STRESS MANAGEMENT AS AN ENABLING TECHNOLOGY FOR HIGH-FIELD SUPERCONDUCTING DIPOLE MAGNETS

A Dissertation

by

EDDIE FRANK HOLIK III

Submitted to the Office of Graduate and Professional Studies of
Texas A&M University
in partial fulfillment of the requirements for the degree of

DOCTOR OF PHILOSOPHY

Chair of Committee,	Peter M. McIntyre
Committee Members,	Alfred D. McInturff
	Che-Ming Ko
	K. Ted Hartwig
	Lin Shao
Head of Department,	George R. Welch

August 2014

Major Subject: Physics

ABSTRACT

This dissertation examines stress management and other construction techniques as means to meet future accelerator requirement demands by planning, fabricating, and analysing a high-field, Nb_3Sn dipole. In order to enable future fundamental research and discovery in high energy accelerator physics, bending magnets must access the highest fields possible. Stress management is a novel, propitious path to attain higher fields and preserve the maximum current capacity of advanced superconductors by managing the Lorentz stress so that strain induced current degradation is mitigated.

Stress management is accomplished through several innovative design features. A block-coil geometry enables an Inconel pier and beam matrix to be incorporated in the windings for Lorentz Stress support and reduced AC loss. A laminar spring between windings and mica paper surrounding each winding inhibit any stress transferral through the support structure and has been simulated with ALGOR®. Wood's metal filled, stainless steel bladders apply isostatic, surface-conforming preload to the pier and beam support structure. Sufficient preload along with mica paper sheer release reduces magnet training by inhibiting stick-slip motion. The effectiveness of stress management is tested with high-precision capacitive stress transducers and strain gauges.

In addition to stress management, there are several technologies developed to assist in the successful construction of a high-field dipole. Quench protection has been designed and simulated along with full 3D magnetic simulation with OPERA®. Rutherford cable was constructed, and cable thermal expansion data was analysed after heat treatment. Pre-impregnation analysis techniques were developed due to elemental tin leakage in varying quantities during heat treatment from each coil. Robust splicing techniques were developed with measured resistivites consistent with nΩ joints.

Stress management has not been incorporated by any other high field dipole research laboratory and has not yet been put to a definitive high-field test. The TAMU Physics Accelerator Research Laboratory has constructed a Nb_3Sn dipole, TAMU3, that is specially designed to provide a test bed for high-field stress management.

DEDICATION

This body of work is dedicated to: my folks, siblings, and kids.

ACKNOWLEDGEMENTS

There is one primary that I would like to acknowledge and give glory to, the Creator and Sustainer of the universe, Jesus Christ. His mercy to me is great and any good within is due Him.

My folks Eddie and Brenda have been a constant support in all ways and means. My sister and brother, Elizabeth and Christopher Odom, were consistent and wise counsellors in addition to being a hostess for the last semesters of my degree. My children, Abigail Rose Holik and Nathan Alen Holik, although separated from me, were always in my thoughts and prayers and provided a chief motivation for each days grind. To each of you this work is dedicated.

From the Mag Lab there is a long list of names that were indispensable in the construction and design of TAMU3. First of course must be Peter McIntyre, my mentor, and the idea man behind stress management. Second must be Alfred McInturff, equally my mentor, who largely enabled the crazy ideas put forth by Peter. Andrew Jaisle was the REAL brains and brawn behind the fantastic transducers (sorry Christopher Benson, Blake Ragland, and JP Ceasar), as well as principally building my magnet; your encouragement kept my head up. Tim Elliott always had a fresh perspective to make any process possible with a little wire and an EDM. Raymond Garrison mastered the impregnation system and was extremely patient with maintaining up to 15 complete revisions to engineering prints. Dior Sattarov is my simulation hero; he always had an answer to my questions that left me feeling stupid. Nick Diaczenko is a fantastic tool and die maker who consistently put the ‘fear of god’ in me about touching tools, and for good measure. I consistently broke them (sorry Drew.) Thank you Saeed Assadi and Tom Mann for your council with managing the difficulties with TAMU3 and help in procuring gainful employment.

To my fellow compodres, Nate Pogue and Kyle Damborsky, I would not have made it through the past 4 years without your friendship. Karie Melconian, Elizabeth Sooby, Josh Kellams, Justin Comeaux, Klaus Smit, Chris Benson, Daniel Krause, and James Gerity, I enjoyed working with each of you. Our conversations consistently challenged my understanding and drove me to be a better scientist.

NOMENCLATURE

A15	Intermetallic superconducting compounds with A_3B chemical formula
AC	Alternating Current
AFRD	Accelerator and Fusion Research Division of LBNL
ARL	Accelerator Research Lab
B_C	Critical Magnetic Field
BIB	Bottom Inner Beam
BICC	Boundary Induced Coupling Currents
BNL	Brookhaven National Lab
BOB	Bottom Outer Beam
BSE	Backscattered Electrons
CDP	Conductor Development Program
CHMFL	Chinese High Magnetic Field Lab
CICC	Cable-In-Conduit Conductor
DC	Direct Current
DMM	Digital Multi-Meter
DOE	Department of Energy
DT	Derivative Time
EDS	Energy Dispersive Spectroscopy
emf	Electromotive Force
FNL	Fermi National Lab
ft-lbs	Foot-Pounds
HD	High field Dipole
HGQ	High Gradient Quadrupole
HQ	High field Quadrupole
HT	Heat Treatment
I_C	Critical Current
IFCC	Inter-Filament Coupling Currents
ITER	International Thermonuclear Experimental Reactor

LARP	LHC Accelerator Research Program
lbf	Pounds of Force
LBNL	Lawrence Berkeley National Lab
LCZ	Inductance Capacitance Impedance
LE	Lead End
LHC	Large Hadron Collider
LN_2	Liquid Nitrogen
MIG	Metal Inert Gas
MJR	Modified Jelly Roll
MOAG	Mother Of All Grounds
NHMFL	National High Magnetic Field Lab
NIH	National Institute of Health
OST	Oxford Superconducting Technologies
PB	Proportional Band
PBD	Pink Book Dipole
PID	Proportional Integrative Derivative
PIT	Powder-In-Tube
QDC	Quench Detection Circuit
RRP	Restacked Rod Process
RRR	Residual-Resistance Ratio
RT	Room Temperature
SE	Secondary Electrons
SEM	Scanning Electron Microscope
SIMS	Secondary Ion Mass Spectroscopy
SS	Stainless Steel
STP	Standard Temperature and Pressure
T_0	Operating Temperature
T_C	Critical Temperature
TC	Thermocouple

TE	Tail End
TIB	Top Inner Beam
TIG	Tungsten Inert Gas
TOB	Top Outer Beam
VPI	Vacuum Pressure Impregnation

TABLE OF CONTENTS

LIST OF FIGURES

Page

LIST OF TABLES

Page

1. INTRODUCTION

The Accelerator Research Laboratory in the Department of Physics at Texas A&M University is developing technology in a series of block dipoles to use advanced superconductors to obtain the highest fields possible by employing stress management in the windings. The first block magnet, TAMU1, tested block winding equipment and procedures as well as a vacuum pressure impregnation (VPI) vessel using NbTi conductor [1, 2]. TAMU2 verified the heat treatment equipment and tested the stress management technology at low field using low J_c Nb_3Sn conductor from the International Thermonuclear Experimental Reactor (ITER) [3-5].

Figure 1: TAMU1, TAMU2, and TAMU3 Superconducting Magnets

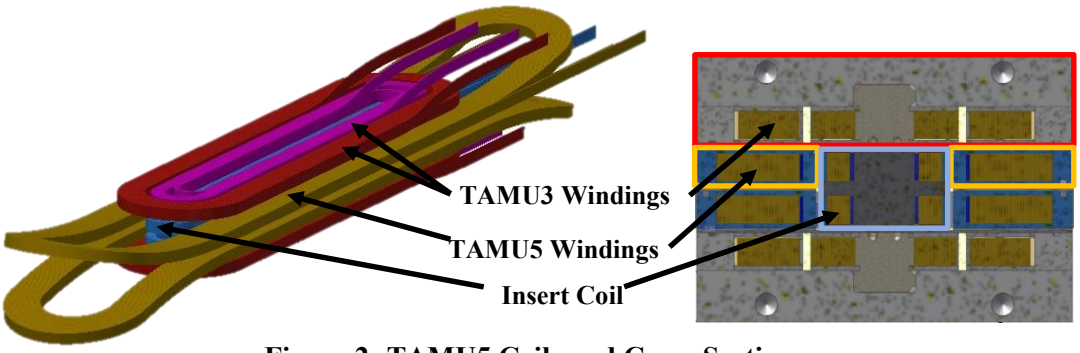

Figure 2: TAMU5 Coils and Cross Section

The completed TAMU magnets are pictured in Figure 1 where TAMU1 is in the top left, TAMU2 at the top right, and TAMU3 is at the bottom. TAMU3 is a high-field (>12 T) test dipole using high J_c Nb_3Sn conductor where irreversible strain-induced current degradation would occur without stress management [6-8]. TAMU5 will feature fully flared ends and a stress managed rectangular bore for testing insert coils and superconducting cable. The TAMU3 windings will supply the top and bottom windings of TAMU5 and are indicated in Figure 2.

1.1 Motivation

The advent of the Large Hadron Collider (LHC) opens a new era for continuing to explore predictions of the Higgs sector of the Standard Model and the prospect for discovery of the particle spectrum of Supersymmetry. At the same time we must continue developing the accelerator physics and technology necessary to extend the reach in energy and mass beyond the window that is opened by LHC.

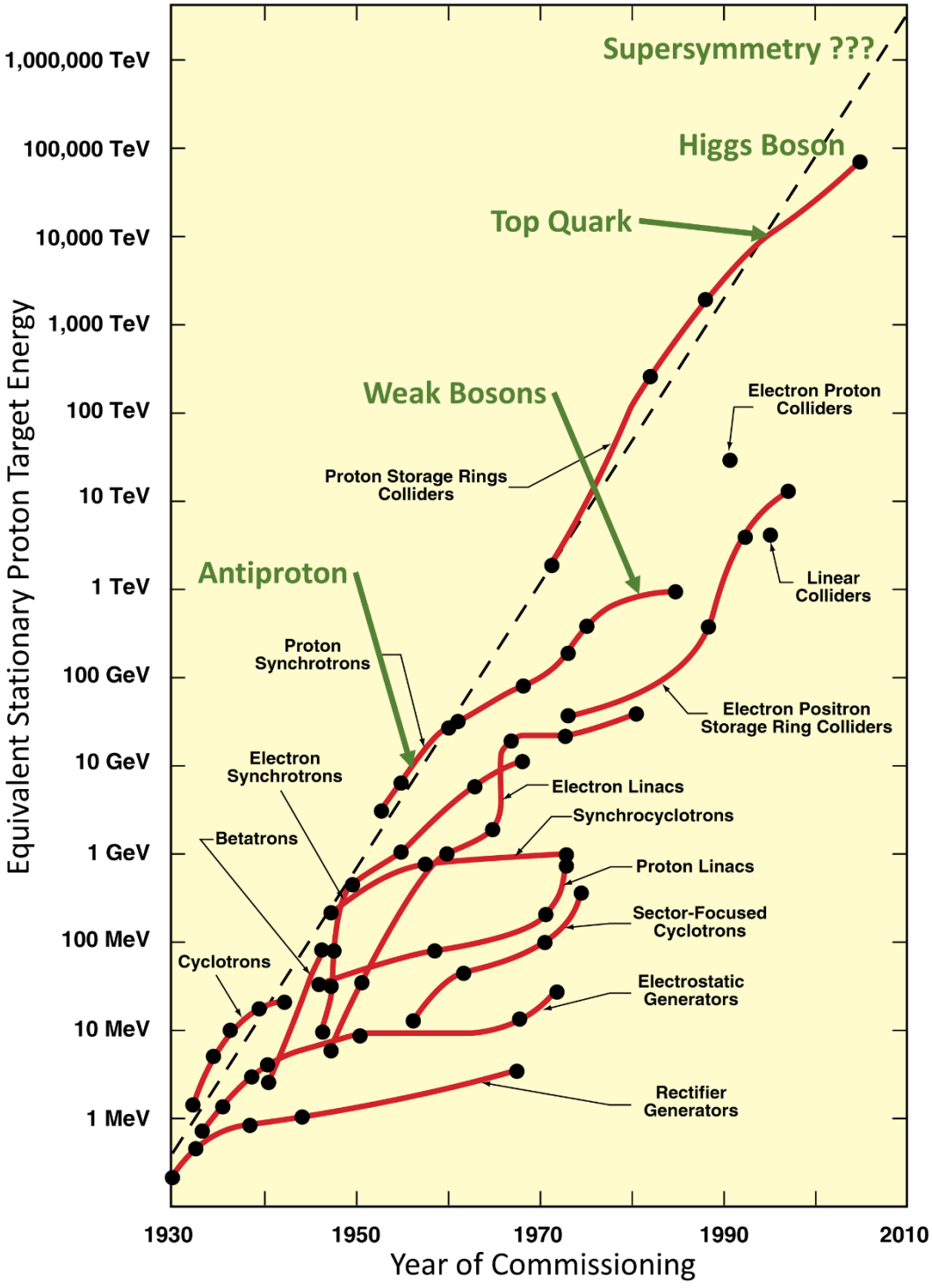

Figure 3 : Livingston Plot [15]

1.1.1 Discovery Accompanies Higher Energy

Since the first high voltage accelerators of the early 1930's, the particle physics community has been ablaze with discovery. Accelerators have enabled the discovery of rare elements and fundamental particles and have pushed technology in medical imaging and proton therapy [9-13]. Discovery quickly follows collision energy increases. Therefore it is essential to the future of particle physics to invest in new technology for future colliders to increase the energy.

A similar plot to the one first generated by Stanley Livingston in 1954 shown in

Figure 3 demonstrates how various types of accelerators have obtained higher and higher energies in an exponential fashion as time has progressed [14-16]. The equivalent stationary proton target energy is determined by requiring the Lorentz 4-momentum product to remain invariant in both the center of mass and lab frames.

Concepts have been presented for an LHC energy tripler [17], a 100 TeV $p\bar{p}$ collider [18], and a muon collider [19-21]. Within the U.S. LHC Accelerator Research Program or LARP there are also pressing projects including 11 meter long, 11 tesla dipoles to enable the high luminosity LHC or HL-LHC [22].

1.1.2 Higher Energy by Higher Magnetic Field

For hadron synchrotrons the energy of the particles varies according to the following hard-relativistic ($E \cong pc$) relation:

$$E[TeV] = 0.3\, R[km]\, B[T] \tag{1}$$

where *E*, *R* and *B* are the energy, radius and magnetic field respectively of a synchrotron accelerator. To increase the energy either the radius of the ring or the dipole magnetic field strength must increase. Increasing the magnetic field strength is the current focus of the accelerator community [22, 23].

1.2 Challenges

Every high field synchrotron built to date has primarily used NbTi alloy as the superconducting material. NbTi has a critical temperature of 9 kelvin, a critical field of 15 tesla and is extremely tough with a 700 GPa tensile strength compared to 200 GPa for common high strength steel [24, 25]. These properties make NbTi a robust conductor for practical magnets up to roughly 9 tesla. The Large Hadron Collider uses NbTi magnets that are designed at 8.4 tesla at superfluid temperatures. For attaining higher field strengths a new conductor must be chosen.

Advanced superconductors carry more current at higher field but often require intricate formation heat treatments and are strain intolerant. They are also much more expensive and have transport current anisotropies. These challenges make constructing a successful high-field dipole difficult.

1.2.1 Intrinsic: Supercurrent Transport

The most important parameter for efficiently obtaining high field strengths is current density. Currently there are two conductors that have transport current properties that are conducive for accelerator dipoles, Nb_3Sn and Bi-2212. Figure 4 from Peter Lee at the Applied Superconductivity Center in Tallahassee shows the engineering current density of pertinent magnet conductors as a function of the applied perpendicular magnetic field. To design an efficient, cost-effective accelerator dipole the engineering current density needs to be above 800 amps / mm^2 (4.2K, 12T) as indicated in Figure 4 [26, 27]. The current density of the low temperature A15 superconductor Nb_3Sn at field strengths below 16 tesla fits this criterion.

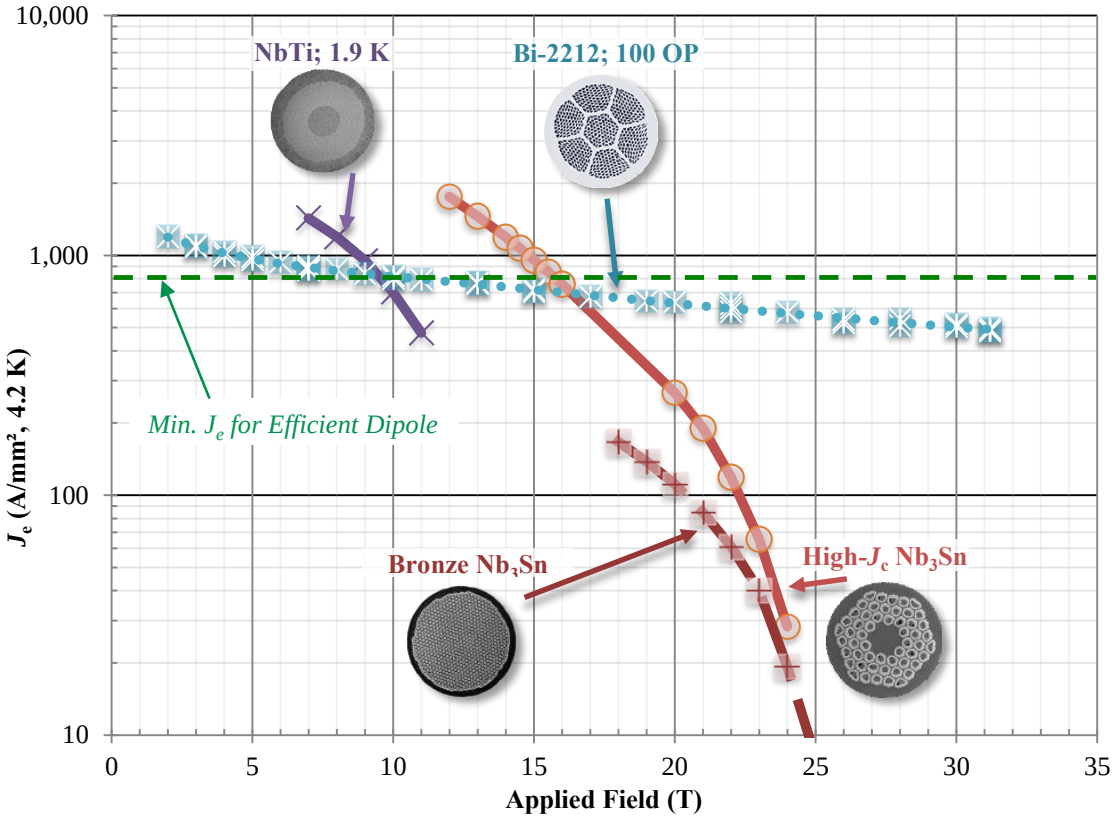

Figure 4 : Engineering Current Density as a Function of Applied Field

Despite extremely high critical field values the cuprates and other high temperature superconductors with correct conductor geometry must improve their current density, techniques, methodology, execution, and technology at field strengths greater than 12 tesla by a factor of three to five [26] before they become advantageous in accelerator magnets. Higher packing density and 100 bar over pressure heat treatments have the potential to double the current density of Bi-2212 to 725 amps / mm^2 at 20 tesla and 4.2 kelvin [28]. Over pressure heat treatments on large magnets in an oxygen atmosphere for Bi-2212 are currently impractical unless a structured cable is involved [28-30].

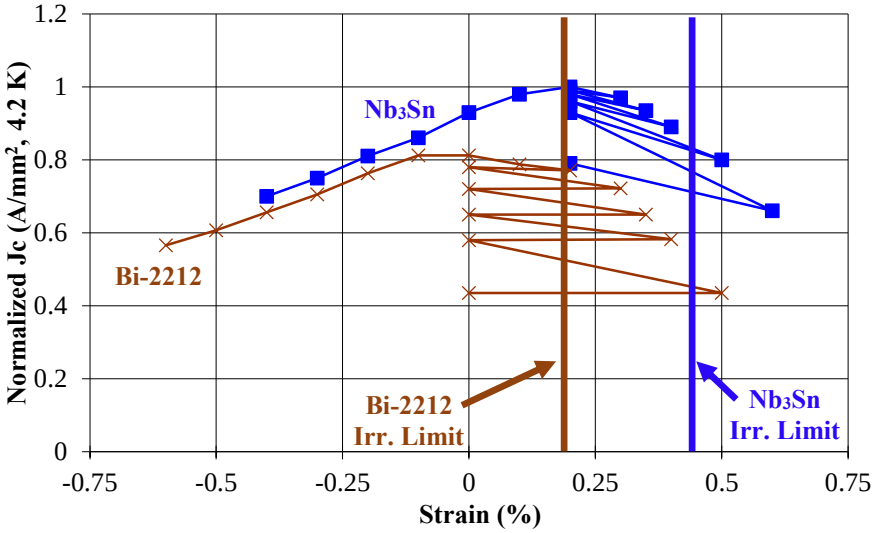

Figure 5: Normalized Current Density as a Function of Strand Stain

1.2.2 Extrinsic: Strain Degradation

The current density of Nb_3Sn is dependent on the amount of strain on the conductor. Differential expansion of the stabilizing copper and the A15 Nb_3Sn gives about 0.2% intrinsic compressional strain [31-33]. Strains of 0.3% degrade the current carrying capacity and strains above 0.4% irreversibly degrade the conductor. The strain sensitivity in Bi-2212 is worse with a 0.2% irreversible degradation level as shown in Figure 5 [34-36]. This leads to a typical winding package having a reversible degradation limit of 150 MPa and an irreversible degradation limit of 200 MPa [37]. The force on the conductor is quadratically dependent on the magnetic field strength; doubling the magnetic field strength will quadruple the conductor forces.

1.2.3 Conductor Heat Treatment

The brittle nature of the A15 compounds require that stoichiometric Nb_3Sn form after the winding is in its final geometry. This requires that an intricate heat treatment schedule be employed. The heat treatment includes a 210°C / 48 hours Sn stabilization and copper

anneal soak, a 340°C / 48 hours solid diffusion soak, and a 670°C / 70 hours formation soak. The formation temperature and duration can range from 650°C - 700°C for 50 – 100 hours depending on the chosen balance between current density and stabilizing copper purity. Long, high temperature heat treatments maximize the current density and short low temperature heat treatments keep the stabilizing copper pure for increasing the dynamic time constant or the rate at which flux moves. The copper purity is measured as the ratio of the room temperature coil resistance to the resistance at 20 kelvin or tactfully above the cable critical temperature. This is known as the Residual Resistance Ratio (RRR.)

The same winding must then cool from 670°C to room temperature, be vacuum pressure impregnated and cured at 125°C, then installed into a flux return at 75°C, and finally cooled to 4.2 kelvin for testing. Stringent demands on material strength and thermal expansion limit the number of materials that can be used in both the magnet and the conductor itself.

1.3 Strategy

There is a five-fold strategy to obtain the highest fields possible in accelerator dipoles. This approach maximizes the transport current potential of the conductor by minimizing strain induced current degradation.

1.3.1 Adopt a Block Coil Geometry

Every superconducting ring magnet constructed so far has used a cosine theta geometry that efficiently uses conductor and produces a nearly perfect dipole field in the bore. In a cosine theta magnet the high stress zone and high field region coincide, both of which decrease the current density. The Lorentz force in a cosine theta coil is supported by the cable edge and requires that the cable have a keystone angle to maximize the number of turns. In a block dipole the force is supported over the cable face and doesn't require keystoning the cable.

The block coil geometry does not use the conductor as efficiently as an ideal cosine theta coil. However, with current densities greater than 3000 A/mm^2 and peak fields

greater than 16 tesla the attainable field with a cosine theta magnet will most likely be strain limited.

1.3.2 Select Nb_3Sn as Conductor

Nb_3Sn essentially doubles the attainable magnetic field in an accelerator dipole that NbTi is capable of producing (from 8 T to 16 T.) Nb_3Sn has now been developed to maturity as a high-field superconductor with good stability and ~km piece length of fine-filament wire and is the only superconducting alternative to NbTi considered sufficiently developed for large scale use [38].

We are using a Restacked Rod Processed (RRP®) internal-tin conductor made by Oxford Superconducting Technologies. The strand is capable of 2800 amps / mm^2 at 4.2 kelvin and 12 tesla.

1.3.3 Wind & React

The strain sensitivity of Nb_3Sn requires that the precursor Rutherford cable be tightly packaged to inhibit cable movement during and after reaction bake. Immediately following reaction bake robust NbTi leaders are soldered to the brittle Nb_3Sn leads.

1.3.4 Vacuum Pressure Impregnation

In Rutherford type cable the crossover points create point like contacts that can overly strain the conductor. Packing all the voids with a high tensile strength fabric and filling epoxy spreads the force uniformly as shown in Figure 6. VPI increases the stress tolerance of the winding package by minimizing the inter-wire point contact force and filling voids to reduce conductor movement from Lorentz force.

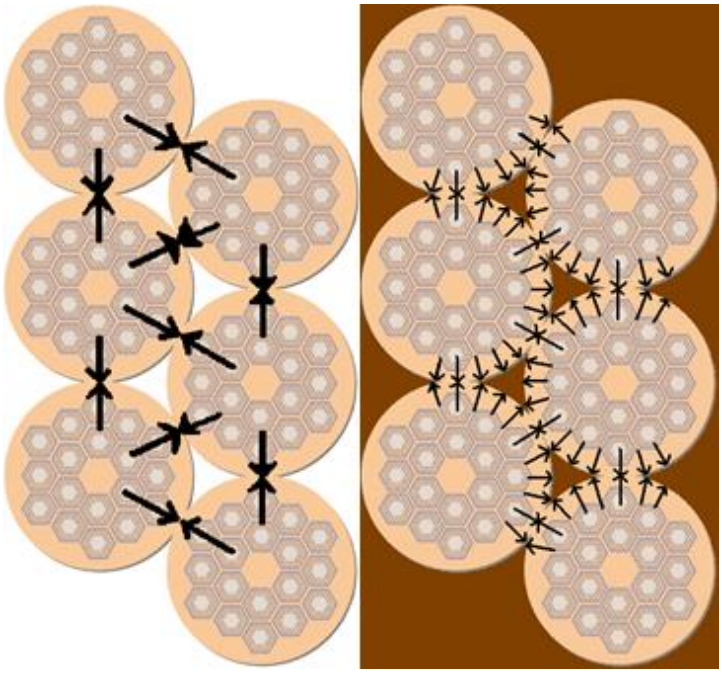

Figure 6: Stress Distribution with Bare Cable and an Impregnated Coil

1.3.5 Stress Management

The final component to protecting Nb_3Sn conductor from strain degradation is stress management. Stress management is a scheme to introduce a high-strength structure directly into the windings to intercept Lorentz stress before it accumulates to levels that would degrade the current carrying capacity of the conductor.

2. STRESS MANAGEMENT

There are 6 features that must work in tandem to enable and verify the success of stress management. Each component will be explained at depth below.

2.1 Coil Configuration

In a block coil geometry the high stress zone is in the low field region (at the last turns of the inner coil for TAMU3.) Block coil dipoles allow support structures to be incorporated in the windings that are perpendicular to the cable face. Stress management requires that a block dipole configuration be employed.

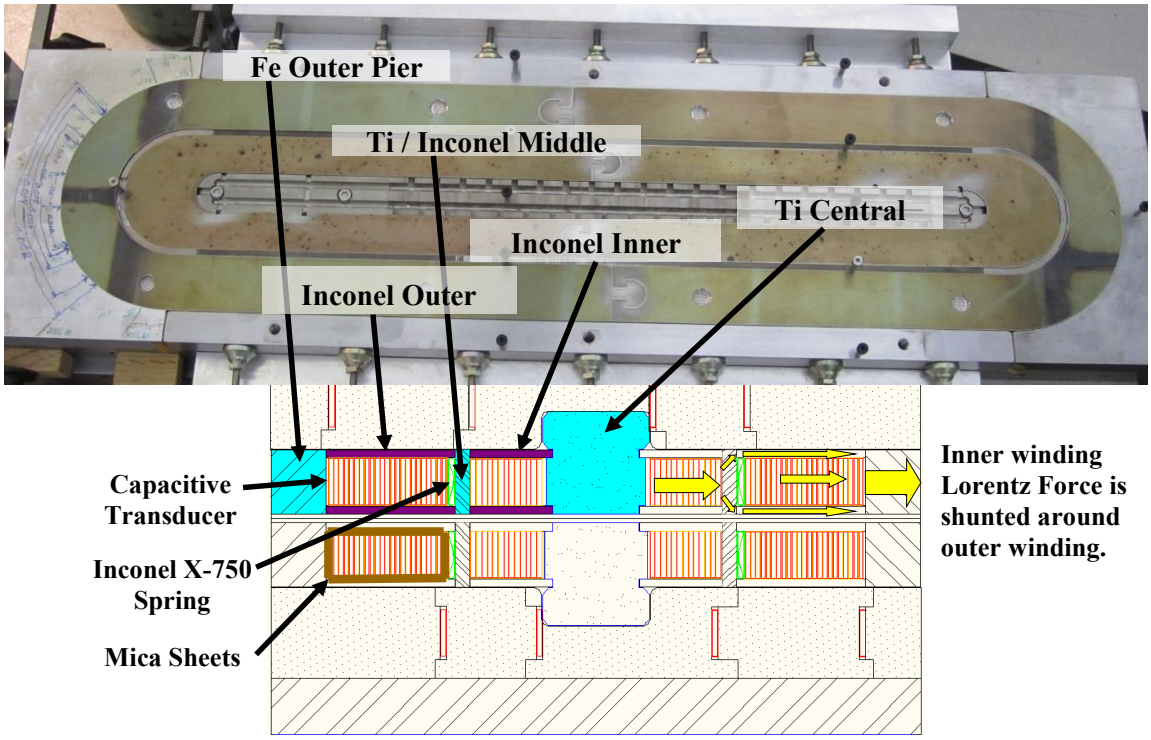

Figure 7: Key Stress Management Components

2.2 Support Matrix

A pier-and-beam support matrix is integrated into the windings so that outward-directed Lorentz stress developed in the inner winding is intercepted on a beam and bypassed around the outer winding as shown in Figure 7. The arrows on the right hand side of Figure 7 demonstrate how the Lorentz force from the inner windings is intercepted by an Inconel middle pier and bypassed around the outer windings through the outer beams. The yoke in turn is supported rigidly by compression within a stress tube, and so both windings are supported within a high-modulus structure and the stress within each winding is limited to a value that prevents strain degradation of the superconductor.

2.2.1 Expansion Coefficients

The central pier is made out of titanium with an integrated expansion coefficient to 4.2 kelvin that is less than the cable and the surrounding support structure. The differential contraction removes unnecessary strain on the inner winding during the 670°C formation heat treatment and maintains preload at cryogenic temperatures. The middle and outer pier end hoops are also made out titanium so that the vertical preload will friction-lock the end hoops in place at cryogenic temperatures to support axial Lorentz stress. The beams are made out high strength Inconel 718 to handle the large Lorentz stress. Expansion slots are machined into the Inconel support structure so that the outer coil is not stretched during heat treatment.

2.2.2 Force Interception and Beam Bending

The success or failure of stress management will be determined by how well the inner winding Lorentz stress is bypassed around the outer winding. The inner winding Lorentz forces at peak field are large enough to deflect or bend the middle pier and compress the outer beams. Using Euler-Bernoulli beam theory for Inconel 718 at cryogenic temperatures we may calculate the deflection of the middle pier at 0.003 inches and the associated compression of the outer beams as another 0.003 inches. This also can be simulated in ALGOR® and the results are shown in Figure 8.

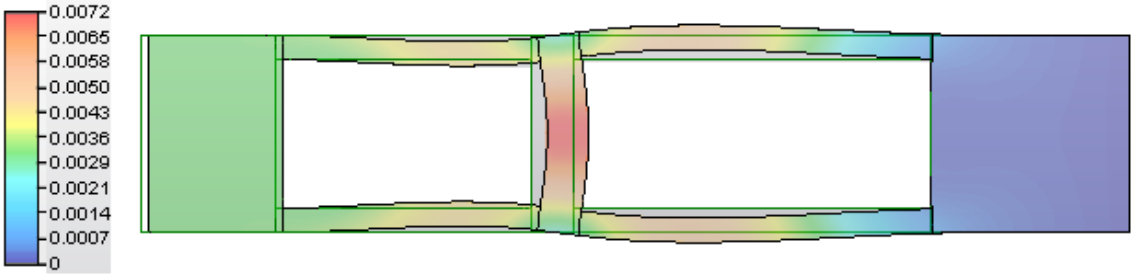

Figure 8: Pier and Beam Deflection in Inches

Figure 8 shows that the middle of the middle pier deflects roughly 0.007 inches. This result requires that a soft modulus element be placed between the middle pier and the outer windings to absorb the deflection and inhibit the outer winding from strain degradation.

2.3 Soft Modulus Element

The Accelerator Research Laboratory has developed a laminar spring that will absorb middle pier deflection, preload the outer winding, and take up minimal space. Figure 9 shows a cross section of the laminar springs developed for the TAMU series magnet development. Incorporating the laminar spring into the winding package protects the entire outer winding from load transfer from pier and beam deflection. Although the spring takes up valuable engineering real estate, it is necessary to ensure full mechanical separation between windings.

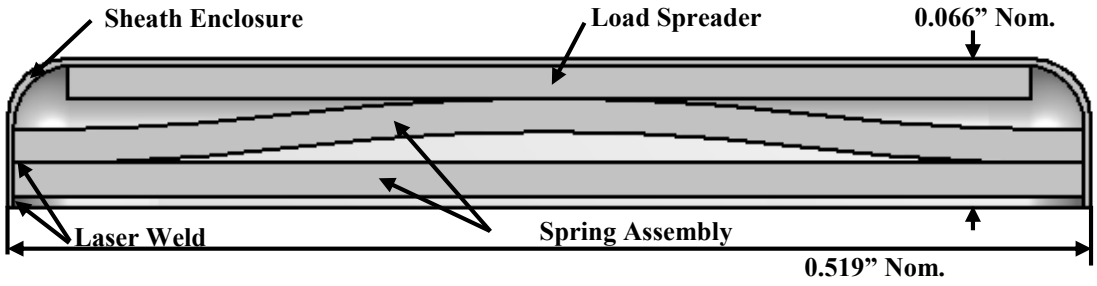

Figure 9: Cross Section of Laminar Spring

2.3.1 Absorbs Middle Pier Deflection

The laminar spring is designed to absorb a maximum 0.010” at 500 psi before yielding or taking a set. The outer winding shim package is designed to compress the springs by 0.003” to 0.005” at 200 psi to 300 psi which leaves 0.005” to 0.007” to absorb the middle pier deflection. These design specifications were verified experimentally and through simulation with ALGOR®.

2.3.2 Preloads Outer Winding

The laminar spring serves the additional purpose of lightly loading the outer winding package from assembly to reaction bake to cool-down. This ensures that the outer winding has minimal void space and is in intimate contact with the rigid outer pier support structure while Vacuum Pressure Impregnation and ultimately while testing the magnet.

2.4 Shear Release

Mica is a sheet silicate mineral with very thin cleavage planes that have a low coefficient of friction. Mica paper is placed on all four sides of each winding as indicated in Figure 7 on page 11. The mica paper creates a shear plane that allows the cable to gradually and uniformly shift relative to the support structure as the Lorentz force increases. The mica also electrically insulates the conductor from the support structure.

2.4.1 Low Friction Motion

The mica prevents sudden movement called stick-slip motion that creates enough heat to raise the temperature of the conductor to a point above T_C where it can no longer carry sufficient transport current. When a section of cable become resistive and loose superconductivity it is said that the coil undergoes quench. Therefore mica paper reduces the chance of quench and training caused by stick-slip motion [39-43].

2.4.2 Minimizes Magnet Training

In a typical high field magnet, each successive quench occurs at higher and higher currents and different locations. This is possibly caused by structure / epoxy / conductor separation. Each quench locally minimizes stick-slip motion and stabilizes the matrix [43]. This plausible process can lead to training of the magnet. With most magnets, the maximum current steadily increases toward a plateau with each additional quench [44-46]. Stress Management aids in minimizing the magnet training phenomenon by properly supporting the coil with piers and beams, preloading with laminar springs, and minimizing stick-slip motion with mica shear planes. No training was observed in TAMU2 because of low peak field and stress management [3].

2.5 Hydraulic Preload

After impregnation the magnet modules are installed in the iron flux return contained within the centripetally forged 2219 aluminum alloy stress cylinder. Wood's metal filled stainless steel bladders act as a smart shim for ideal Lorentz stress support between the magnet module, the flux return, and the stress cylinder. Figure 10 shows the location of the stainless bladders in blue. The red arrows indicate the coil preload from the bladders. Other magnet groups at Fermilab or LBNL use a bladder-and-key approach to preload. The bladder is only used to overly compress the coil for clearance so that a key can lock the support structure into place [47, 48].

2.5.1 Metal Filled Bladder

Wood's metal is the generic name for the eutectic compounds of bismuth, lead, tin, and cadmium with a 70°C melting point. Cerrolow alloy 147 has a small addition of Indium to decrease the melting point further to 64°C. Cerrolow alloy 147 was chosen and procured for TAMU3 for its low melting point and supposed small integrated thermal expansion coefficient to cryogenic temperatures. There is a 1.7% volumetric contraction when solidified [49] but should not affect the ultimate bladder preload because of a controlled solidification process in which Wood's metal continually will flow into the

bladder as each zone sequentially solidifies and contracts. The entire coil and flux return assembly is heated above the melting point to roughly 80°C so that bladders can be filled.

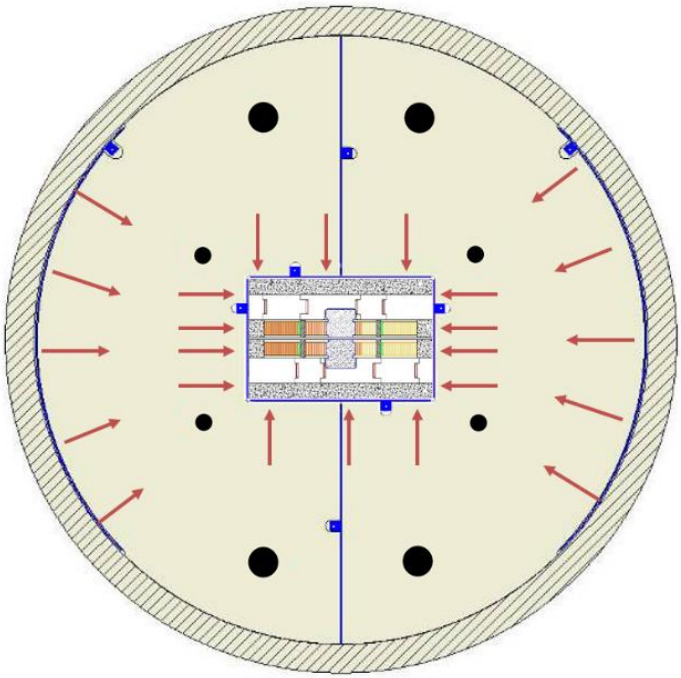

Figure 10: Stainless Bladders and Pre-Load

2.5.2 Surface Conformity

The outer arched bladders are filled to 13.6 MPa to give essentially an infinitely rigid support for the rectangular aperture inside the iron yoke. The top, bottom, left, and right magnet bladders are filled from 3.8 to 4.1 MPa. This pressure range enables the bladders to adequately conform to surfaces without overly pressing the magnet modules. The bladders have been tested up to 70 MPa without leaks [50].

2.5.3 Isostatic Preload

The metal is cooled and the bladders supply a conforming and isostatic pressure to each magnet module and assure rigid support. Uniform preload to all surfaces is crucial to ensure that no region or stress management structure can flex when Lorentz forces develop during magnet testing.

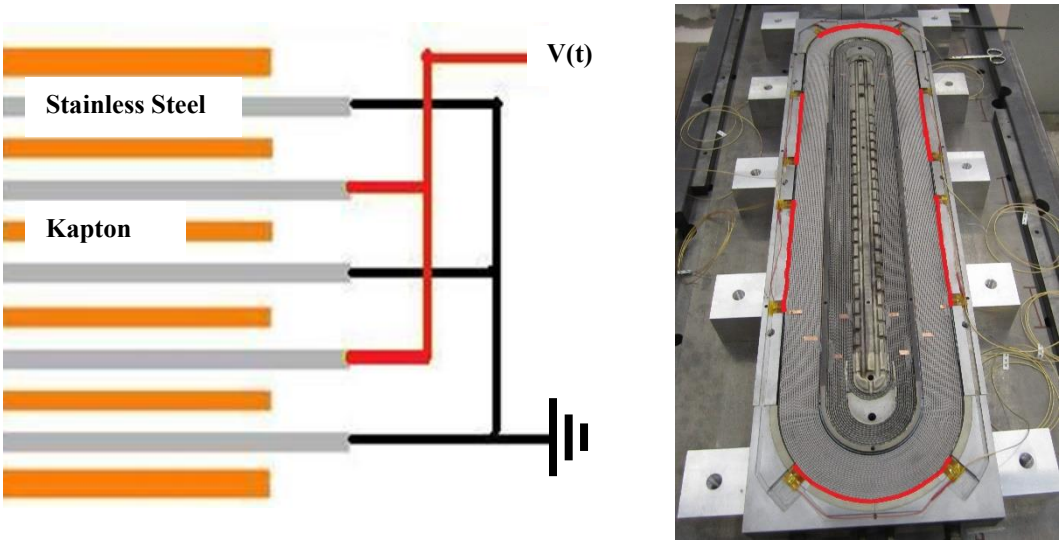

Figure 11: Capacitive Transducer Schematic and Locations

2.6 Stress Transducers

Laminar capacitive stress transducers are evenly distributed between the outer winding and the outer pier. They are simply a multi-laminate of alternating Kapton and stainless steel foils with a thin layer of epoxy for glue as shown in Figure 11. The laminate's capacitance varies as a function of the integrated Lorentz stress to the surface and will provide a measurement of stress.

2.6.1 Challenges and Solutions

Previous transducers constructed for TAMU2 required extensive calibration and experienced internal creep and zero-shifts after thermal cycling so that it was difficult to accurately interpret the results. Transducers developed in Russia, CERN, FNAL, BNL and LBNL also had the same problems [51-56]. Much effort was devoted to curing these problems with new construction procedures and tooling [57].

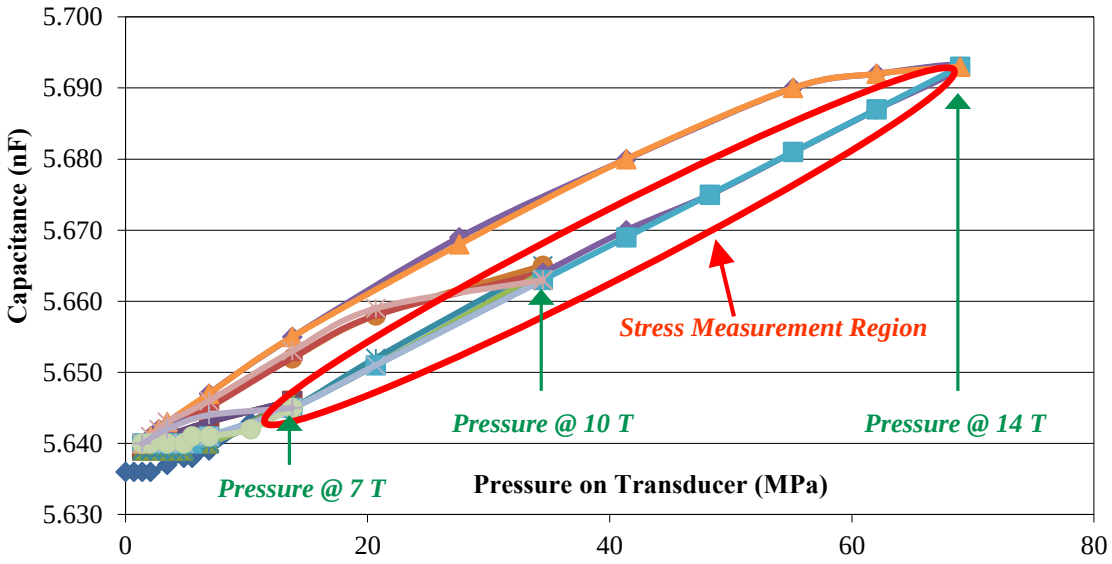

Figure 12: Capacitance as a Function of Pressure

New tooling and construction techniques enabled new transducers to be very reproducible in dimensionality and quality control. The retooling results are promising with a ±2% cycle to cycle reproducibility as shown in Figure 12 [57-59]. The cyclic off-set is minimal compared to previous transducers with practically no creep. The new transducers are an exciting advancement in magnet technology and should enable a precise test of stress management. Each capacitive stress transducer is individually calibrated so that the average expected uncertainty at 70 MPa (full field) will be 3.5 MPa.

2.6.2 TAMU3 Stress Management Test

Stress management in TAMU3 will be quantified using capacitive stress transducers. The transducers are located between the outer winding and the outer pier as shown on Figure 11 on page 17 and should only measure force from the outer winding. If the transducers measure a force that is larger than the integrated force of the outer winding then there was force transfer through the middle pier and spring and the stress management scheme needs modification. If the transducers measure a force that is equal to or below the integrated force generated from the outer windings then the stress management scheme was successful. The transducers are the primary stress management measurement devices.

2.7 Strain Gauges

In TAMU3 axial Lorentz force is contained and transferred to the flux return through friction lock. Friction lock is a method of taking advantage of integrated differential expansions of materials to lock load bearing components in place. Friction lock is a crucial component to stress management.

The middle pier and outer pier end shoes are made out of Grade 5 titanium with an integrated thermal expansion coefficient to 4 kelvin that is significantly less than the surrounding steel (1.5 mm / m and 2.1 mm / m respectively.) Upon cool down to 4 K the surrounding iron will rigidly compress the titanium and friction lock the end shoes. This will directly transfer the axial Lorentz force to the thick magnet base and thin skin without the need for bulky external bracing. Friction lock will be verified for the first time at high magnetic field strength in TAMU3.

Strain gauges will be used to measure the effectiveness of friction lock in stress management. Ideally all of the axial force will be absorbed by friction lock. If there is any slippage or load transfer then the strain gauges will give valuable quantitative information. This is accomplished by placing the gauge between the thrust bolts and the winding package.

3. TAMU3 DESIGN

TAMU3 is a Nb_3Sn bi-modular single-pancake dipole that is the first test of stress management at high field strength. The two modules of TAMU3 are optimized to become the background field for subsequent magnet assemblies. Stress management in TAMU3 is designed to protect the conductor from strain degradation. The high-field strengths and associated Lorentz forces in TAMU3 will vet stress management as a potential means to enable conductor to obtain the highest fields possible by inhibiting strain degradation.

3.1 Magnetics

The TAMU3 modules were originally designed and optimized to supply the background field for TAMU4 and TAMU5. The TAMU3 configuration makes the field strength in the lead and tail ends 1.4 tesla larger than the peak field in the straight section where the stress management structure is to be tested. Modifications to the iron were necessary to make the body field as large as possible and move the peak into the body.

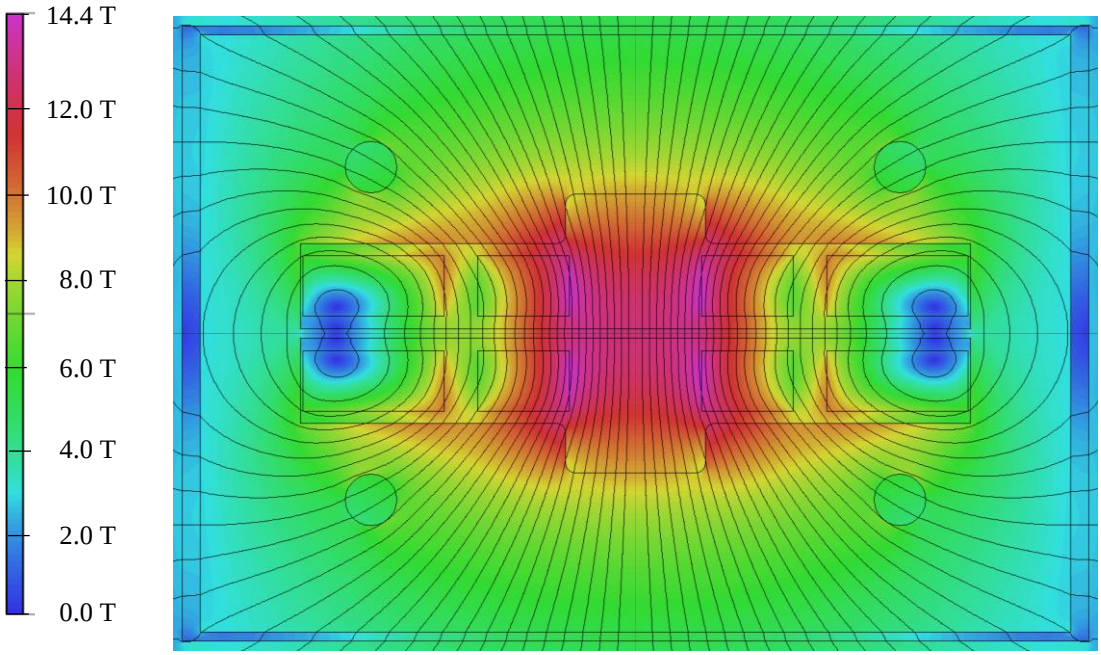

Figure 13: Magnetic Field and Field Lines in 2-D Cross Sectional View

3.1.1 2-D Magnetic Field Simulation

Vector Fields OPERA® produced the 2-D simulation shown in Figure 13. The magnetization curve for standard iron used. From the 2-D simulation and critical current properties of the Rutherford conductor we set the current for all 3-D simulation to 13.9 kA. When the first full 3-D simulation converged it was found that there was roughly a 1.4 tesla difference between the 2-D peak field (14.4 tesla) and the 3-D peak field (15.8 tesla.) To correct this oversight the only realistic option was to replace iron components with non-magnetic materials.

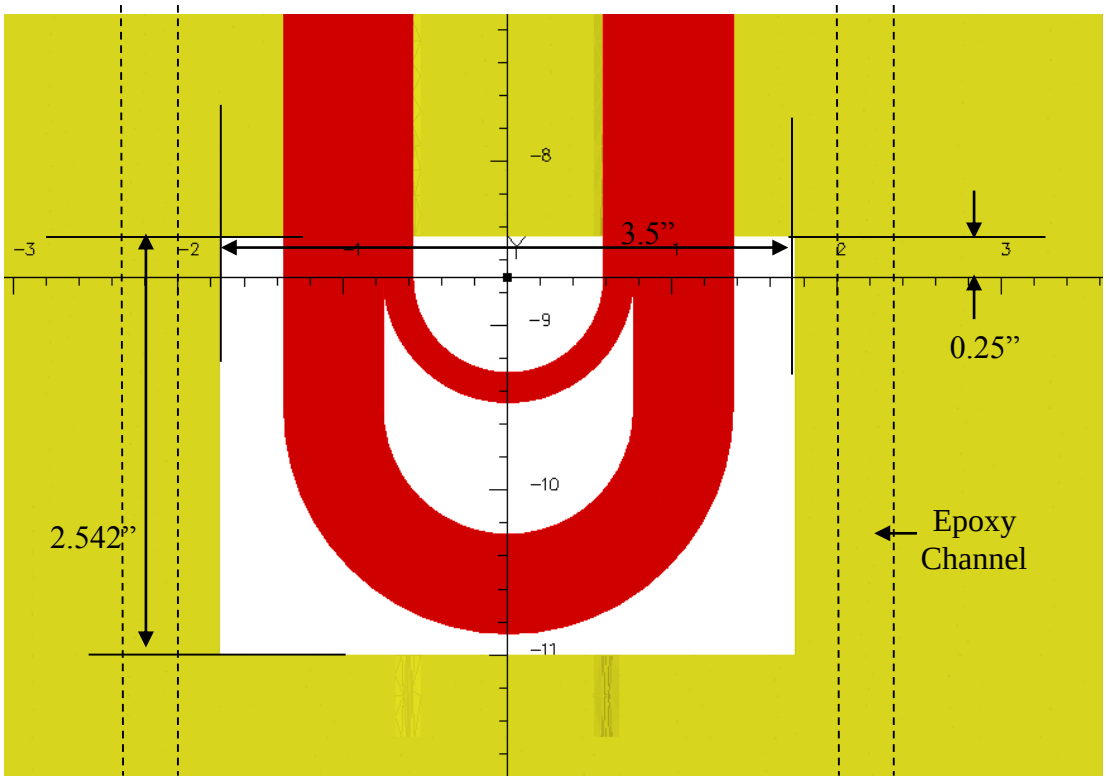

Figure 14: TAMU3 Inner Winding and Removed Iron

3.1.2 Iron Modification

Select tooling, the iron magnet base or thick skin, along with end filler iron was modified to reduce the peak field difference between the ends and the straight section to 0.2 T. The amount of removed iron above and below the red inner winding of TAMU3 is shown in Figure 14. Figure 15 shows a picture of the modified thick skin with a stainless steel insert along with the new stainless steel end tuner.

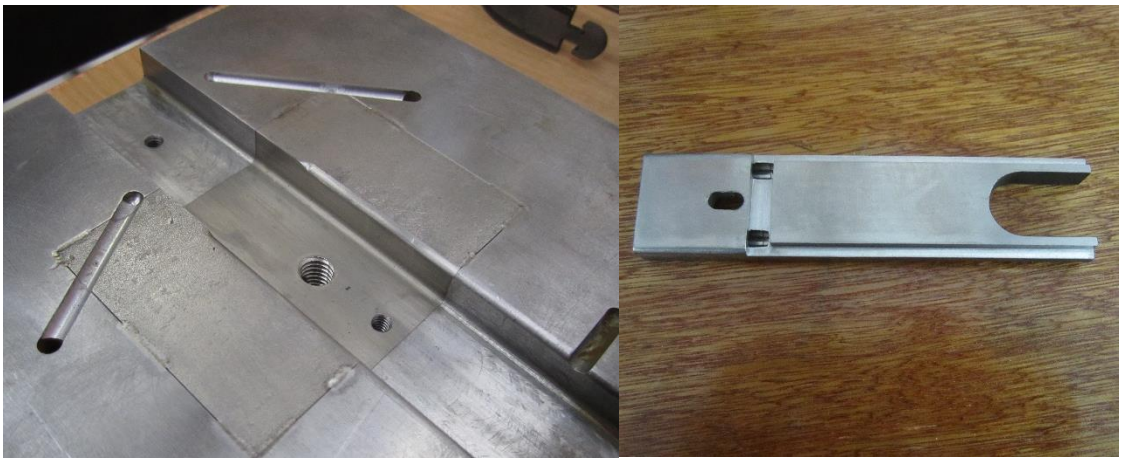

Figure 15: Picture of Modified Thick Skin and End Tuner

Figure 16 shows the filler iron with inserts of titanium along the two ends. The picture on the left shows the titanium insert with four epoxied 'dog bone' joints that hold the metals in place. The epoxy chosen was a two part 'toughened' epoxy (DP-460NS) from 3M®. This advanced epoxy is commonly used to attach golf club heads with shafts. The filler iron pieces are comprised of titanium and A36 mild steel and were co-ground together to dimension by Brent Grinding and Machining in Houston, Texas. The right picture in Figure 16 shows both filler irons with one additional filler piece attached.

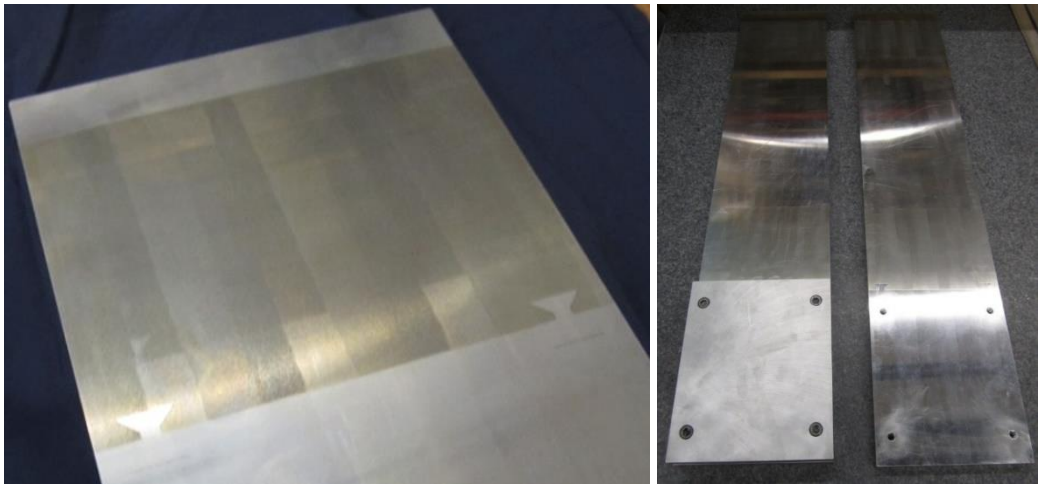

Figure 16: Filler Iron Modified with Titanium Inserts

The filler bar has titanium over the end shoes because of its small integrated expansion coefficient from room temperature to cryogenic temperature. This will maintain friction lock over the lead and tail ends while reducing the peak field in the region. The middle section of Figure 16 remained iron to maximize the magnetic field in the body of the coil.

3.1.3 3-D Magnetic Field Simulation

The modification discussed in the previous section were driven by an iterative process of iron cuts and associated field variations in the magnet. Only the iron distribution of the final version of TAMU3 is presented below.

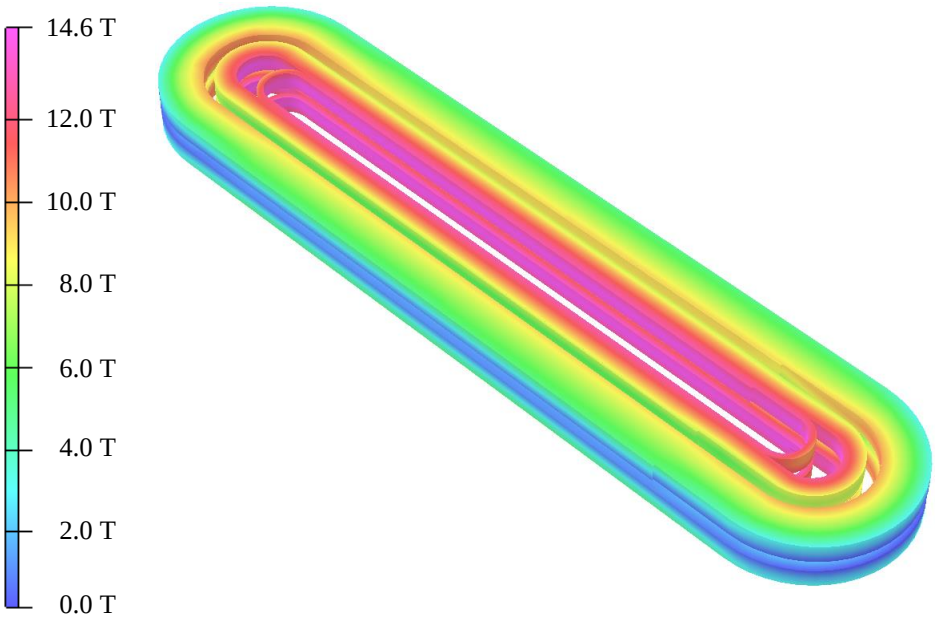

Figure 17: Magnetic Field on the Conductor

All magnetic simulation was performed with OPERA® Vector Fields assuming a standard magnetization curve for iron. In Figure 17, the peak field on the conductor is reduced to 14.6 tesla from 15.8 tesla at 13.9 kA. The peak field is located in the lead end and is 0.2 tesla larger than the body peak field.

Figure 18 shows the longitudinal magnetic field along the length of the magnet. The small black boxes at the ends are the cross sections of the superconducting coils. The left hand side of the figure is the lead end of the magnet. This image nicely displays how the iron modifications reduce the peak field in the ends and maintain high field strength in the body. The primary modification effects are circled in Figure 18.

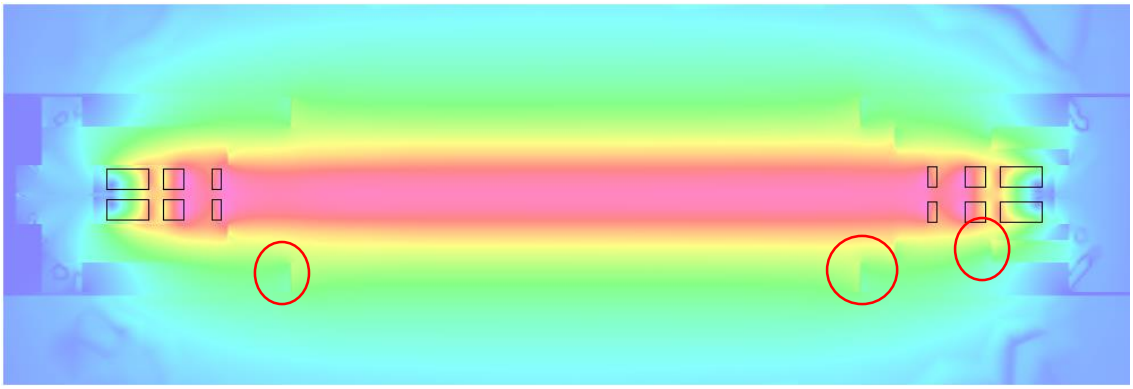

Figure 18: Longitudinal Magnetic Field Along the Length of the Magnet

3.1.4 Load Line and Magnet Parameters

The peak magnetic field is on the pole turn at the lead end of the magnet on the opposite side of the lead. TAMU3 has a peak field of 14.36 T at 13.72 kA. The geometric centerline field strength is 12.78 T. Table 1 gives all of the important parameters for simulating quench and collected parameters from the 3-D load line plot in Figure 19. The load line plot gives the critical current of the inner and outer Rutherford cable as a function of the background magnetic field as well as the transfer function of the magnet. The transfer function is simply what the peak magnetic field is for a given coil current. The intersection of these two functions are where the magnet will operate and is circled in Figure 19.

Table 1: Important Load Line Parameters

Property	Value
Inner Turns	13 Turns
Outer Turns	23 Turns
Magnet Inductance	2.5 mH
I_c (Inner Conductor limited)	13.72 kA
B_c (Inner Conductor)	14.36 T
B (Outer @ Ic)	11.24 T
B_c (Outer @ Ic)	13.22 T
B in probe bore at Ic	9.95 T

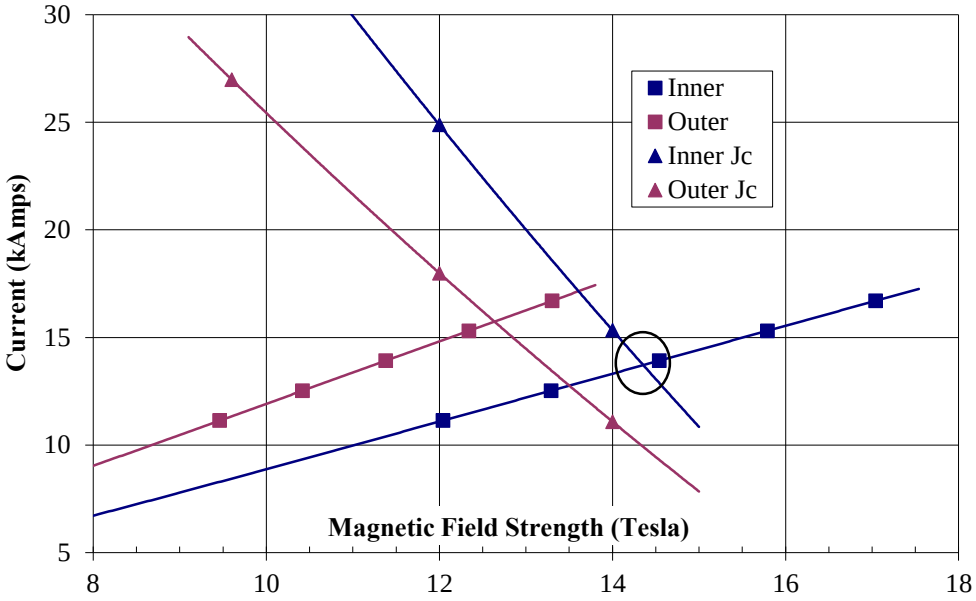

Figure 19: Load Line Plot for TAMU3

3.2 Structure Measurements

Winding in block geometry, applying mica shear planes, and installing laminar spring relax cable tolerances and ease the winding procedure. However, the stress management structure must have tight tolerances to minimize gaps and void space that often causes magnet training. Gaps between piers, beams, and conductor might allow excessive structure movement and ultimately stress transfer between windings and strain degradation. To properly apply the stress management scheme several tooling and conductor measurement procedures were developed.

3.2.1 TAMU2 Difficulties

TAMU2 was a single pancake, mirror configured Nb_3Sn magnet that obtained 98% of short sample at 6.8 T with no measureable training [3]. Magnet autopsy revealed that there were gaps between stress management structures, over and under compressed springs, and tilted Rutherford type cable. The attained magnetic field did not generate

sufficient Lorentz force to irreversibly degrade the conductor and thus any shortcomings in the stress management scheme was benign. These problems are addressed in TAMU3.

3.2.2 TAMU3 Solutions

In TAMU3 the forces are expected to be large enough to irreversibly degrade the conductor. Cable location, spring compression, and support structure must be accurately located within tolerance for the stress management scheme to successfully protect the brittle Nb_3Sn conductor.

3.2.2.1 10-Stack Measurements

The geometric and mechanical properties of the conductor in bare and impregnated form must be determined to accurately locate the cable, determine shim size, and close the stress management structure. This is accomplished by making a mock-up of a 10-stack winding package. The cable properties as determined from 10-stack measurements are summarized in Table 2. The fine filament S-2 glass from AGY and sock insulation braided by A&P Technologies was tested by 10-stack. The new insulation has a 20% increase in shear strength with no loss in electrical integrity. The new fine filament insulation is also 50% thinner which increased the engineering current density by 10% [60].

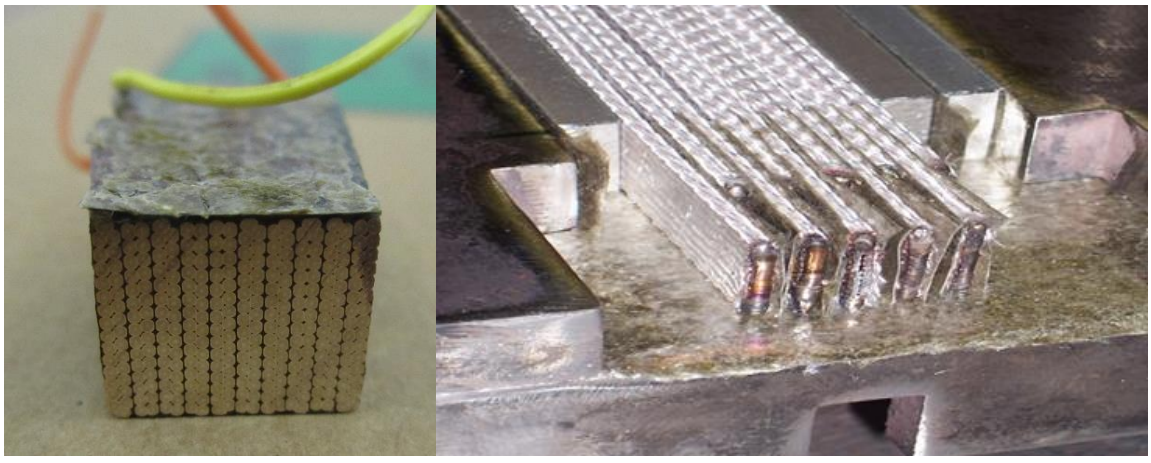

Figure 20: Ten-Stack Cross Section and Assembly

Table 2: Data from 10-Stack Analysis

Type	Description				Units
Dimensional	Bare Cable Dimensions	Inner	1.4155	13.031	mm
		Outer	1.2079	13.022	mm
	Insulated Cable Dimensions	Inner	1.5255	13.141	mm
	Under ~2MPa	Outer	1.3179	13.132	mm
	10-Stack Fabrication Pressure			2 – 3	MPa
Mechanical	10-Stack Shear Strength		Palmitic Acid	47	MPa
	Turn / Turn	Average	Silane	64	MPa
		Max	Silane	77	MPa
Thermal	Integrated Shrinkage 77K–300K [L(77K) – L(300K)] / L(300K)			(2.65 ± 0.15) $x10^{-3}$	
Electrical	Electrical Insulation	LowVoltage	A few volts	$\geq$ 2.0 x 10^{7}	Ω
	Turn / Turn	High Voltage	300 volts	$\geq$ 1.3x 10^{11}	Ω
		(Turn/turn)	350 volts	0.7 - 6.0 x 10^{11}	Ω
			1800 volts	~ 10^{8}	Ω

3.2.2.2 Compressive Fuji Prescale Film

To verify the horizontal and vertical load on the conductor prior to heat treatment, a layer of mica and S-2 glass was replaced with Fuji Prescale Film®. The film has tiny corpuscles of ink that burst by varying amounts based on the pressure on the film. Figure 21 shows the distribution of force on the coils from the weight of the coffin retort lid alone on the left and from 20 ft-lbs of torque on 8 different 1”- 8 threads / inch bolts on the right.

The weight of the lid alone seems to place the most concentrated pressure on the left side of the lead end. Figure 22 shows the distribution of force on the coil from 40 ft-lbs of torque on the left and 75 ft-lbs of torque on the right using the same bolts. The coil is heat treated and impregnated at 75 ft-lbs. Once full pressure was reached the force on the central and middle piers seemed to be the strongest. The Fuji film verified that the force was relatively uniform on the coil.

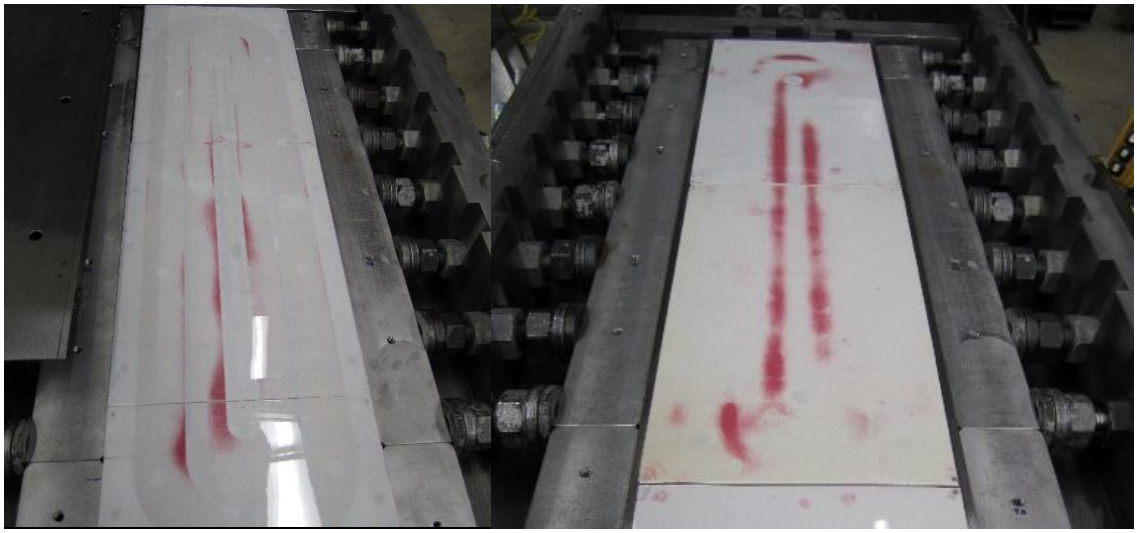

Figure 21: Fuji Film with Two Different Low Pressures

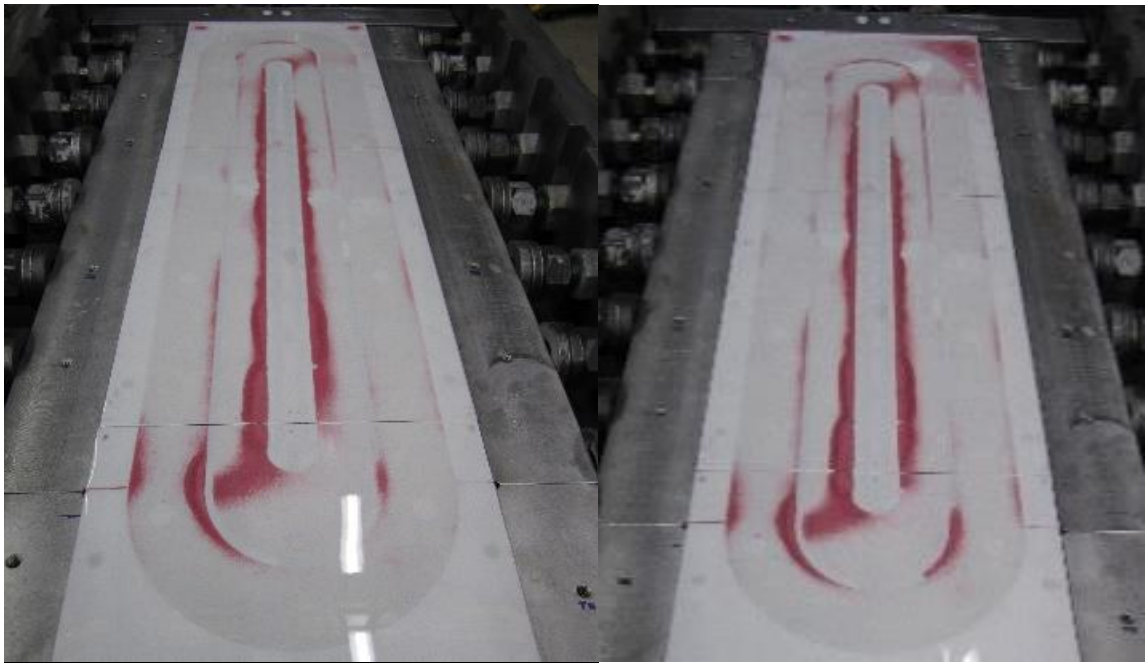

Figure 22: Fuji Film with Two Different High Pressures

3.2.2.3 Monument Measurement

Shoulder bolt monuments were incorporated into the piers to measure stress management structure location. These measurement were taken with just the magnet tooling and then after each coil was wound. By design, the cable loading during heat treatment was defined by cable compressibility and shimming to 300 psi. Therefore shoulder bolt measurements only gave verification that the stress management tooling was completely and correctly aligned and oriented. Figure 23 shows the location of the monuments. They are positioned on the central, middle, and outer piers for determining coil sizing.

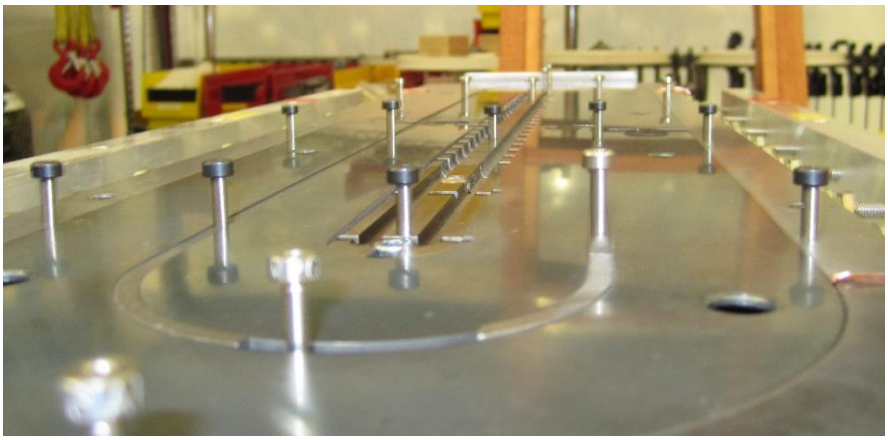

Figure 23: Measurement Monument Bolts

This verification is extremely important to detect gaps that would jeopardize load transferal between stress managing elements during magnet testing. Multiple rows of monument bolts were strategically employed to give confidence that the stress management structure is accurately located. Any gap between any pier and any beam was detected and corrected with theses monument measurements in conjunction with depth micrometer measurements.

3.2.2.4 Depth Micrometer Measurement

Shoulder bolt measurement is only possible when the magnet thin skin is removed. It is necessary to have information for structure location while loaded in the coffin and the thin skin present. Six holes on the lid and six holes on the coffin thrust bars were drilled to measure the stress management structure location under full coffin loading. Figure 24 shows the vertical and horizontal ports for measuring the outer dimensions of the coil.

During heat treatment each coil maintained the same vertical dimension but expanded in the horizontal direction. TAMU3b expanded by 0.007" on each side and TAMU3c expanded by 0.006" per side. The diameter and length of internal tin strands both increase during heat treatment [61] and thus this lateral coil expansion is expected.

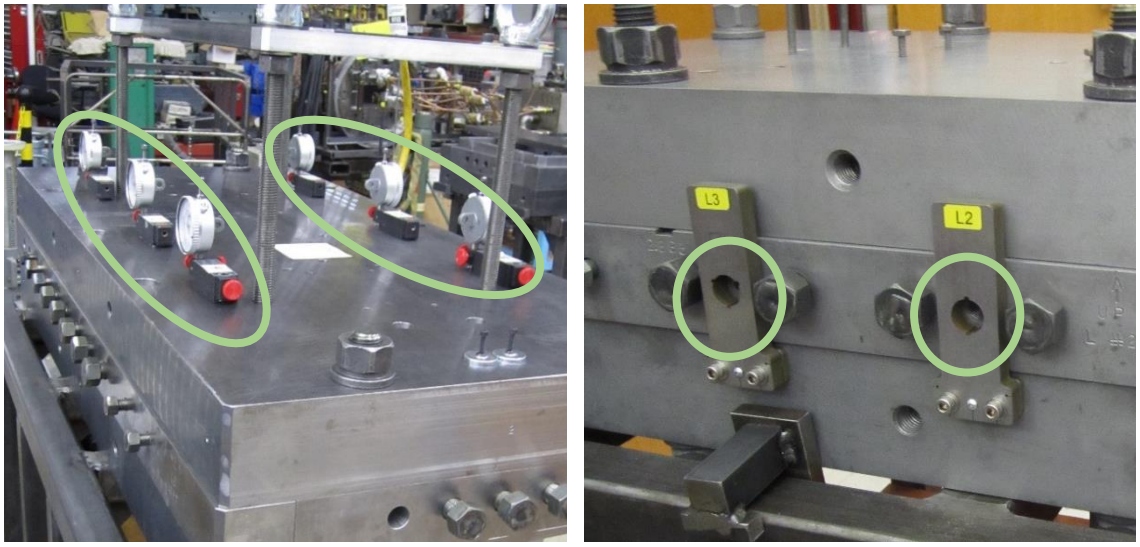

Figure 24: Vertical and Horizontal In-Situ Coil Measurement

3.3 Quench Simulation

The goal behind simulating a quench is to ensure the safe and repeatable operation of the magnet at cryogenic temperatures. The most important parameter to determine with simulation is the peak temperature rise and voltage in the conductor for different initial currents and protection circuitry. With this goal in mind there are several codes available to simulate the quench phenomenon in a dipole magnet. Opera has an expensive thermodynamics solver (TEMPO) and a quench solver that would work with Vector Fields. There is also OPUS and QUABER used at CERN [62], QUENCH written by M. Wilson [10], and a modified QUENCH code called QUCERN by A. McInturff [63]. There is also ANSYS [64], COMSOL, QLASA [65], QUENCHPRO, KUENCH, and a ROXIE quench subroutine [66] that simulate a quench after a cursory investigation. Each code has strengths and weaknesses.

Several simplifying assumptions can safely be made for TAMU3 that make the power of finite element not necessary. The same simplifying assumptions can also be made in comparable MgB_2 coils [67]. Additionally, the only tangible difference between finite element and integral solving codes such as QUENCH and QLASA is presentation and not necessarily accuracy of output.

3.3.1 Simulation Assumptions

First we assume the thermal dynamics are adiabatic with respect to heat conduction to the helium bath. The characteristic times for an impregnated magnet is small (~0.050 sec) and the thermal conductivity through an insulating barrier is small (~0.0001 k_{Cu}.) Both ensure the adiabaticity of the process.

Second we assume that the quench occurs in the high field region. By default a stress managed block coil geometry such as TAMU3 should not quench in the high stress region. This makes copper magnetoresistance calculations straight forward to include.

Third we estimate the effect of the protection heater as a step function heat source that acts on the covered portion of the coil after a diffusion delay time. In reality the quench must propagate from the top edge to the bottom edge of the Rutherford cable and then

between gaps of heater coverage (both ~0.00005 seconds at high field). However, these effects are dwarfed by the Kapton diffusion time (~0.020 seconds.) These two assumptions give a 'worst case scenario' for a quench. The protection heater is estimated as a step function heat source that acts on 70% of the coil after a diffusion delay time of 20 milliseconds. Following the prescription of Wilson [21], quench dynamics were simulated for both a quench originating in the outer conductor and a quench originating in the inner conductor.

3.3.2 QUENCH Code Requirement and Explanation

Over the temperature range that a quench occurs, the specific heat, resistivity, and thermal conductivity change anywhere between 2 and 4 orders of magnitude. The size of the quench zone and the speed at which it is growing is changing based on these highly dynamic parameters. The job of any quench code is simply to keep track of temperatures, identify the quench front, and conserve energy. Ideally the output should include the maximum temperature rise, the peak voltage, and the characteristic time of the quench. These three pieces of information are the most important for coil protection.

QUENCH simulates a quench by calculating the quench velocity in each direction based on conductor properties. The initial size of the quench is based on these velocities and the time step chosen for the simulation. The following equation gives the size change of the quench volume in one direction where J is the current density, γ is the density, ρ is the resistivity, k is the thermal conductivity, T_C is the critical transition temperature at the given background field, and T_0 is the operating temperature.

$$\Delta x = v\Delta t = \Delta t \frac{J}{\gamma C}\sqrt{\frac{\rho k}{T_C - T_0}} \quad \textbf{(1)}$$

Then the temperature rise in that volume is calculated based on the 'balance of heat' equation per unit volume where t is time and T is temperature.

$$J^2(t)\rho(T)dt = \gamma C(t)dT \quad \textbf{(2)}$$

The current in the magnet is reduced based on the magnet inductance and the temperature rise in the quench volume. Then another layer of thickness determined from equation (1)

is added to the quenched volume like the layers of an onion with each layer having its own temperature. This process is continued until the coil boundaries are reached by the quench front. Peak temperature occurs at quench origin, voltages are determined from the quenched layer resistance, and the characteristic time is found from the current decay.

Equation (2) is separable so that we have the following per unit volume equation:

$$\int_0^\infty J^2 dt = J_0^2 t_d = \int_{T_0}^{T_{MAX}} \frac{\gamma C}{\rho} dT \qquad \textbf{(3)}$$

Equation (3) is the most important for determining the protection of the magnet. The left hand side is determined by the current decay and thus mostly from magnet protection properties. The right hand side is determined only from conductor properties. For magnet protection a peak allowable temperature rise is determined and based only on conductor, a 'MIITS bank' (million amps^2 second) is calculated. The MIITS bank puts constraints on how fast the current of the magnet must be brought down or how small the characteristic time t_d must be for the peak temperature to remain safe.

Table 3: Important Cable and Coil Properties for Simulating Quench

Property	Value
Outer Coil Unit Cell .135 by 1.316 cm	0.179 cm^2
Outer Conductor Area (77.4%)	0.138 cm^2
Inner Coil Unit Cell .156 by 1.315 cm	0.205 cm^2
Inner Conductor Area (76.5%)	0.157 cm^2
Insulation Thickness (Single Turn)	74.9 μm
Outer Coil Unit Length	132.4 cm
Inner Coil Length	111.9 cm
Magnet Inductance	2.50 mH
I_c (Inner Conductor limited)	13.72 kA
B_c (Inner Conductor)	14.36 T
B (Outer @ I_c)	11.24 T
B_c (Outer @ I_c)	13.22 T

3.3.1 Input Parameters and Results

The conductor fractions are based on the OST RRP® 54/61 Internal Tin strand (0.8 mm and 0.7 mm diameter for the inner and outer conductors.) Material properties were gathered from the Brookhaven Selected Cryogenic Data Notebook [68]. The important properties of the cable and magnet for quench simulation are given in Table 3.

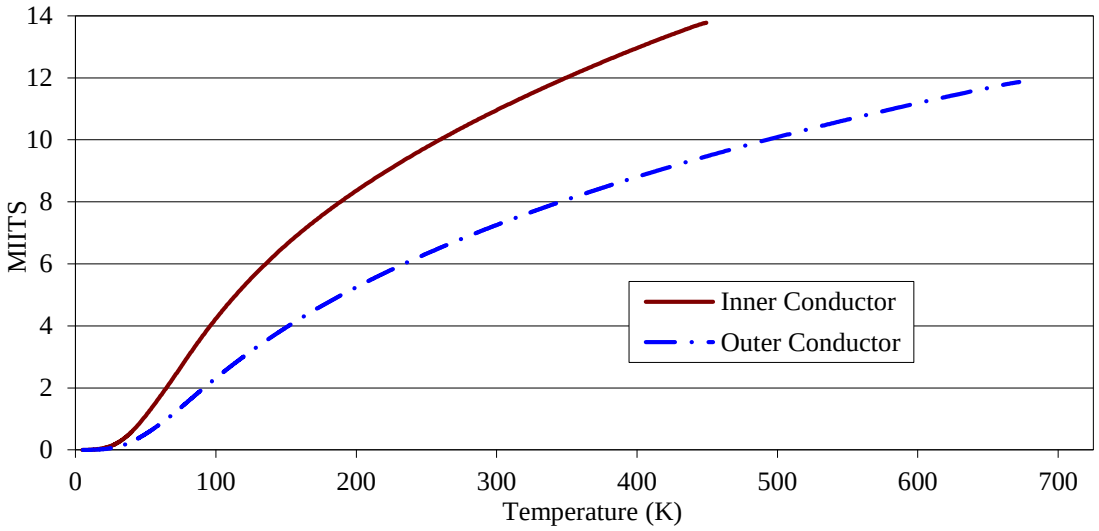

Figure 25: MIITS Curve for Inner and Outer Conductor

All simulations have an initial current that produces the highest temperature rise in the conductor (13.72 kA 11.24 T for the outer coil and 13.69 kA and 14.33 T for the inner coil.)

The primary output for the code is shown in Figure 25 by way of the MIITS curve. The quench integral is much smaller for the outer conductor because the cable cross section is 13% smaller and the RRR is 10 for the outer conductor and 30 for the inner conductor. The MIITS quench integral will reveal what the peak temperature of the conductor is from magnet trace data.

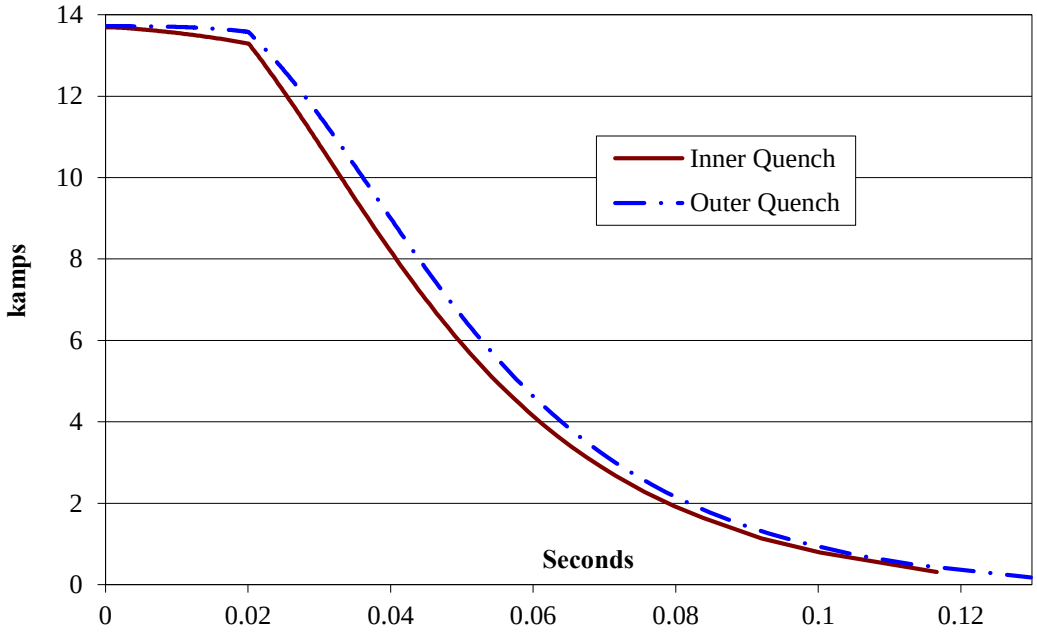

Figure 26: Current Decay for Simulated Quench

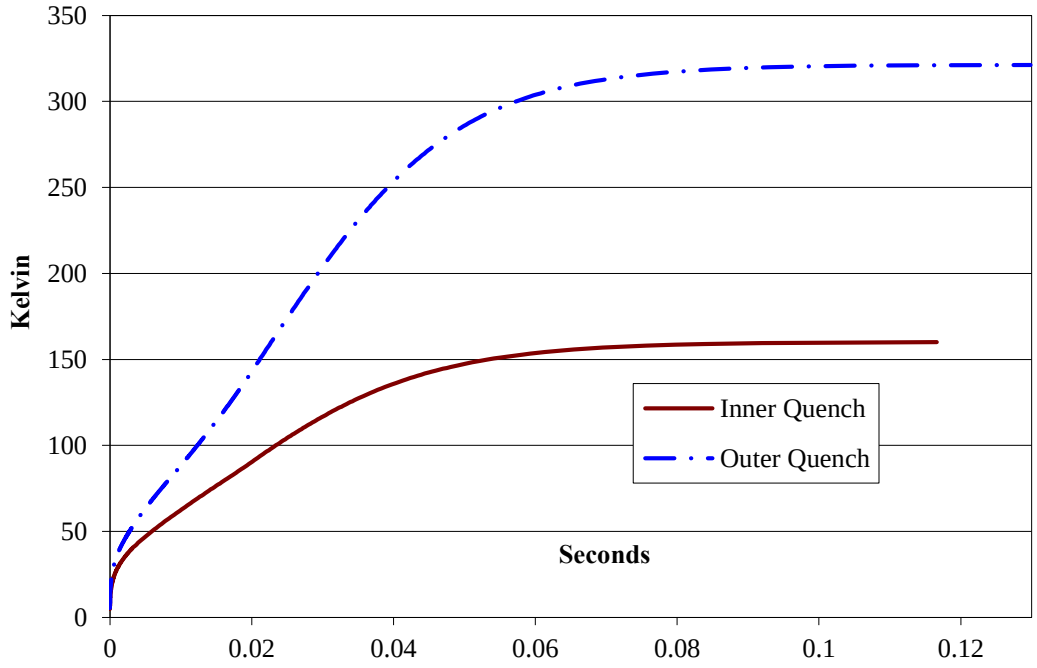

Figure 27: Temperature Rise for Simulated Quench

Figure 26 and Figure 27 show the current decay and temperature rise after a quench with protection heaters initiating a coil wide quench after 0.02 seconds. The protection heaters keep the peak temperature below 200K in the inner conductor for an inner coil quench. For an outer coil quench the peak temperature still exceeds room temperature. Above 380K Formvar insulation softens [69] and the outer coil stays safely below that at 321K. The characteristic time is 0.06 s and 0.056 s for an outer and inner quench. The peak internal voltage is 667 and 643 distributed volts for the inner and outer coils respectively.

3.3.2 Required Quench Protection Coverage

From the quench integral output an estimate can be made for what fraction of the coil needs to be covered by a protection heater and how fast the heater needs to be fired. The quench integral gives a 'MIITS bank' for a given final peak conductor temperature T_f where MIITS is the standard million amps^2 second unit. Following the approximation of Iwasa [69] the coil resistance, *R*, is the resistance of the coil at T_f divided by four, where ½ comes from spatial averaging and another ½ comes from time averaging. So that

$$MIITS(T_f) - I_0^2 t_d = I_0^2 \, L/R \tag{4}$$

where

$$R = \frac{\rho(T_f)}{4A} L_{cable} f. \tag{5}$$

For Equation (5), A is the cable cross section, ρ is the cable resistivity, L_{cable} is the length of cable, and f is the fraction of the coil under the protection heater.

For TAMU3, a heater power of 45 W/cm^2 will set the detection and diffusion time to roughly 10 ms based on insulation thickness and previous experience. From the graphs of the previous section and a 20ms diffusion time, the protection heater should only allow a peak temperature of 321K and not 380K+ as the formula suggests. This equation puts an upper bound to the peak temperature whereas the code gives a much more accurate estimation.

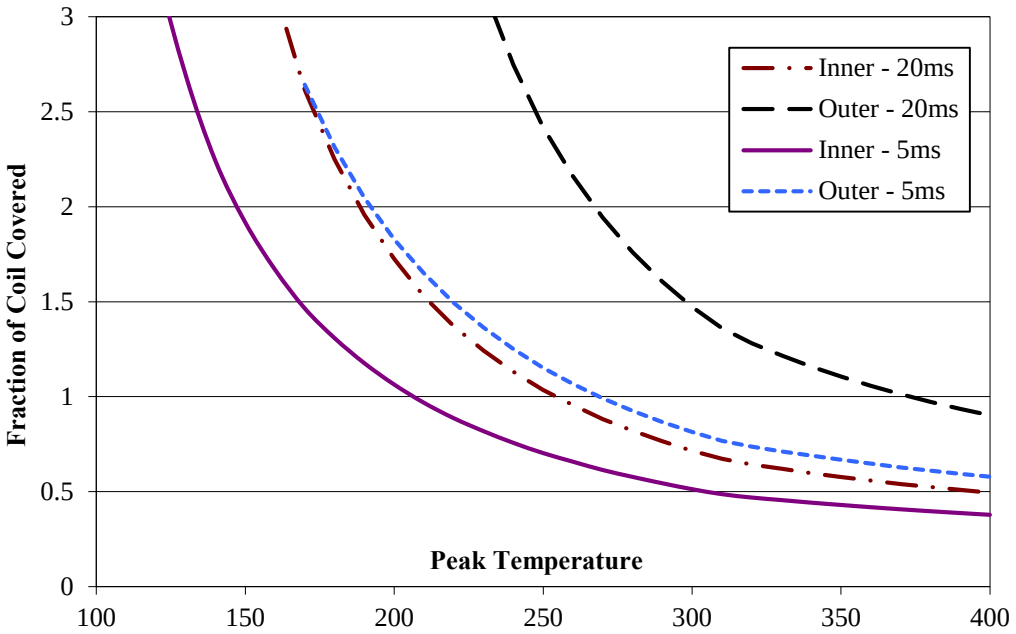

Figure 28: Required Coil Coverage Fraction as a Function of Peak Temperature

Figure 28 gives the required fraction of the coil covered by a protection heater for a given peak temperature as calculated from the quench integral and from a delay time indicated in the key (20 and 5 ms.) A value of greater than one implies that energy will need to be removed by an external dump resistor with a value determined by the amount greater than one.

3.4 Quench Protection Design

The stored energy at peak field is 0.24 MJ in TAMU3. When a section of the magnet no longer is superconducting or quenches the energy is deposited in the form of resistive heating in the quenched region. Without any protection the peak temperature rise in the small zone can be in excess of 1000 kelvin or enough to melt insulation or conductor and destroy the magnet in fantastic fashion. Therefore, quench detection and protection is very important in superconducting magnets.

3.4.1 Voltage Taps and Signals

Quench detection is accomplished with a series of voltage taps strategically located on the first and last turns of the inner and outer windings where quench is most likely to occur. Figure 29 shows the location of the voltage taps and quench protection heater strips at the lead end. TAMU3b and TAMU3c are symmetric coils in TAMU3 so that comparative circuits will measure voltage differences between corresponding voltage taps. The induced voltages from ramping the magnet should produce opposite and symmetric voltages that will be cancelled with a comparator circuit. Then any voltage developed from a quench is isolated from AC or ramping signals and will be used to detect a quench.

Figure 29: Voltage Tap and Quench Protection Heater Installation

Carbon resistors on each lead measure temperature rise and give a secondary quench detection signal. Depending on where the quench originates and quench velocity we may see temperature rise before the quench detection circuitry fires due to the relatively large Nb_3Sn margin in comparison to NbTi.

3.4.2 Quench Protection

Quench protection in TAMU3 is accomplished with an external dump resistor and an internal heater foil. The dump resistor is connected across the leads during a quench so that some of the energy stored in the magnet inductance is dumped into the resistor outside of the magnet and decreases the peak temperature rise in the magnet. The dump resistance is calculated so that the peak voltage across leads is less than 1000 volts or roughly 50 mΩ.

The primary protection for TAMU3 is accomplished with a heater foil. The heater is as thermally close to the windings as possible while remaining electrically isolated and covers roughly 70% of each coil. When a quench is detected a capacitor bank drives current through each foil on the order of 45 W/cm^2 and raises the temperature above the superconducting critical temperature and drives the majority of the volume of the coil into quench. With a large quench region the deposited energy is distributed and the peak temperature is greatly reduced. With effective quench protection the peak temperature is simulated to remain below 200 kelvin.

3.5 Spring Design

Laminar springs were designed and fabricated in TAMU3 to provide two crucial stress managing functions. Primarily they give mechanical separation between the inner and outer windings to inhibit transfer of stress. Secondarily they provide preload to the outer windings. The spring must have sufficient travel and high enough spring constant at both cryogenic and reaction bake temperatures to accomplish this task. All the while the spring profile must be as small as possible to maximize the space for conductor. Inconel X-750 was chosen for its excellent strength at reaction bake and cryogenic temperatures.

3.5.1 Spring Design Parameters

A schematic of the spring profile is shown in Figure 30. The Inconel X-750 spring and load spreaders used in TAMU3 were precipitation heat treated under the AMS specification #5598 heat treatment schedule to obtain the necessary spring strength [70-72]. The heat treatment is in argon to 1350ºF (732.2ºC) for 8 hours and then furnace cool and hold to 1150ºF (621.1ºC) for a total precipitation-treating time of 18 hours with a final argon cool. This heat treatment allows Ni3Al, Ni3Ti, as well as trace carbides to form creating a 32 – 42 HRC hardness and a modulus of ~30,000ksi at room temperature. All test samples from the precipitation heat treatment were between 34.8 and 39.8 HRC with an average of 37.3 HRC. The springs were designed to have a repeatable travel of about 0.006" before extensive plastic deformation. The absolute maximum travel is designed at about 0.012" after plastic deformation.

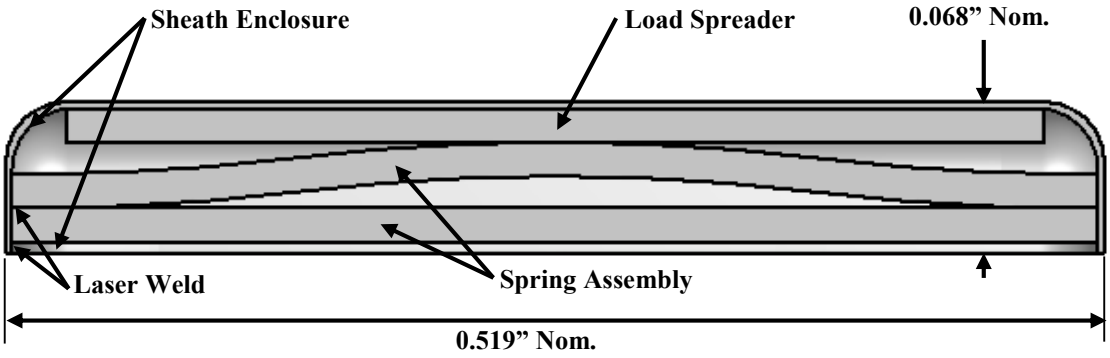

Figure 30: Schematic Diagram of Laminar Spring

The springs were then assembled and laser welded into a hermetically sealed can to maintain travel after epoxy impregnation. The springs are placed between the middle pier support structure and the outer coil during winding. The spring provides preload during the Nb_3Sn reaction bake and epoxy impregnation and absorbs pier deflection during magnet testing.

Figure 31: TAMU3 '10-Stack' Laminar Spring

The Nb_3Sn formation stage of the reaction bake is 670ºC for 70 hours. This temperature is almost 50ºC above the lower stage of the precipitation heat treatment. This poses several concerns about how the behavior of the springs might be altered from the reaction bake. The spring may have a zero point shift, a spring constant change, a travel decrease, or any combination of these three. Extensive testing and simulation was performed on a set of springs to observe the effect of heat treatment on the spring integrity.

3.5.2 TAMU3a Spring Analysis

TAMU3a springs were dimensioned before and after reaction bake. A summary of the average widths for the three straight springs are in Table 4 below. One can see that there was a 0.004” zero offset on the short lead-end spring and a 0.010” zero offset on the curved springs.

Table 4: TAMU3a Spring Thickness

Inches	Pre RXN	Post RXN	Zero Offset
Long Spring	0.0683	0.0663	0.0020
Middle Spring	0.0676	0.0660	0.0015
Short Spring	0.0681	0.0636	0.0044
Curved Spring	0.068	0.058	0.010

The high offset of the curved spring indicate that during the winding process the spring is plastically deformed until completely flat. This is expected due to the capstan force from each turn. The total capstan force is about 700 psi which is enough to plastically yield the spring according to simulation. The other zero offsets are largely unexpected and a series of experiments were designed so that the possible effect of heat treatment on the temper and hardness of the springs could be tested. It was thought that perhaps the heat treatment was softening the spring to the point that it was taking a set under the standard 300 psi target pre-load pressure on each spring.

3.5.3 TAMU3 Spring Testing

Previous tests were performed on post reaction bake 10-stack springs at too high of a pressure. The results of one such test is shown in Figure 32. One can see a resemblance of a linear regime for the spring up to 2000 psi for this test and complete plastic deformation of the spring afterward.

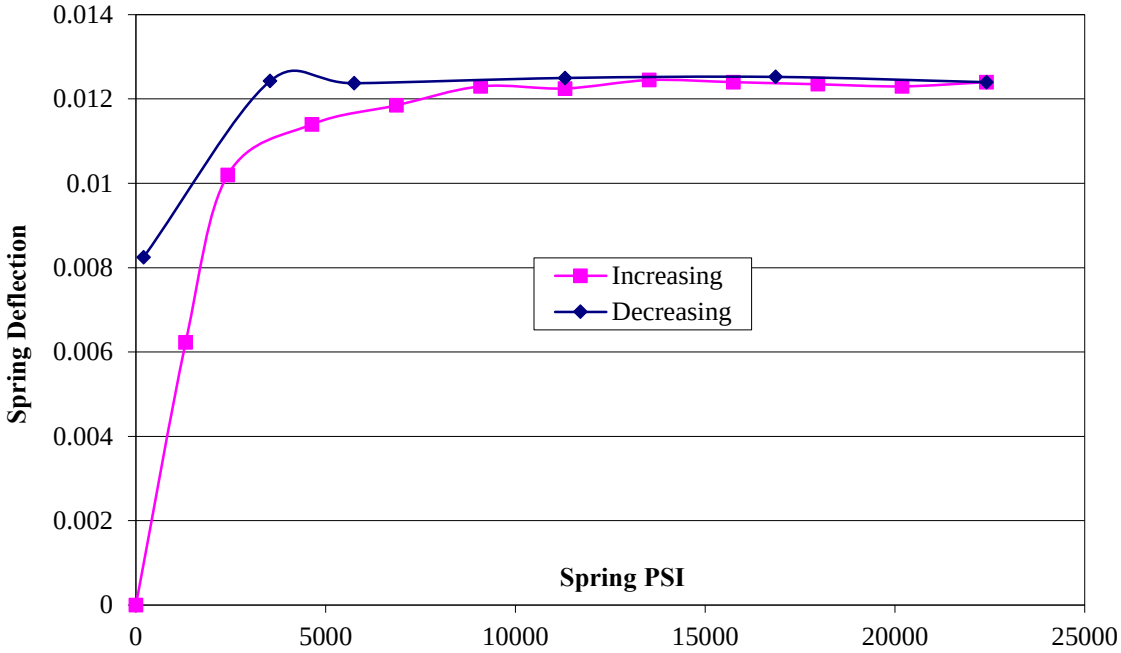

Figure 32: TAMU3 Spring Compressed at Room Temperature

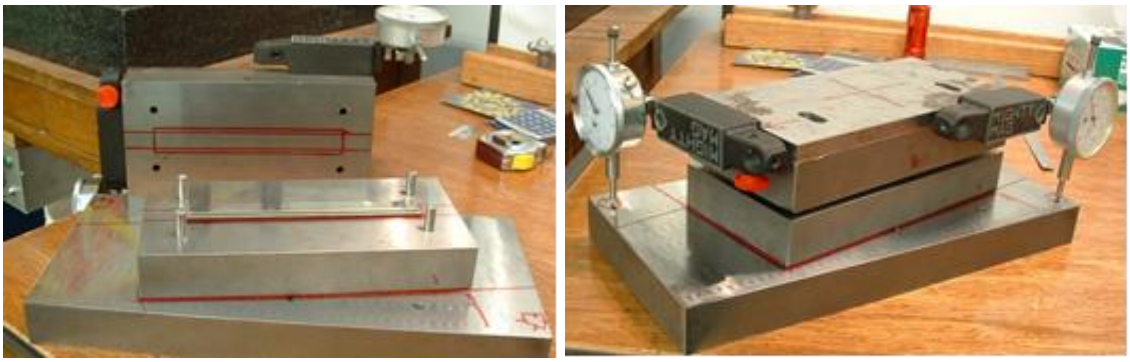

Figure 33: Spring Test Fixture

The response of an unused TAMU3 10-stack spring was measured both before and after the heat treatment to 100, 200 and 300 psi. The same spring was then compressed to 300 psi and heat treated under load. Pictures of the experimental setup are shown in Figure 33 and Figure 34. The spring dimension as a function of pressure from before and after

the reaction bake is shown in Figure 35 and Figure 36. The spring zero point shifted by about 0.001" from 300 psi compression as evidenced by Figure 35. This is expected since there is a concentration of stress at the outer welds that will be discussed in simulation.

Figure 34: Spring Test Setup and Heat Treatment Fixture

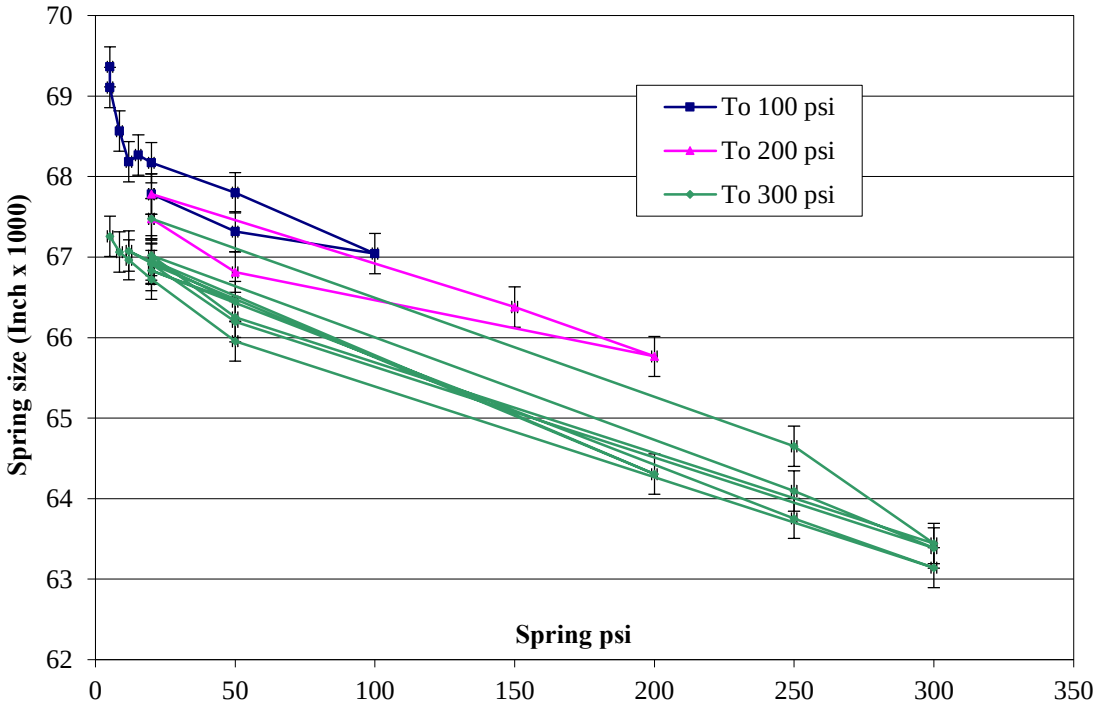

Figure 35: Spring Compression Before Heat Treatment

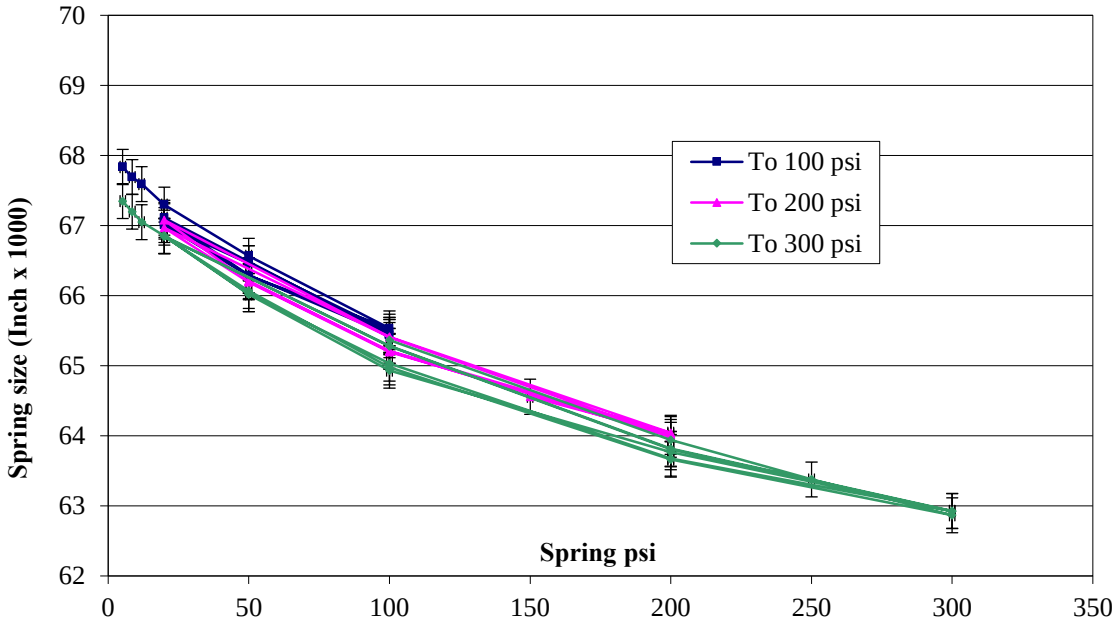

Figure 36: Spring Compression After Heat Treatment

After the heat treatment more data points were collected and Figure 36 reveals a quadratic shape. At 300 psi the dimension of the spring is about 0.063" both before and after heat treatment. Also at 25 psi the dimension of the spring is about 0.067" both before and after heat treatment. Remarkably, baking the spring at 670°C for 70 hours had no significant effect on the spring constant or the spring travel!

3.5.4 TAMU3 Spring Simulation

Testing the springs directly revealed that the heat treatment did not appreciably change the spring constant. The springs were modelled and simulated with ALGOR to compare the response with what would be expected with standard properties of precipitation hardened Inconel X-750. Values for the modulus, yield, and tensile strengths at 25% elongation are 30×10^6 psi, 135 ksi, and 186.5 ksi respectively as taken from the Inconel X-750 Publication No. SMC-067 from Special Metals Corporation for strip in AMS specification #5598 heat treatment condition [72]. For simulation the complete

stress-strain relationship for Inconel X-750 at room temperature was used from the Selected Cryogenic Data Notebook from Brookhaven [68]. The analysis type was the Mechanical Event Simulation (MES) solver with nonlinear material models. This solver employs von Mises stress with kinematic hardening. This is ALGOR®'s most advanced and computationally intensive mechanical solver for metal simulation. The von Mises yield criterion for two dimensions is given as

$$\sigma_{von\ Mises} = \sqrt{\sigma_{xx}^2 + \sigma_{yy}^2 - \sigma_{xx}\sigma_{yy} + 3\tau_{xy}^2} \quad \textbf{(6)}$$

where σ_{xx} and σ_{yy} are the principal stresses and τ_{xy} is the shear stress. For the simulation it was assumed that there is a 300 psi force on the spring which is the target designed compression.

The two-fold symmetry of the spring was taken advantage of to reduce the computational requirement. For Figure 37, Figure 38, and Figure 39 the right hand side has a rolling symmetry boundary condition. The bottom is also a rolling boundary condition where the bottom right node is fixed. Figure 37 shows the uncompressed spring for comparison.

Figure 38 shows that the peak stress is on the load spreader along the centerline of the spring on the right hand side. The peak stress in the spring itself is near the yield strength of Inconel X-750 at 135 ksi and is located at the weld near the left edge of the spring.

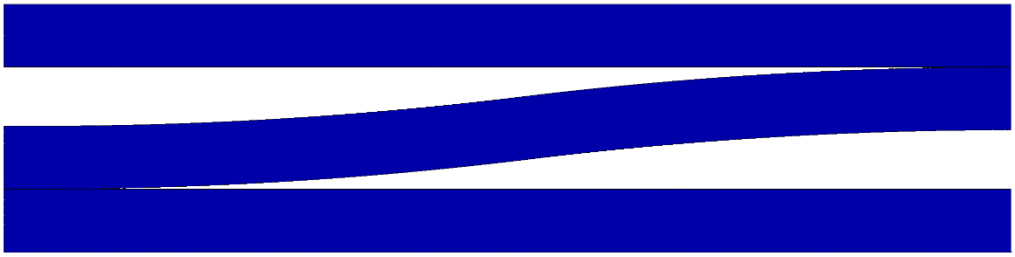

Figure 37: Simulated Uncompressed Spring

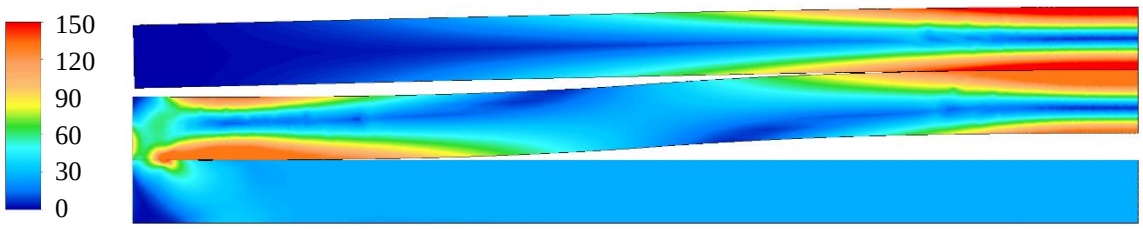

Figure 38: Designed von Mises Stress in ksi

The displacement of the spring is 0.085 inches at 300 psi according to Figure 39. From Figure 35 and Figure 36, the measured displacement was 0.005 inches at 300 psi. This is roughly 0.003 inches more compression that was simulated. If cryogenic material properties are used for Inconel X-750, then essentially the simulation and the measurements coincide even though the yield strength only increases by 10%. This result indicates how material properties can have a large effect on spring displacement.

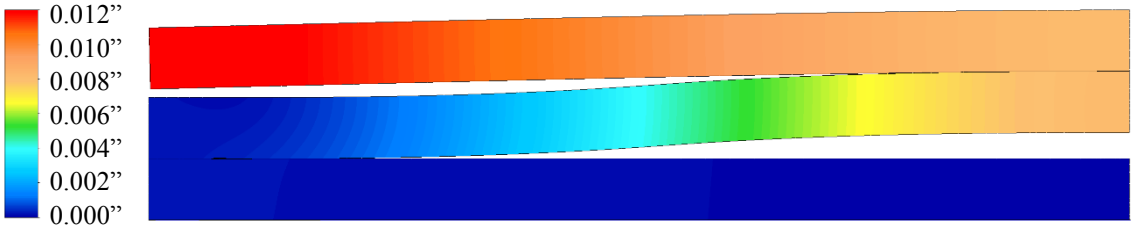

Figure 39: Simulated Spring Displacement at 300 psi

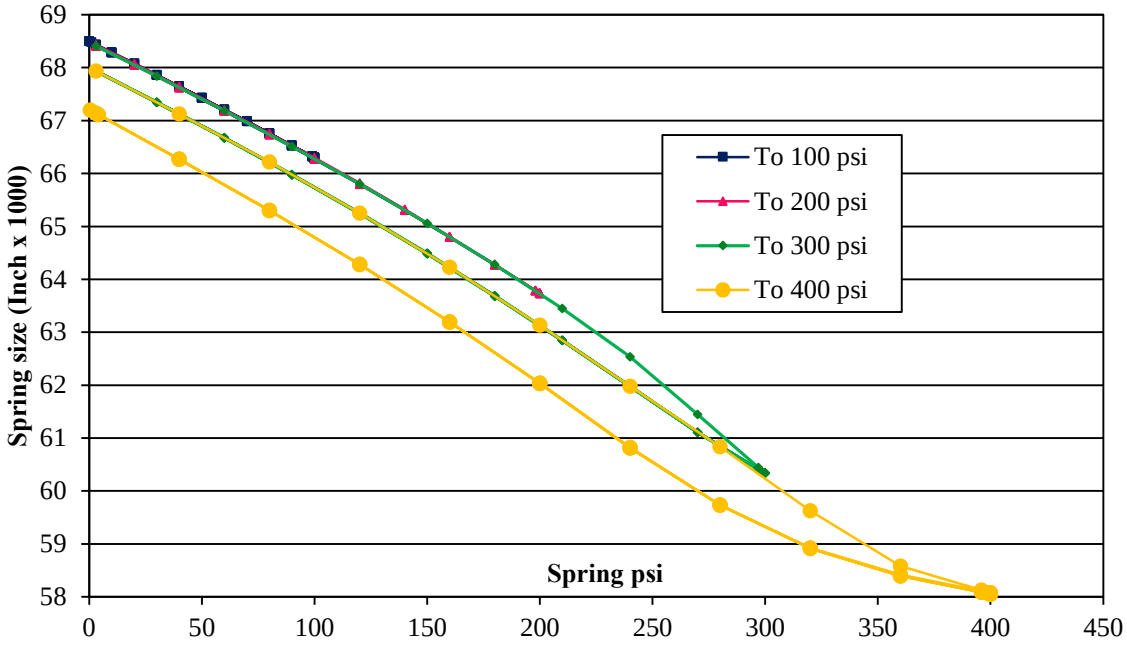

Figure 40: Simulated Spring Displacement as a Function of Pressure

The simulation as shown in Figure 40, implies that there should be about a 0.0005" zero offset from 300 psi. Actual spring measurements indicate that a 0.001" offset is produced from 300 psi. At about 360 psi on the load spreader the outer edge touches the curved piece of the spring. This artificially causes the tail end of the curve to artificially curve up in Figure 40. The average spring zero offset from TAMU3a reacted springs was 0.002". This indicates that the winding procedure produced about 400 psi peak on the TAMU3a springs.

4. TAMU3 CONSTRUCTION

Constructing Nb_3Sn superconducting magnets is an involved intricate process. The initial tooling and superconductor must be fabricated and quality checked. Each coil is then wound and subsequently heat treated to form stoichiometric Nb_3Sn in the Rutherford cable. After heat treatment the coil is filled with epoxy to fill void space, minimize conductor movement while testing, and increase resistivity between turns. The final steps are to install the coils in a flux return and to test the entire magnet assembly.

4.1 Rutherford Cabling

The strand is from Oxford Superconducting Technology (OST) through the Conductor Development Program (CDP). The high internal tin 54/61 Restacked Rod Processed (RRP®) strands are 0.7 mm diameter for the outer windings (34 strands) and 0.8 mm for the inner windings (30 strands). The strands were cabled by the Supercon group of the Accelerator and Fusion Research Division (AFRD) at Lawrence Berkeley National Lab. The Rutherford cable was insulated by a new fine-filament (5.5 μm) S-2 glass drawn by AGY in South Carolina and braided directly on the cable by A&P Technologies in Ohio [60].

4.1.1 Original Cable

Original conductor for TAMU3 was cabled in 2006 and all information has come from the ARL cable log and the LBNL cable logs. The inner conductor is 0.8 mm OST RRP® Nb_3Sn. Figure 41 shows a picture of TAMU3 inner cable from LBNL. The inner cable was first rolled to 9.2% compression, then annealed, and then rolled to 11.7% compression. Each anneal was at 205°C for 4 hours to release the intrinsic strain between the niobium rods and copper stabilizer. The outer cable was first rolled to 9.9% compression, then annealed, and then rolled to 12.3% compression. We then attempted to insulate the outer cable with S-2 glass but the cable deregistered. The cable was then annealed again and rerolled to 13.5 to 14% compression to increase the mechanical

stability of the cable. Insulation was then successfully braided onto the outer cable. The processing of original TAMU3 conductor is summarized in Table 5.

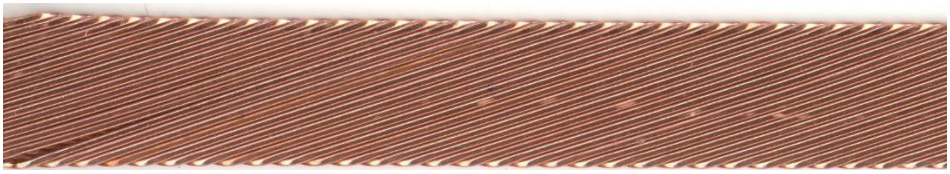

Figure 41: Uninsulated TAMU3 Inner Rutherford Cable

Table 5: TAMU3 Original Conductor Summary

Conductor	Width	Thickness	% Compression
TAMU3 inner cable	30 strands x 0.8mm		
T4O-B0937-BR	75 Meters		
Unstrained		0.0630”	0.0
First Roll		0.0572”	9.2
Re-Roll After Anneal	0.5120”	0.0556”	11.7
TAMU3 outer cable	34 strands x 0.7mm		
T-5-O-B0943RR-1&2	110 Meters (total)		
Unstrained		0.0551”	0.0
First Roll		0.0496”	9.9
Re-Roll After Anneal		0.0483”	12.3
Re-Roll After 2nd Anneal	TAMU3a 0.5133”	0.0474”	14.0
Re-Roll After 2nd Anneal	TAMU3b 0.5120”	0.0477”	13.4

After heat treating TAMU3a, sufficient amounts of tin leaked out of the conductor and etched stabilizing copper from the leads that it was deemed irresponsible to incorporate the coil into the TAMU3 magnet. This required a replacement coil be fabricated with new conductor. Enough inner conductor was initially made in 2006 for additional coils so that a replacement inner coil could be wound. However, more outer conductor needed to be fabricated.

4.1.2 Rutherford Cabling at LBNL

To fabricate new outer conductor for TAMU3 and future magnets, over 4 km of 0.7 mm RRP® strand was procured. The strand was the spooled onto 34 bobbins to fabricate 110 meters of Rutherford type cable at LBNL.

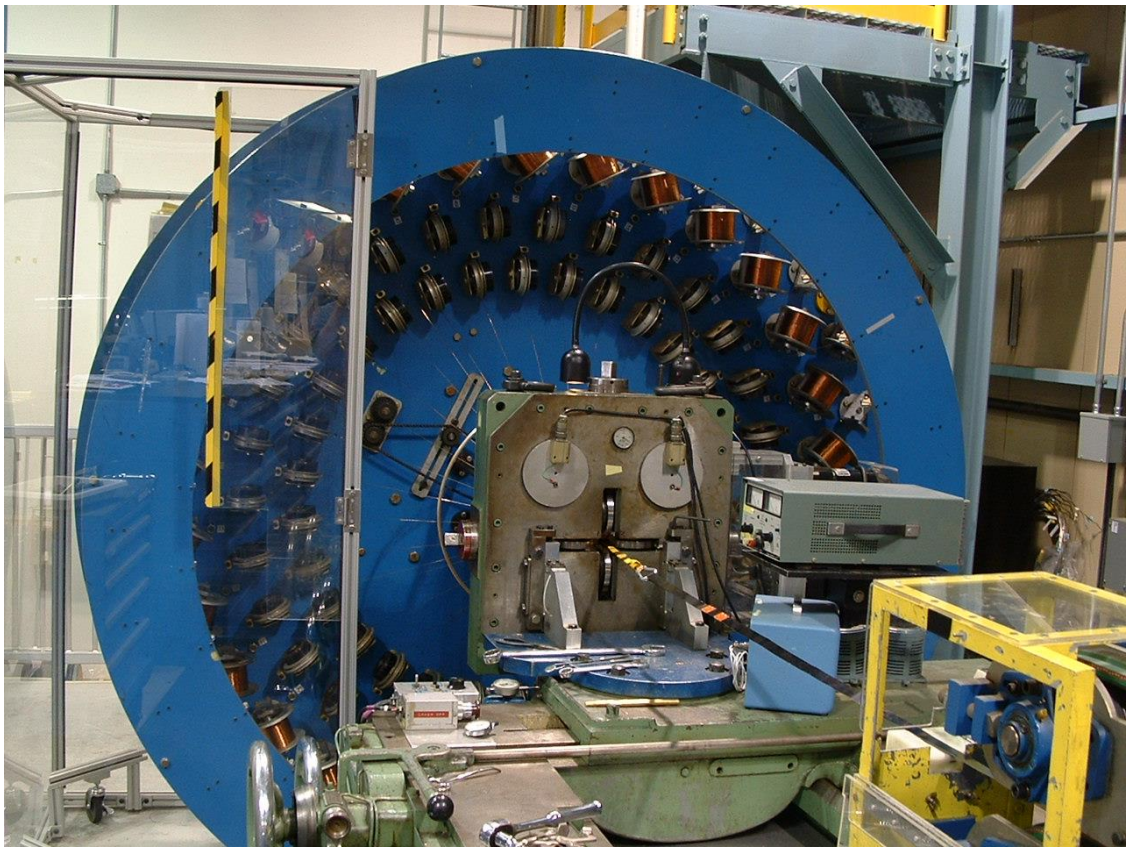

Figure 42: LBNL Cabling Machine

The cabling machine in Figure 42 rotates anywhere between crawling speed to roughly 80 rpm producing a maximum of 10 meters per minute with 60 strands. With the TAMU3 outer conductor we have 34 strands at 0.7 mm diameter. We were able to go to

~30 rpm before the Turk's Head DC motor was current supply limited which produced about 2 meters per minute. It took about 2 hours to make the 110 meters of outer 0.7mm RRP cable.

The Turk's head is warmed to ~40°C prior to cabling to minimize die spacing oscillation. The Turk's head and die rollers are located on the right hand side of Figure 43. The caterpillar cable take up, located on the bottom right side of Figure 42, is geared directly to the lathe and set to the ideal pitch length per rotation. The actual rate of take up is determined by the two Turk's Head motors that are independent of the lathe. The adjustment is made so that there is the minimal amount of tension on the cable between the Turk's Head and the Caterpillar cable take up.

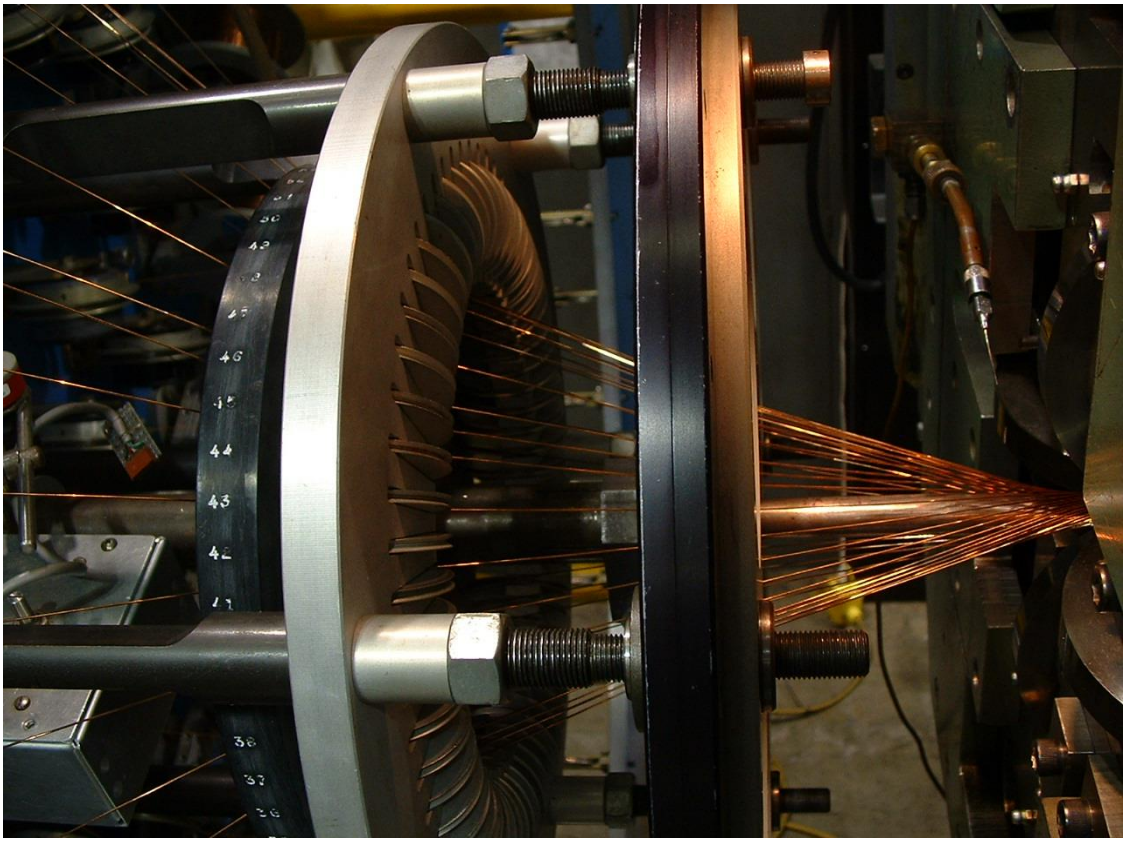

Figure 43: Turk's Head and Naphtha Lubricant Drip

The Naphtha nozzle is connected to a liter size container of Richards Apex V-4BR CPD vanishing fluid which is an evaporating oil for cabling with fatty additive plus (rust) inhibitor. The nozzle is shown on the right hand side of Figure 43. Hugh Higley from LBNL indicated that it is Naphtha with <5% of a fatty vegetable acid. He did not know if it was palmitic acid or not but it is strongly suspected that it is. As for the inhibitor, we deduced that it inhibits copper oxidation and could be benzotriazole ($C_6H_5N_3$), which forms a passive layer on the surface. The solution is applied directly onto the cabling mandrel without dripping onto the strands. The solution is applied at the rate of about one drop per pitch length or one roughly 1 ml every 3 meters or 15 ml in one winding set of TAMU3. Napalm is a mixture of one of the products of Naphtha and Palmitic acid.

A cable dimension measurement is taken every 0.8 meters along the cable. The length of cable is measured at the dimension measurement device shown in the middle of Figure 45 and at the SS cable anneal spool. The same reduction schedule was used for both the inner and outer cables as was originally used for TAMU3a conductor. Figure 44 shows the LBNL cabling team hard at work re-rolling TAMU3 outer Rutherford cable.

L to R; Alfred McInturff, Nate Liggins, Hugh Higley, Dan Dietderich

Figure 44: Cabling Assembly Line

Before annealing the entire cable set, we ran a test on short segments of bare wire. From past experience, if there was a local barrier break during the anneal, the strand would fracture at small bending radii from hard bronze forming. The 0.7 mm uncabled strands remained soft and pliable after an anneal at 204°C for 4 hours in a purged (10x the volume overnight) atmosphere. After the anneal the Turk's Head was moved to the end of the cabling lathe in front of the cable dimension measurement device to aid in rerolling the cable to its final dimensions (~3% reduction in thickness).

Figure 45: Automatic Cable Measurement Equipment

In summary, 110 meters of TAMU3 outer conductor was fabricated at LBNL with very simular dimensionality as the original Rutherford cable. It is worth mentioning that the original cable went through two anneals and re-rolls whereas the new outer conductor went through a single anneal and subsequent re-roll.

Table 6: TAMU3 Outer Cable Summary

Conductor	Width	Thickness	% Compression
New outer cable	34 strands x 0.7mm		
TAMU-5-O-B1029R	110 Meters		
Unstrained		0.0551”	0
First Roll		0.0489”	11.4
Re-Roll After Anneal	0.5127”	0.0475”	13.9
Original outer cable	34 strands x 0.7mm		
T-5-O-B0943RR-1&2	88 Meters (total)		
Unstrained		0.0551”	0.0
First Roll		0.0496”	9.9
Re-Roll After Anneal		0.0483”	12.3
Re-Roll After 2nd Anneal	TAMU3a 0.5133”	0.0474”	14.0
Re-Roll After 2nd Anneal	TAMU3b 0.5120”	0.0477”	13.4

4.2 Winding

After the magnet is fully designed and sufficient tooling is fabricated, winding commences. Winding superconducting magnets takes patience and precision. Failing to follow protocol or rushing will surely bring more heartache than efficiency. Included below are the novel techniques and nuances discovered while winding the TAMU3 coils.

4.2.1 Lead / Transition Tolerances

The original design placed too tight of constraint along the transition region of the leads. Shorts quickly formed from the winding procedure which required modifications to the nose piece and transitions on the base caps as shown in Figure 46. The top image is of the inner lead transition on the nose piece before modifications to widen the cable channel. The bottom image is after the modifications.

The field and thus Lorentz force on the leads is sufficiently decreased to about 10% of the force on each turn in the body. The magnetic flux density along the center of each lead and solder joint is shown in Figure 47. The decreased force enabled us to fill the relaxed tolerance S-2 fine filament glass fabric and tape. The extra tape also protected the leads from a propensity to form shorts. The best practice in designing hard bends is to

allow the cable some freedom. Tightly constraining Rutherford cable usually results in hard shorts to the transition tooling even if additional insulation is employed.

Figure 46: Inner Coil Nose Piece Transition Modifications

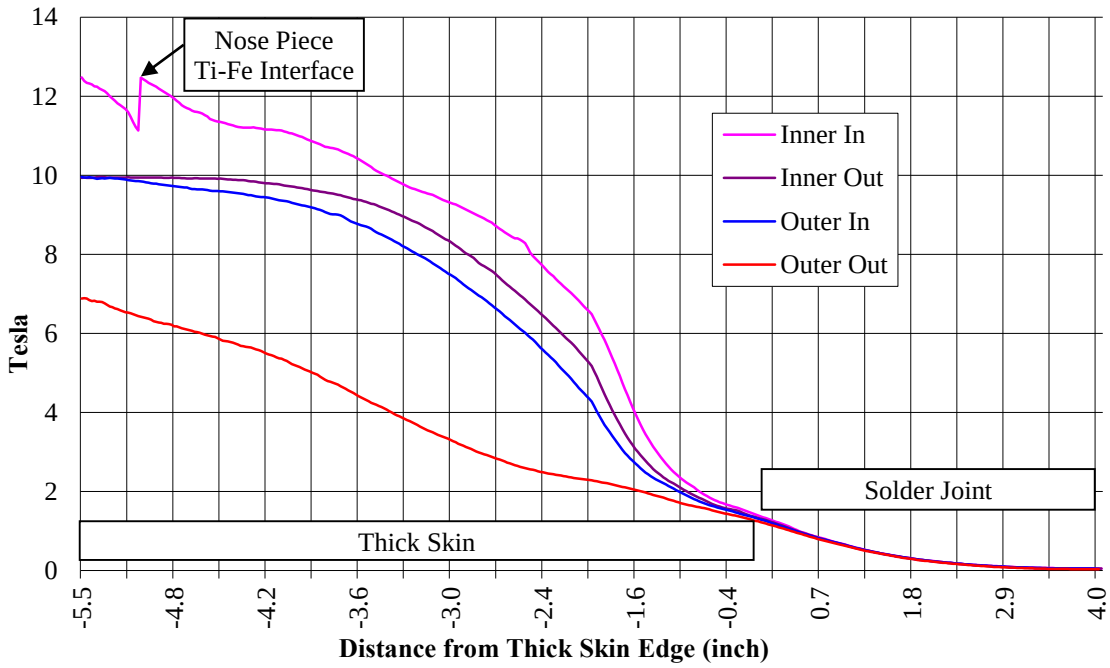

Figure 47: Magnetic Flux Density Along the Leads

4.2.2 Bottom Beam Orientation and Insulation

The original bottom inner beam design had pieces with undefined orientation and caused gas flow and epoxy channel misalignment. An inner winding was almost completed before this error was discovered and corrected in the design. In Figure 48 the top two segments of the bottom inner beam have gas flow / epoxy channel holes that misalign with the magnet base.

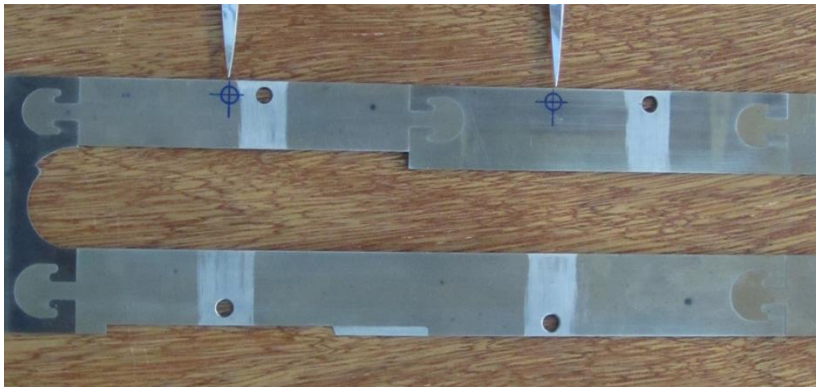

Figure 48: Bottom Inner Beam Epoxy Channel Holes and Misalignment

Once a turn is in place, it is imperative to minimize movement that tends to fray the delicate sock on the conductor and the blanket underneath the conductor. This is essentially impossible while winding a racetrack type coil, because the straight sections bow and form a catenary curve. The best practice is to place a thin sheet of a polyimide such as Kapton between the conductor and the S-2 glass blanket while winding and remove the sheet after the winding is complete.

4.3 Diffusion / Formation Heat Treatment

After magnet winding is complete the magnet is installed into a large magnet retort called a coffin for maintaining vertical and horizontal magnet pressure during the diffusion / formation heat treatment.

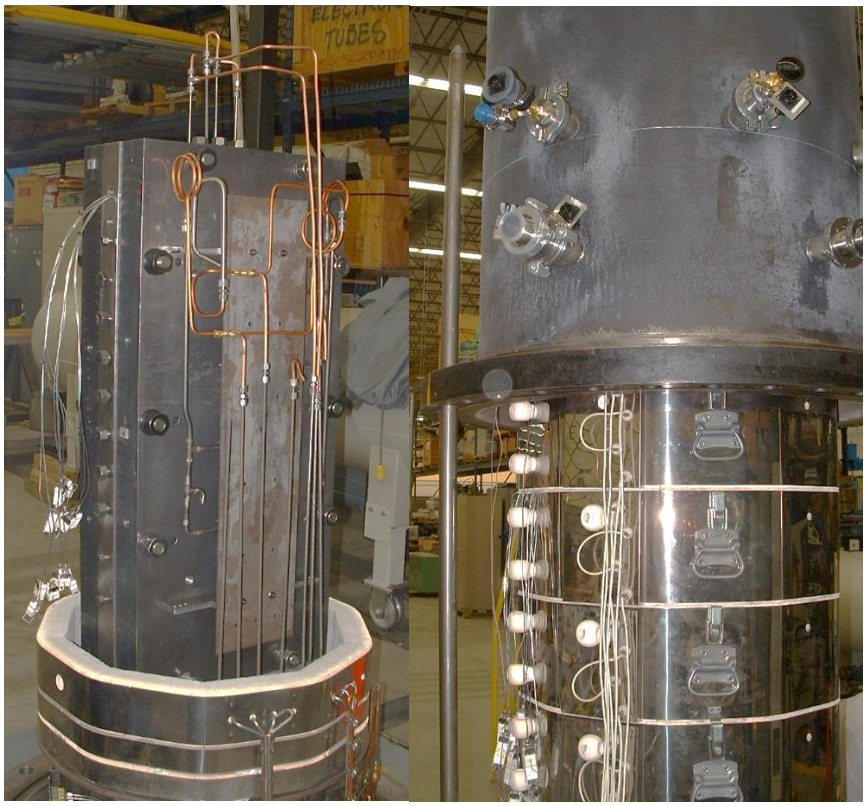

Figure 49: Heat Treatment Elements, Thermocouples, and Gas Lines

A positive pressure of argon flows through each coil to minimize oxidation. The left picture in Figure 49 shows all of the argon supply and return gas lines connected to the 900 kg retort. The right picture shows the ceramic heating elements surrounding the retort and the thermocouples protruding between layers. The top bell jar is the vacuum chamber for pump / purge process. The picture in Figure 50 shows the data logging cart and heat treatment vessel in the foreground and the temperature control electrical box in the background.

Figure 50: TAMU3 Heat Treatment Equipment

The relative mass of the retort compared to the heat available from the 480 V heating coils is quite disproportional. The response lag time is on the order of 30 minutes or a small eternity for standard temperature control processing. The system is underpowered and required tedious calibration and furnace characterization to maintain close control on conductor temperature. For more information on the heat treatment procedure see the heat treatment appendix.

The heat treatment for TAMU3 Nb_3Sn conductor has three steps: a solid stabilization step below the melting point of tin at 210°C for 48 hours to allow a small fraction of the tin to diffuse into the copper and form a bronze, a tin diffusion step at 340°C for 48 hours to form a tin rich bronze so that the niobium rods have sufficient concentration, and a Nb_3Sn formation step at 670°C for 70 hours for stoichiometric, A15 Nb_3Sn to form. This heat treatment schedule was chosen to maximise current density to test stress management

at the highest possible flux density. The conductor should produce 2800 A/mm^2 (12 T, 4.2 K) and a RRR of 30 with this heat treatment.

4.4 Vacuum Pressure Impregnation

After the Nb_3Sn heat treatment, robust NbTi leaders are spliced onto the brittle Nb_3Sn leads for protection against strain degradation in the leads. Then all voltage taps, capacitive strain gauges, and electrical instrumentation that would not survive the heat treatment are installed along with quench detection and protection circuitry. After the quench circuitry is installed, the magnet is welded closed and sealed for Vacuum Pressure Impregnation or VPI with CTD-101k® [73]. As previously discussed VPI minimizes the inter-wire point contact force and fills voids to reduce conductor movement from Lorentz force and increases resistivity between contacts.

Figure 51: Epoxy Filling Cups and VPI Vessel with Viewports

VPI is accomplished by first degasing the epoxy at a temperature that balances the epoxy pot life and minimizes the viscosity (100 μTorr, 60°C, 80 cP, 10 hours) [73]. Simultaneously the magnet is placed in low vacuum (250 μTorr) in the VPI vessel in

Figure 51 to minimize the formation of void space and trapped air inside the magnet. Then atmospheric pressure is opened to the degassed epoxy and differential pressure enables epoxy to flow into the magnet. The magnet is fully impregnated once each overflow cup has collected epoxy as shown in Figure 52. The epoxy is then cured at 110°C for 5 hours and 125°C for 16 hours. The cured epoxy also increases the resistance between the coil and the surrounding support structure [74]. Figure 53 shows a picture of both coils after VPI.

Figure 52: Cured Epoxy in Filling Cups

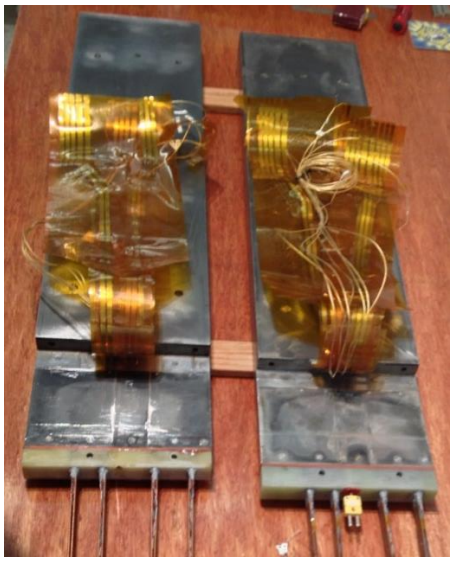

Figure 53: Fully Impregnated TAMU3b and TAMU3c Coils

4.5 Flux Return Installation and Instrumentation

After the coil is fully impregnated and cured it is ready to be installed into the flux return. There are three primary steps to the installation process. First, each coil needs to be electrically insulated with Kapton and G-10 sheets to prevent multiple current paths and protect each coil if there are multiple shorts from a catastrophic quench. The second step is to physically install and center the coils using Wood's metal filled bladders. The TAMU3 magnet will be vertically cold tested with the leads downward. This allows the magnet to be better protected against low levels of liquid helium and will allow more testing for the amount of liquid helium used. The final step is to electrically wire each coil to terminal strips and fabricate a wiring harness that is compatible with the electrical interface of LBNL's new test station.

4.5.1 Coil Insulation

The lowest resistance to ground is located in the TAMU3c coil at roughly 250 Ω. If a hard short (1-2 Ω) were to occur on one of the coils while testing we would still be able to

successfully complete the test as long as the shorted coil were isolated and allowed to electrically float relative to all of the other electronics. If each coil is insulated, then we are allowed a single hard short in each coil without creating a closed, alternate path for current to travel. Figure 54 shows the first layer of Kapton and the subsequent layer of G-10 insulation that electrically isolates the coil from the flux return.

Figure 54: Kapton and G-10 Insulated Coils

Each coil was electrically high-potential tested by placing each surface on a metal plate and connecting the surfaces to a high-voltage power supply. The test criterion was set to 500 volts with a 0.1 µA trip current. Each surface of TAMU3b and TAMU3c passed the high-potential test.

4.5.2 Flux Return Installation

The process of installing the coils using Wood's metal filled bladders requires four simple steps: warming the entire assembly, installing and centering the coils, pressurizing the bladders, and finally solidifying the Wood's metal. The Wood's metal bladder system is shown in Figure 55. The valve system on the left hand side of Figure 55 is shown schematically in Figure 56 and the Wood's metal bladder valve system shown on the right half of Figure 55 is shown schematically in Figure 57.

Figure 55: Wood's Metal Bladder System

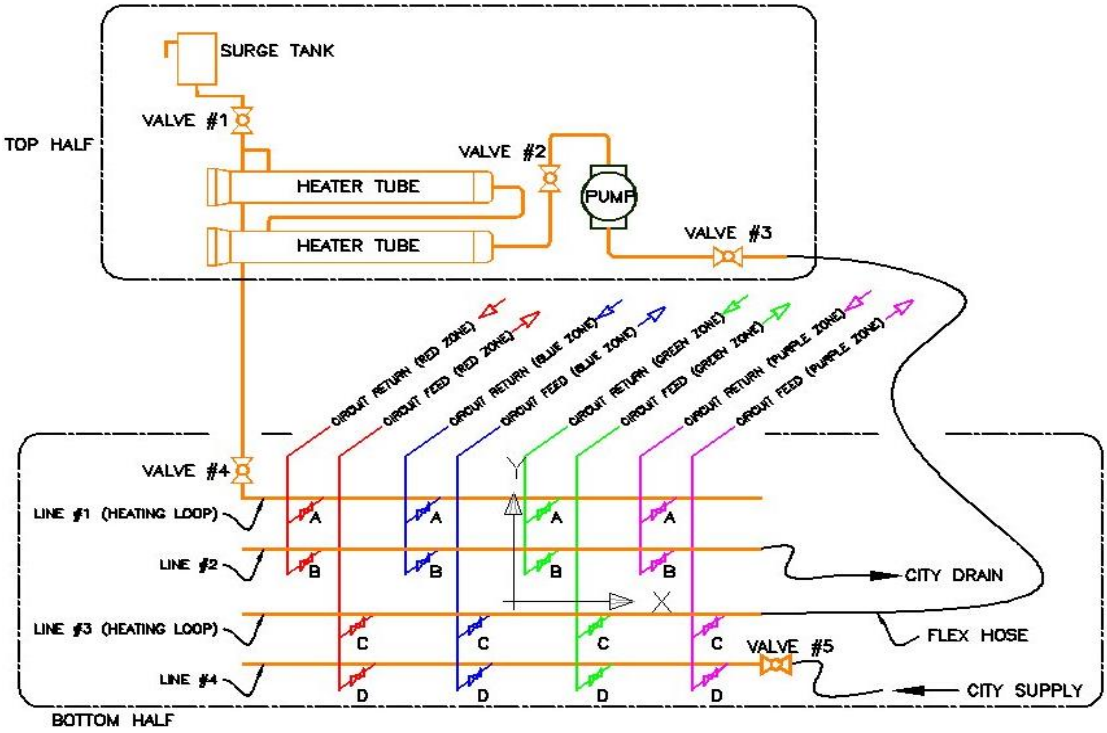

Figure 56: Flux Return Zone Valve Map

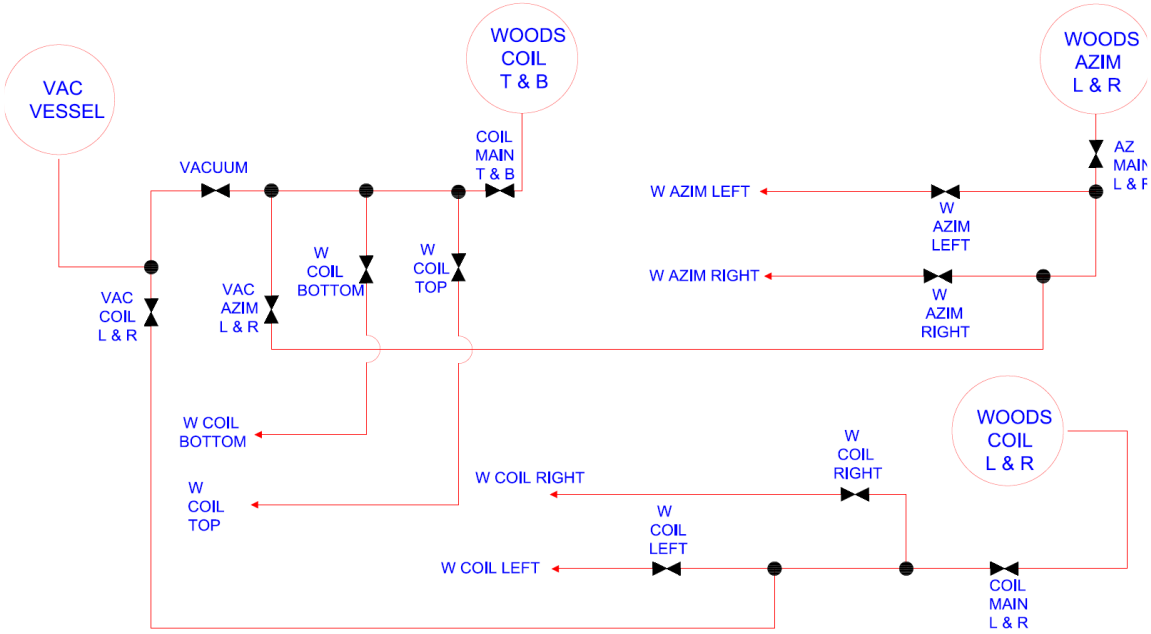

Figure 57: Wood's Metal Bladder Valve Map

First the coils are installed in the bore of the flux return. The installation ordering for each coil and piece of filler iron is designated in Figure 58. The bladders are made out 0.020" stainless steel sheets and are placed between the coils and the flux return. The coil is centered by using dial indicators as shown in Figure 59. Once the entire flux return and bladder system are above the melting point of Wood's metal the bladders are pressurized while keeping each coil centered in the flux return. Finally the system is slowly and sequentially cooled below the melting point of Wood's metal starting on the tail end of the coil and progressing through each of the four zones of the flux return. This procedure ensures that the preload on the magnet is uniform and independent of the phase change contraction of Wood's metal.

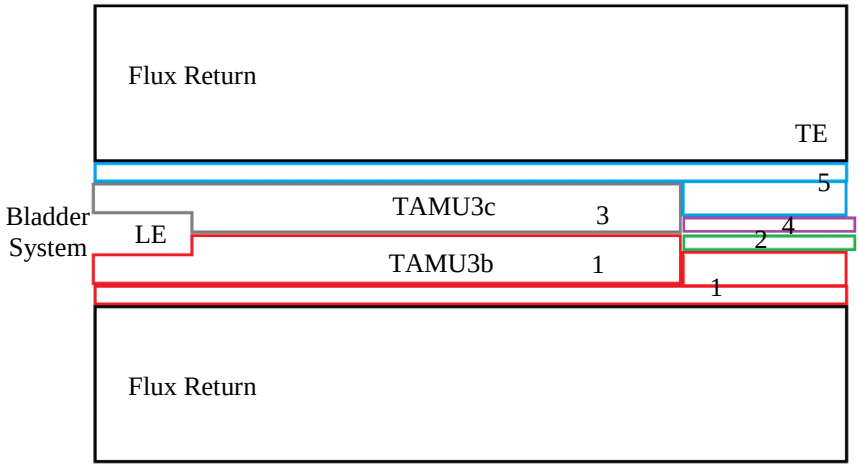

Figure 58: Installation Ordering into the Flux Return

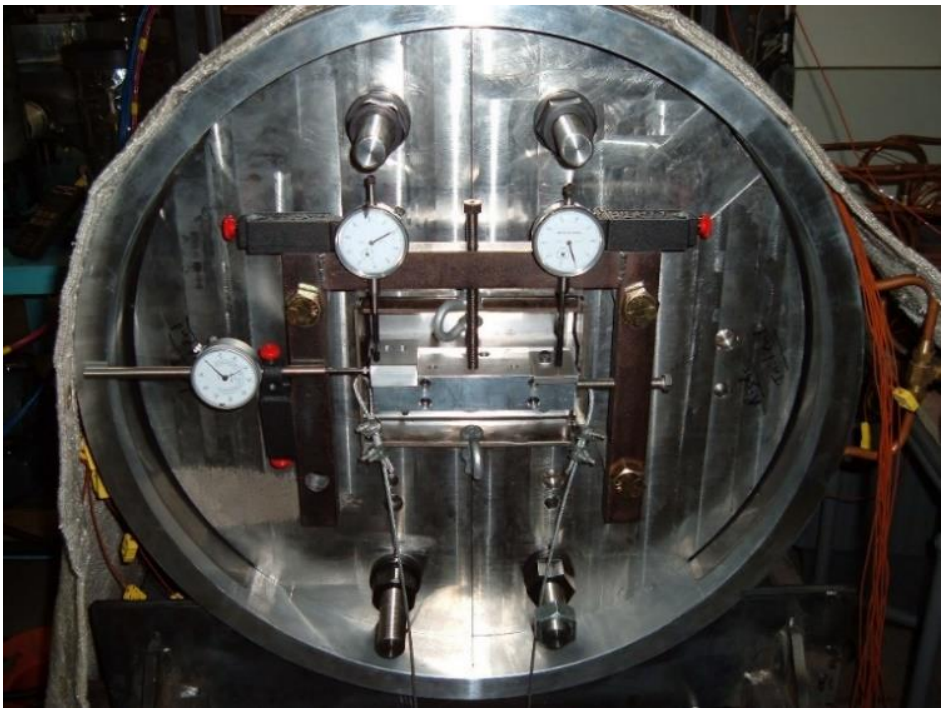

Figure 59: Dial Indicators to Center Coils

5. TAMU3 ANALYSIS

TAMU3 is a bi-modular Nb_3Sn single-pancake dipole designed to become the background field for a full bore dipole. The developmental conductor used should produce the highest current densities possible with low temperature superconductors in the 12 to 15 tesla range. However, during heat treatment elemental tin leaked out of the conductor and differential expansion between support materials and the conductor could potentially reduce the current carrying capacity of the conductor. Cable resistivity and bulk resistance to ground are within the expected ranges in comparison to simular superconducting magnets. Transducer and strain gauge calibration results enable excellent and reliable data from magnet testing to be collected and analysed. Cable and magnetic field orientation will minimize the AC losses for TAMU3 in comparison to other comparable coils.

5.1 Cable Expansion

Gaps were found in TAMU2 stress management structure after heat treatment. It was determined that TAMU2 gaps were caused by the relaxing of internal stress in the stress management structure during the heat treatment. This was corrected in TAMU3 by pre-annealing all components prior to tooling and heat treatment.

It is a generally accepted phenomena that internal tin Rutherford cable contracts in length (~0.0005 m / 1 m) and expands in cross section during the heat treatment [75]. The heat treatment of TAMU3a and TAMU3b resulted in a gap of roughly 0.41 mm forming in the end regions between the stress management spring and the first turn of the outer winding. This is the opposite of conventional thought with internal tin conductor. Incorporating the potential strain on the conductor from the support structure, the calculated gap should be between 0.22 mm (from material properties) and 0.79 mm (from empirical cable data.)

5.1.1 Magnet and Material Properties

Figure 60 shows the location of a gap between the curved middle pier and the first turn of the outer coil of TAMU3b. For the TAMU series magnets Grade 5 titanium was chosen as the central mandrel for its small thermal expansion and Inconel 718 was chosen for the stress management structure for its high strength. Table 7 shows the integrated thermal expansion coefficients for various materials and internal tin conductors.

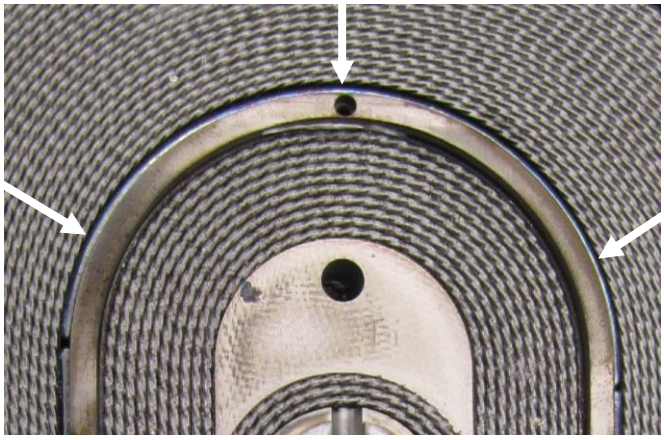

Figure 60: Tail End Gap in TAMU3b

Table 7: Integrated Thermal Expansion Coefficients for Conductor and Materials

Material (mm/m)	STP	670°C	STP	To 4.2 K	STP
Internal Tin Simulation [76]	0	2.8	-3.6	-6.3	-3.1
Internal Tin Rutherford Cable, 19 subelement [75]	0		-2.8		
Internal Tin Strand, 19 subelement MJR [77]	0	1.4	-7.0		
OST RRP 84/91 twisted strand [78]	0	5.7	-0.2		
OST RRP 54/61 twisted strand [61]	0		+0.3		
OST RRP 108/127 twisted strand [61]	0		-0.45		
OST RRP 108/127 untwisted strand [61]	0		-1.2		
Inconel 718 [79, 80]	0	9.91	0	-2.389	
Inconel X-750 [72]	0	9.9	0	-2.4	
Titanium [81]	0	6.9	0	-1.5	
A36 Steel [82]	0	8.5	0	-2.02	
Copper	0	12.4	0	-3.26	
Niobium	0	4.6	0	-1.43	
Nb_3Sn [83]	0	5.5	0	-1.8	

5.1.2 Gap Calculation

The length of the middle pier and inner beams is 55 cm and made out of Inconel alloy 718. This structure should expand 5.5 mm during the 670 °C soak from Table 7 data. The cable undergoes stress relief, phase change, and thermal expansion simultaneously and isn't nearly as straight forward to calculate [84]. From simulation [76] and from a slightly higher filament count high-tin content OST RRP® conductor [78] the best estimate for expansion of the outer conductor is 2.8 mm or about half as much as the middle pier. This implies that the cable is in tension during the Nb_3Sn formation heat treatment. The outer coil cable tension during A15 formation inhibits the conductor from freely contracting during heat treatment cool down.

To calculate the total strain on the conductor at each step of the heat treatment we need to balance the stress equation below using the given stress-free expansion parameters of Table 7 and the moduli, cross section, and length from Table 8.

$$\sum_i A_i E_i \varepsilon_i = 0 \tag{7}$$

In the static or equilibrium force Equation (3), the strain is calculated from the deviation from the stress-free position of each material or the strain. A_i is the area, E_i is the material modulus, and ε_i is the strain. The point of contact is between the compressed spring and the outer coil. Solving this equation by taking into account the coffin, the coil, the spring, and the stress management structure, the equilibrium length is 55.81 cm at 670°C where the Inconel is compressed by 0.66 mm, the cable is in tension by 1.45 mm and the steel support structure is compressed by 0.08 mm.

Table 8: Young's Modulus and TAMU3 Cross Sections

Material (GPa)	4 K	STP	670°C	Cross Section	Length (inner / outer)
Niobium [68]	109.6	105.0	94.4	81.3 mm^2	55.33 cm
Nb_3Sn [76]	100.0	135.0	135.0	99.4 mm^2	55.33 cm
Copper [68]	137.0	128.1	90.7	150.3 mm^2	55.33 cm
Inconel 718 [79]	216.5	199.9	162.0	252.9 mm^2 / 306.5 mm^2	55.33 cm / 62.92 cm
Steel Coffin [85]	212	200.0	124.1	380 cm^2	99.1 cm

During the cool down, the stress equation is balanced with the only nuance being that Nb_3Sn was formed in the stretched cable state. After the horizontal coffin pressure is released from the axial Inconel bolts, the coil is free to move to its stress free length and the coffin contribution to Equation (3) is removed. The final cable dimension is 55.39 cm or 0.64 mm larger than the middle pier. Now both curved springs are relaxed and will each expand about 0.10 mm so that the total measured gap will be roughly 0.44 mm. Therefore based on the new Nb_3Sn equilibrium length, the cable moduli, and the spring compression the calculated gap between the tail end curved middle pier springs and the outer coil is 0.22 mm. At the tail end apex of TAMU3b a 0.41 mm gap was measured with all other stress managing structure and cable in intimate contact as designed or about double the calculated amount.

We can also estimate the final cable dimension based on heat treated cable measurements rather than cable constituents. According to Dietderich et al. [77] simular conductor contracted 8 mm / m from reaction to room temperature and McRae et al. [78] reports 5.7 mm / m respectively. Using these numbers as a range we get that the final gap between the outer coil and middle pier should be between 0.14 mm and 0.79 mm. The result from McRae et al. is with conductor (84/91 RRP®) that is very similar to our conductor (54/61 RRP®.)

5.1.3 TAMU3c Solution

This problem was remedied in TAMU3c by adding a 1.0 mm sliding expansion joint in the pier and beam structure as shown in Figure 61. The new sliding joint enabled the continued use of high strength Inconel 718 and was accomplished without loss of stress management strength for long length magnets.

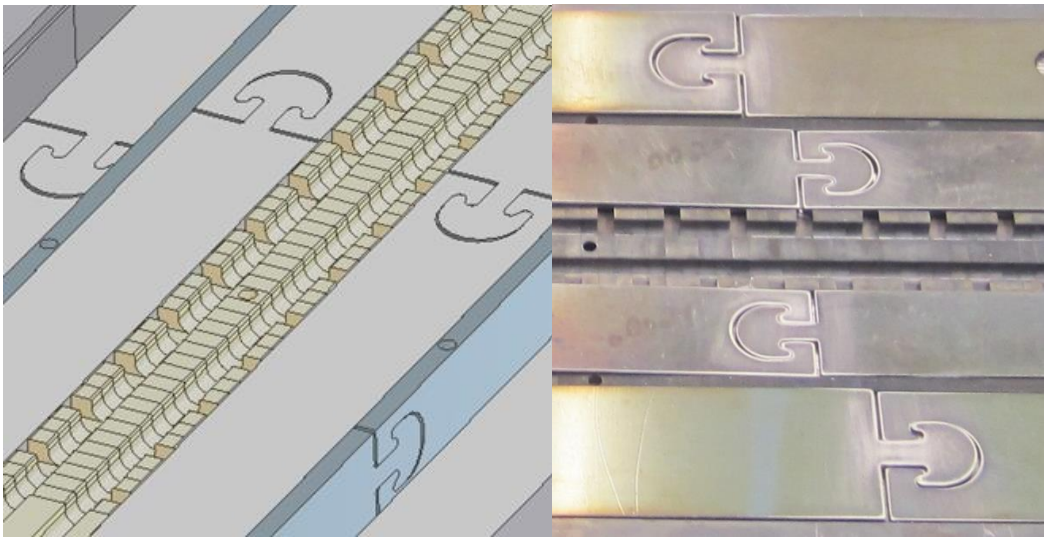

Figure 61: Thermal Expansion Sliding Joints

5.2 TAMU3a Post Heat Treatment Analysis

Opening the retort coffin after heat treating TAMU3a revealed several deposits of tin that leaked out of the conductor. There was also a large deposit of a black coating over the lead end of the titanium central mandrel. A journey then commenced to determine the cause, the extent of damage, and the viability of the coil without invasive or destructive testing. Several of the methods developed in this process have the potential to aid in magnet characterization and quality control with the ability to predict magnet failure before cold testing. The likely causes of tin leakage was determined to be an omitted 210°C solid diffusion stabilization soak during the heat treatment. Other contributions to the leaked tin include the possibility of over strained conductor or damaged barriers from the cabling and subsequent anneal cycles.

5.2.1 Preliminary Tests

The first test was to verify the elemental makeup of the leaked metal. The leaked metal was initially thought to be aluminium from a temporary non-heat treatment tooling piece unknowingly left in place. The metal melted on a hot plate set to 350°C and

aluminium melts at 660°C. Figure 62 shows the extent of tin that leaked along the leads and eroded or etched much of the stabilizing copper.

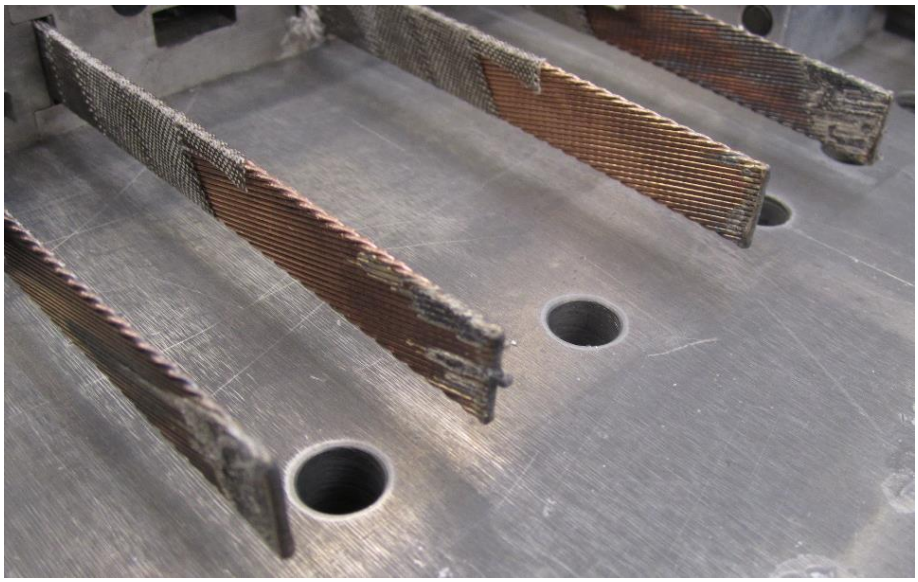

Figure 62: Exposed TAMU3a Leads

The metal was then taken to the Texas A&M Microscopy and Imaging Center for EDS or Energy Dispersive Spectroscopy to determine the elemental makeup of a collected sample. EDS revealed the sample was elemental tin with small amounts of copper and carbon varying between 0 and 3 weight percent. The black coating was also analysed and was determined to be predominately carbon but the source was undetermined. Both tin and carbon samples were removed from the tooling shown in Figure 63.

Figure 63: Location of Leaked Tin and Carbon Soot

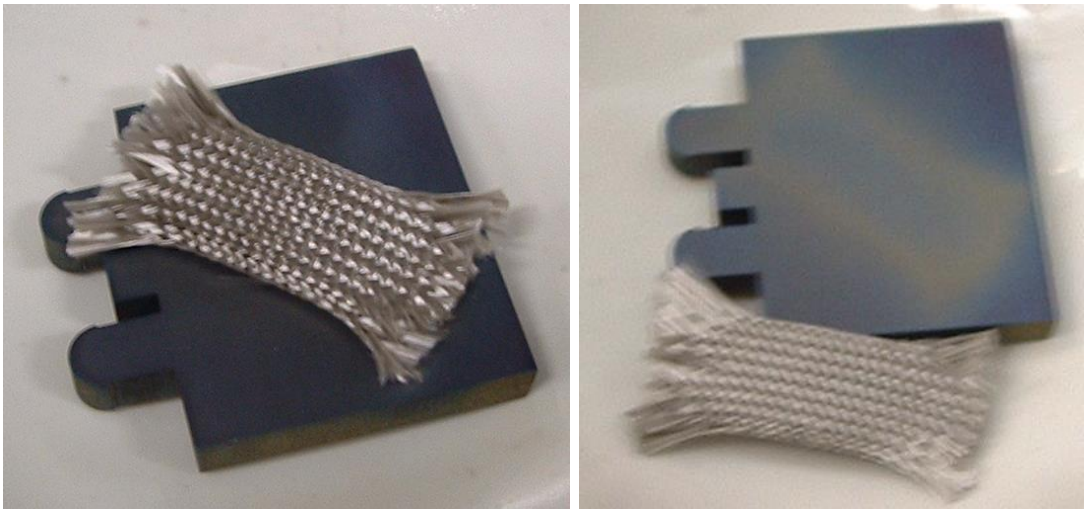

Figure 64: S-Glass and Titanium Bake-Out Test

The next series of tests was to determine if any of the cable processing chemicals could cause the black carbon. Direct EDS of the fine filament S-Glass insulation was inconclusive because the quartz material dominated the spectrum. Inert bake out tests with the S-Glass in contact with titanium revealed a discoloration oxide layer but no carbon

residue as shown in Figure 64. This ruled out that silane or palmitic acid from the cabling and insulation process caused the carbon soot on the titanium central mandrel.

Since EDS was not sensitive enough to determine the relative quantity of carbon on the surface of the S-Glass it was decided to use Secondary Ion Mass Spectrometry or SIMS on the surface through the Center for Chemical Characterization and Analysis in the Department of Chemistry at Texas A&M University [86]. The samples were prepared by placing raw and baked S-Glass samples on a meniscus of silver paste on a silver foil. The intensities of C, AlO and SiOH were normalized by the intensity of Si as shown in Table 9. The data obtained is for 3 different surface spots where each spot has different number of wires. To avoid surface charging via ion bombardment, the surface was sputter coated by a ~5 nm Pd layer.

The results indicate that the darker discoloration on baked S-Glass samples was not carbon based. The baked samples had less carbon than the raw samples. In conclusion the discoloration is not carbon based and is likely due to the silane sizing.

Table 9: SIMS of Raw and Baked S-Glass Braded Insulation

	C / ^{30}Si	AlO / ^{30}Si	SiOH / ^{30}Si
Raw glass site 1	0.05	0.5	2.3
Raw glass site 2	0.09	0.4	2.2
Raw glass site 3	0.14	0.5	2.4
Baked glass site 4	0.04	0.35	1.8
Baked glass site 5	0.03	0.5	2.2
Baked glass site 6	0.03	0.55	2.5

5.2.2 Weld Analysis

The majority of the tin leaked out of the end of the cable near the ends. The cable is TIG welded to inhibit tin from leaking. There was a small fraction of tin that leaked in the body of the coil where an arc damaged a small segment of conductor near the tail end

while welding the leads. A picture of the arc after heat treatment and the new grounding device codenamed Mother of All Grounds is shown in Figure 65. This welding method is the most common practice for sealing Rutherford cable for Nb_3Sn internal tin conductor.

Figure 65: Weld Arc and MOAG

Images of TAMU3a welds were compared with images of welds on other reacted and unreacted cables of Nb_3Sn to determine the failure mechanism. Samples were prepared by curing them in an epoxy resin and polishing them with varying grit sizes, ending with .03 micron slurry. In 10-stack weld images shown in Figure 70, little to no cracking or splitting in the bundles were found. The 10-stacks were previously prepared and heat-treated by a sequence that included the first dwell-time.

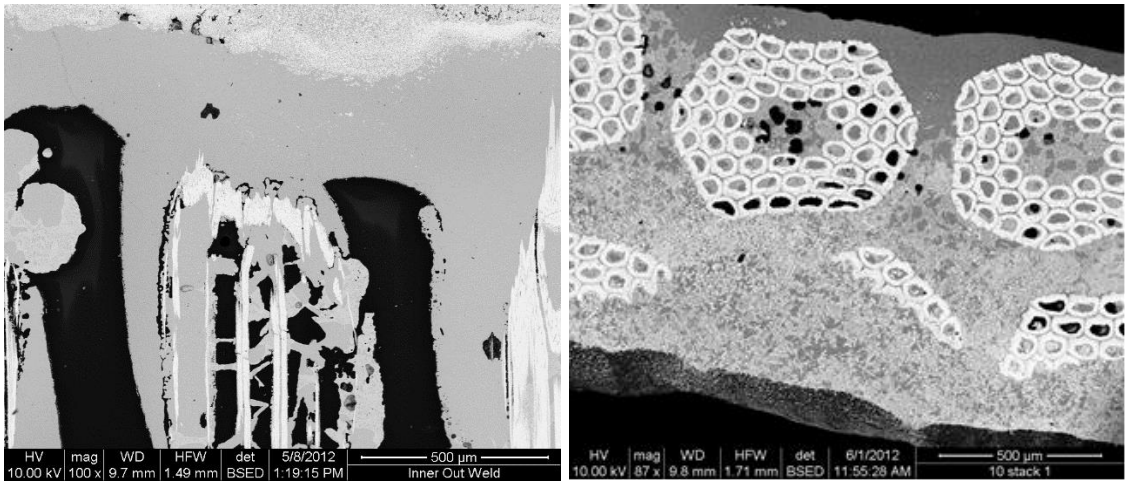

Figure 66: 10-Stack Welds in Longitudinal and Transverse Cross Section

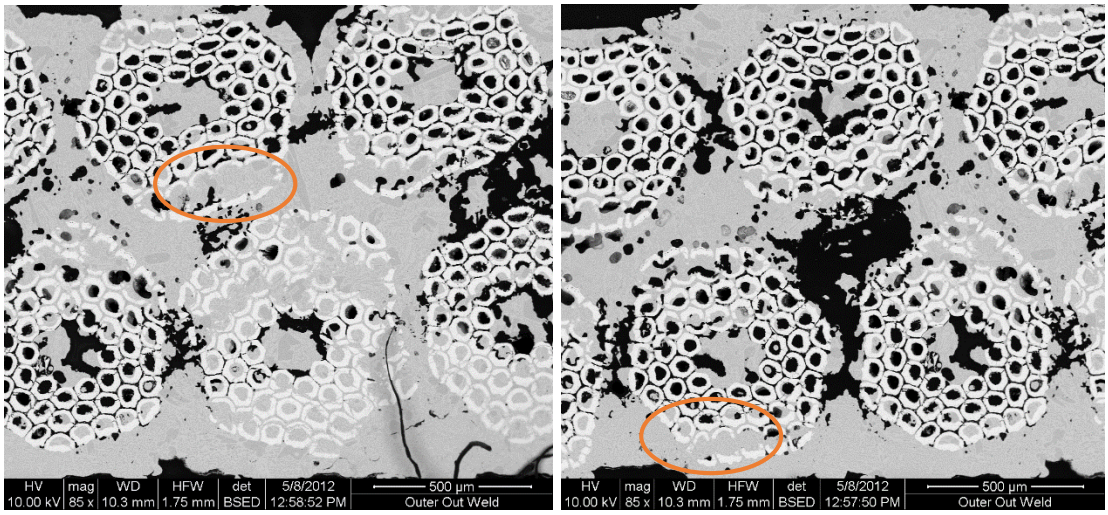

Figure 67: Transverse TAMU3a SEM Weld Images

In Figure 67 there is clear evidence of high pressure molten tin causing the bundles to burst. Two of the locations of burst bundles are indicated. The standing head pressure based on the density of tin and the length of the coil is roughly 0.2 MPa. Tin expands roughly 2% when melting and would cause over 1000 MPa of pressure based on the geometry and strength of materials if no tin has time to diffuse into the copper and decrease

the volume before the phase transformation. In conclusion it stands to reason that the omitted 210°C solid diffusion soak was the primary cause of leaked tin at the welds. The welds are indeed the weakest point for tin pressure but should be adequate when the entire heat treatment is employed.

5.2.3 Cable Resistivity Measurements

For the resistance measurements one amp of current was placed in each coil as determined by a 10 watt, one Ω resistor and voltages were measured at each voltage tap and turn on the lead (LE) and tail ends (TE) as mapped in Figure 68. For Figure 69, resistance per length was calculated from the voltage difference between two adjacent measurements and divided by the current and the length between measurements.

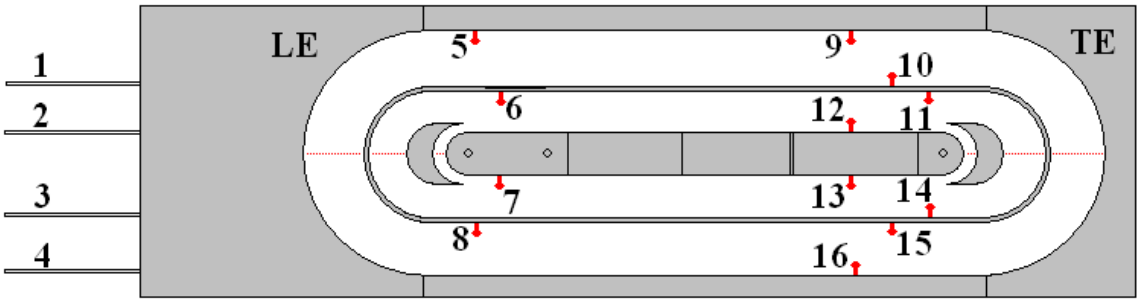

Figure 68: TAMU3 Voltage Tap Map

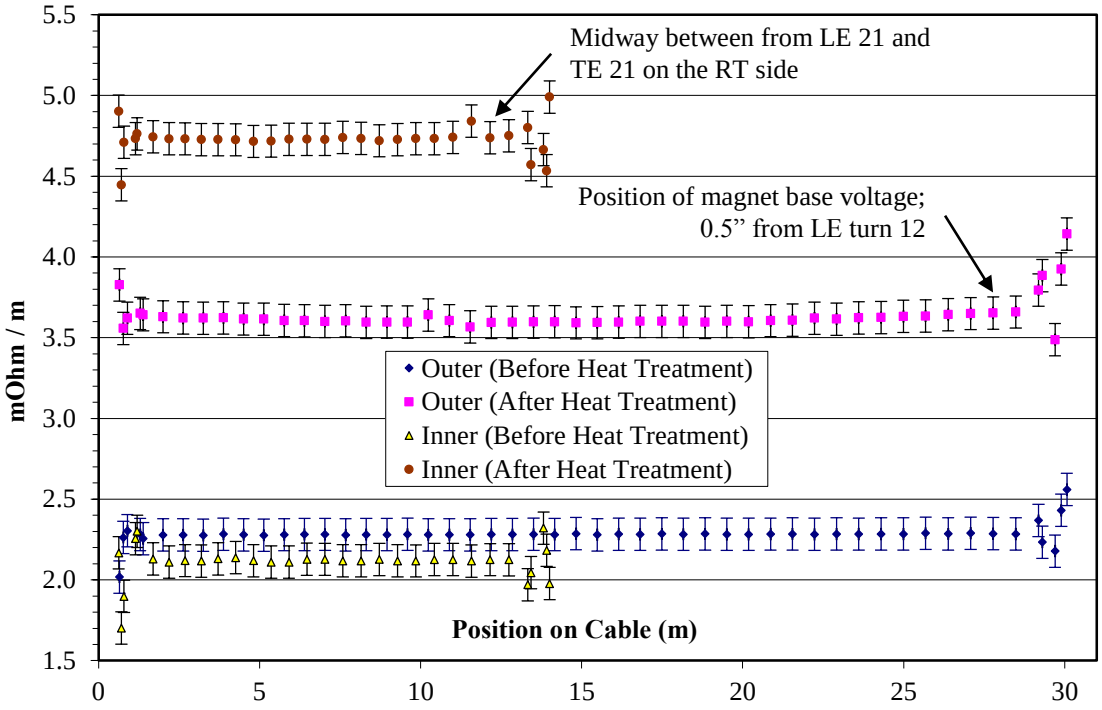

Figure 69: TAMU3a Coil Resistance per Length

In Figure 69, the systematic errors originate from the current gradually shifting due to the one Ω resistor and power supply gradually shifting during measurement. The voltage taps are relatively close to each other and voltage measurement errors were magnified in the voltage tap regions near the first and last turns.

The voltage measured on the exit leads with respect to the entrance lead before (after) heat treatment was 31.41mV (69.89mV) for the inner and 71.72mV (112.83mV) for the outer. After heat treatment the voltage measured on the central pier, the middle pier, the outer pier, the magnet base and the base caps all measured 100.5mV for the outer and 61.7mV for the inner. This corresponds to positions on the cable as indicated on the Figure 69 that have the smallest resistance to ground. The cable resistance remains uniform in the same region and indicates that there was not a large loss of tin that would cause an increase in resistance per length and decrease in resistance to ground.

Table 10: Summary of Coil Resistance per Length

(mΩ / m)	Inner		Outer	
	Before HT	After HT	Before HT	After HT
Average	2.11	4.73	2.28	3.64
Standard deviation	0.11	0.09	0.06	0.10
Percent difference	76.6%		45.8%	
Ratio	2.24		1.59	

Other magnet fabrication groups do not traditionally publish cable room temperature resistance; only the RRR value is published. From a personal communication with Alfred McInturff from the Accelerator Research Laboratory at Texas A&M, it was determined that the resistance of the cable as given in Table 10 is well within the acceptable ranges for before and after heat treatment.

There are also substantial variations in the resistance per length near the ends of the cable. The variations extend roughly a full turn from each lead. There are two suspected causes for the resistance variation. One obvious explanation would be the tin leakage from the leads. Preferential volumetric expansion near the ends of welded cable/wire samples would also explain the large variation [61].

5.2.4 Wire Saw Lead Cutting

After measuring the resistance per length of the coil it was determined to calculate what the theoretical values should be and to determine the amount of tin that wicked in the middle of the Rutherford cable. Samples were cut with a specially developed wire saw. The wire is 0.3 mm in diameter and impregnated with diamond shards to abrasively cut one inch off of the leads. Rather than a continuous one direction motion that is typical for abrasive cutting, the wire was manually reciprocated for fine control of wire speed and to minimize the disruption to the remainder of the Nb_3Sn superconducting cable. In Figure 70 the motion and function of the saw is demonstrated and in Figure 71 the resulting first cut lead segments are displayed.

Figure 70: Rutherford Cable Wire Saw Assembly

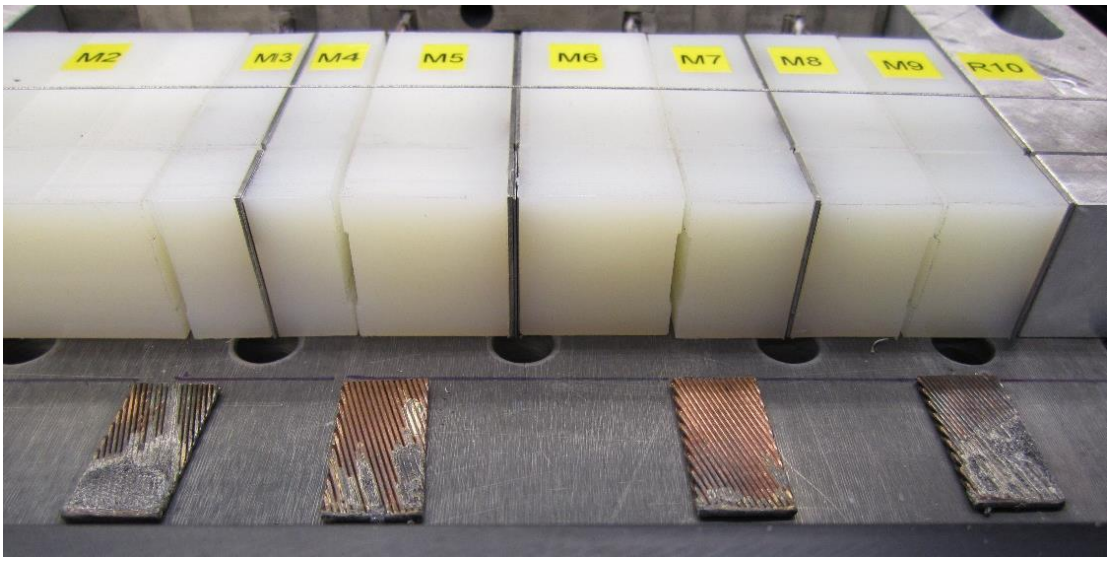

Figure 71: First Cut Inch of Rutherford Cable

5.2.5 Optical Images of Cut Leads

To better determine the extent of tin damage to the leads optical images of the first and second cut inch of each lead were taken. A single image of each strand was taken with an Amscope® binocular biological microscope with a 1.3 MP camera attachment. All images were collected at 150x magnification. The images were pieced together and are presented in Figure 72. The images starting from left to right are of the first and second inch of inner conductor and the first and second inch of outer conductor. The first cut inch was lightly etched and removed the bright luster that is visible in the unetched images of the second inch.

For the inner conductor very little tin is visible between the strands of the Rutherford cable both at the one and two inch mark. In total the splice joint is designed to be 4 inches long. The end of the outer cable was completely poisoned with tin and after one inch 25 of 34 strands were poisoned. For the second inch 13 of 34 strands were poisoned. This left two inches to make the splice joint which is typically the minimum length necessary to make a reputable ~nΩ joint. In conclusion, there are sufficient number of clean strands and sufficient length to make a successful joint. However, the ability to introduce current into the compromised strands needed to be verified.

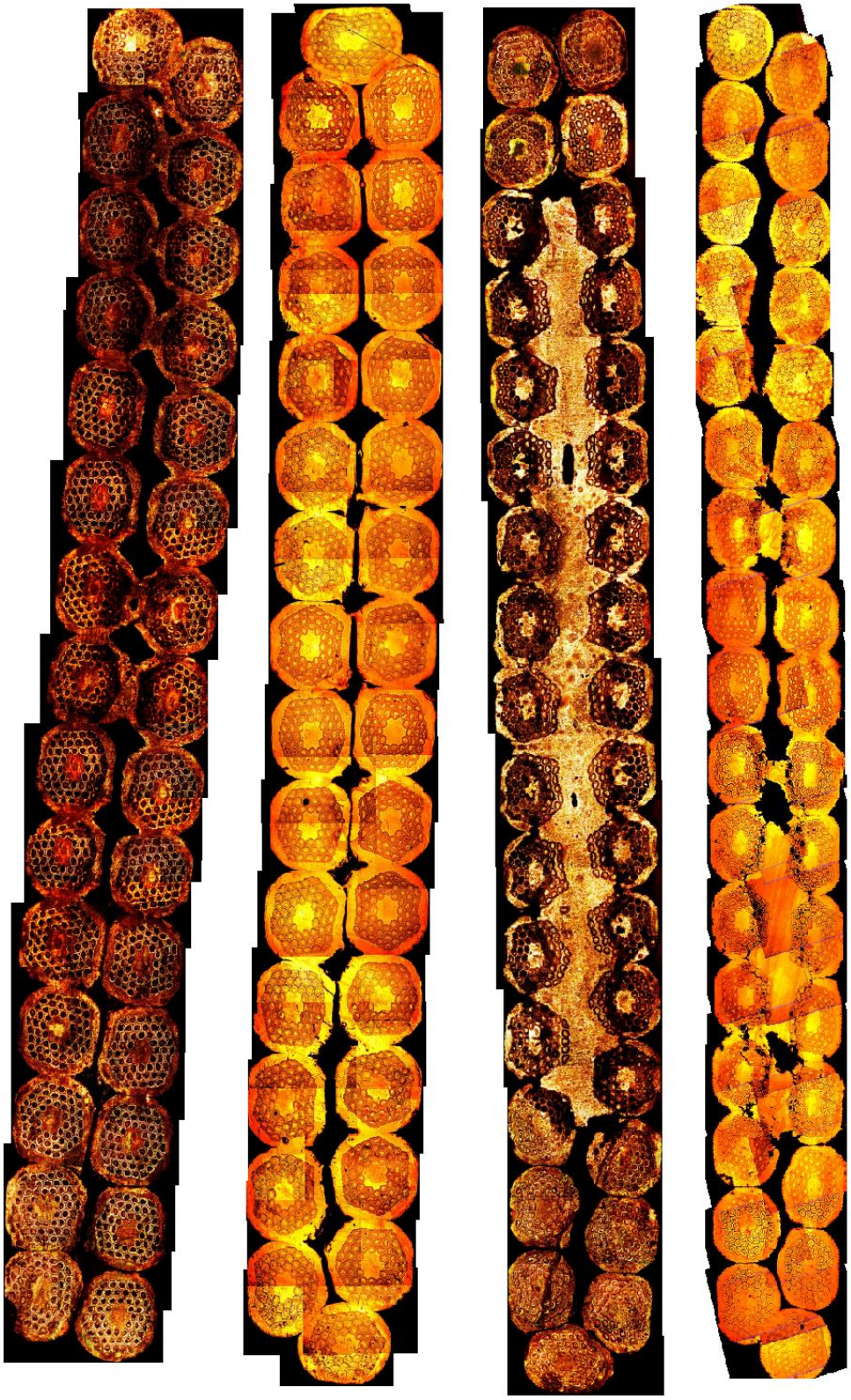

Figure 72: Optical Images of TAMU3a Cut Leads

5.2.6 SEM Imaging and ImageJ® Analysis

After optically imaging the cut leads it was determined that Scanning Electron Microscope (SEM) analysis should proceed to determine the extent of A15 present, the extent of copper poisoning and each component cross section. For this process both reacted samples from the wire saw and unreacted cross sections were polished and analysed. The outer precursor SEM samples were polished to 0.02 microns and etched in 50% solution of HNO_3 by swab for 8 seconds. The etching removed all elemental tin in the core of each bundle for the unreacted. The inner samples were polished to 0.02 microns and then etched in a solution of 13% HF + 37% HNO_3 by swab for 10 seconds. Theoretical cable resistances were calculated from cross sections calculated with ImageJ® [87]. A great debt is owed to K. Damborsky for his kind tutelage with SEM analysis and ImageJ®.

5.2.6.1 Unreacted Outer Conductor

The Outer conductor is 34 strands at 0.7 mm diameter. The conductor was initially annealed at 200°C for 4 hours and then cabled and rolled for a compaction of roughly 11%. Braiding S-Glass insulation deregistered the Rutherford cable so the cable was re-annealed and rerolled to a total of 13.5% compression. S-Glass insulation was then successfully braided onto the cable. This pre-anneal allowed various phases of bronze as seen in the above Back-Scattered Electron (BSE) image in Figure 73 and Energy Dispersion Spectroscopy (EDS) analysis presented in Table 11.

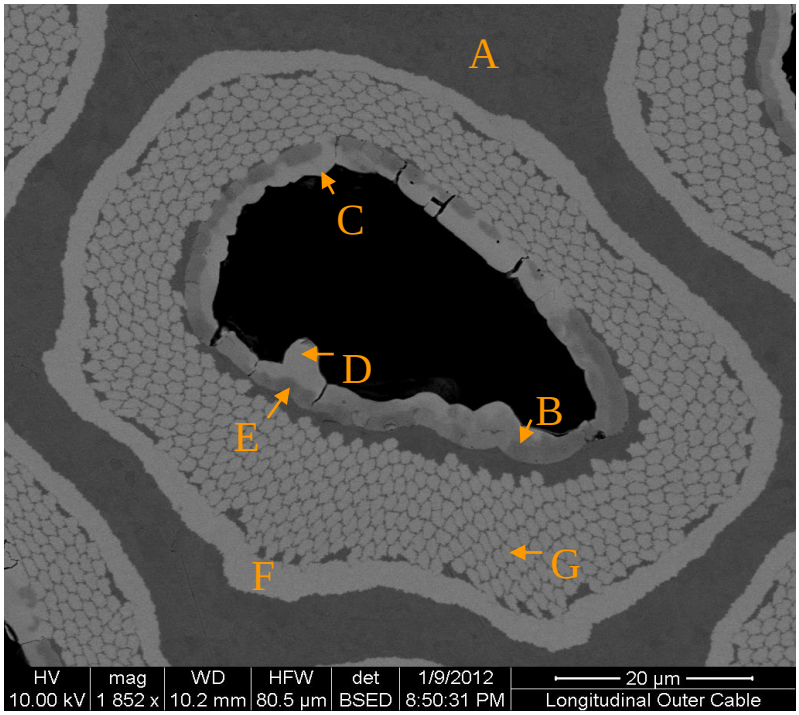

Figure 73: BSE Image of TAMU3 Unreacted Outer Conductor

Table 11: Atomic % EDS Analysis of Unreacted Outer Conductor

Location	Nb	Sn	Cu	Ta	O_2	N	C
A			97.48				2.52
B		22.5	19.4		48.1	1.2	8.9
C		32.5	0.0		53.8		13.7
D		30.7	39.7		23.6		6.0
E		29.5	34.0		29.8		6.8
F	96.2			3.8			
G	84.5			3.0	12.5		

Table 12: ImageJ® Cross Sections and Resistivities of Unreacted Cable Materials

Material	Area (mm^2)	Percent	ρ (Ω-m)
Nb	0.100	27.4	1.33E-07
Sn	0.037	10.0	1.01E-07
Bronze HIGH	0.020	5.5	1.80E-07
Bronze LOW			9.50E-08
Internal Copper	0.027	7.4	1.58E-08
Stabilizing Copper	0.184	49.8	1.58E-08

Table 13: Unreacted Outer Cable Resistance per Length Calculated and Measured

Calculation	Ω / m
Cable HIGH	0.00201
Cable LOW	0.00200
Measured	0.00228

Using ImageJ® from the NIH [87] the percentages of each element in the unreacted cable was calculated as well as the total cross sectional area. The resistances are at room temperature and a range of resistance was given for different alloys of bronze. The calculated resistance per unit length for an individual strand and then for the entire cable is calculated from data in Table 12 and tabulated in Table 13. The measured resistance per length from electrical data is also included. The percent difference is relatively small at 13% between the calculated and measured resistance per length. This verified that our method of calculation was accurate enough to detect unexpected resistance differences greater than 20%.

5.2.6.2 Reacted Outer Conductor

The following SEM images in Figure 74 and Figure 75 are taken at the same location on the first cut inch of reacted TAMU3a outer conductor. Notice in Figure 74 that there no longer remains any differentiation between strands of the Rutherford cable. The topology of the image is an artifact of the etching process. The Back-Scattered Electron (BSE) image in Figure 75 shows how the middle material is from various phases of bronze. The lighter colors are more tin rich bronzes while the darker areas between the strands are tin poor.

The SEM sample shown in Figure 76 was polished to 0.2 microns with no etch. The same sample was analysed with EDS to determine the elemental makeup at certain locations and the results are presented in Table 14. The cross sections of the image was analysed with ImageJ® and the results are presented in Table 15.

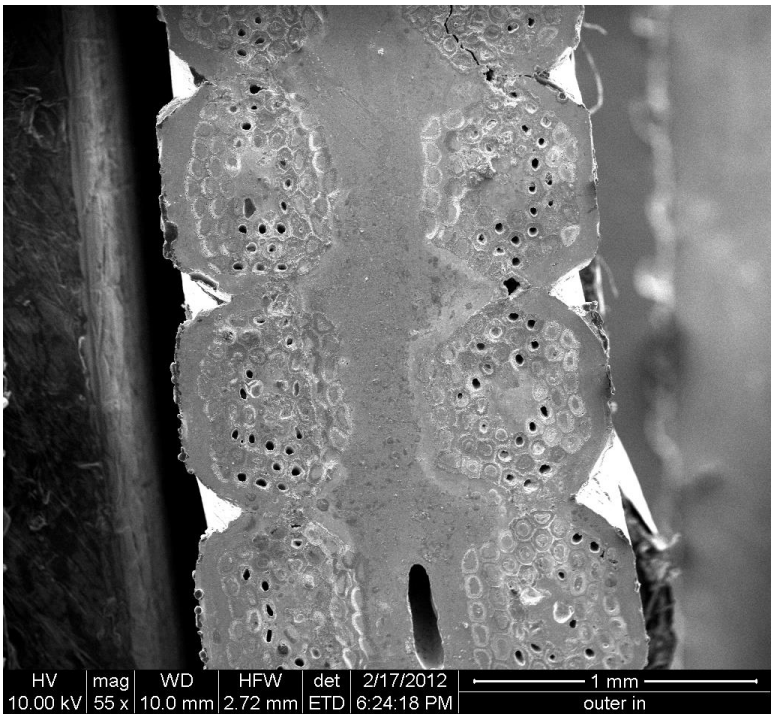

Figure 74: SE SEM Image of the First Cut Inch of Outer Conductor

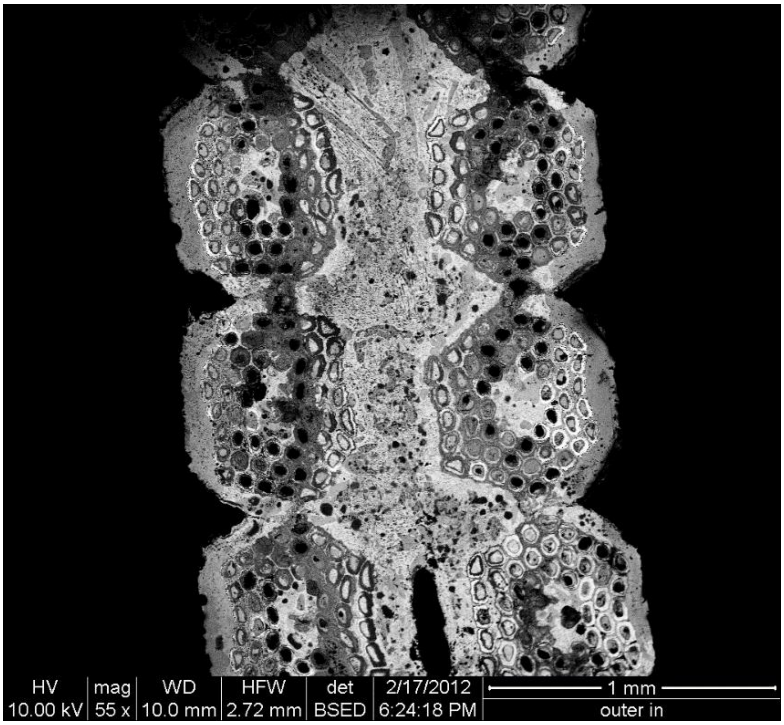

Figure 75: BSE SEM Image of the First Cut Inch of Outer Conductor

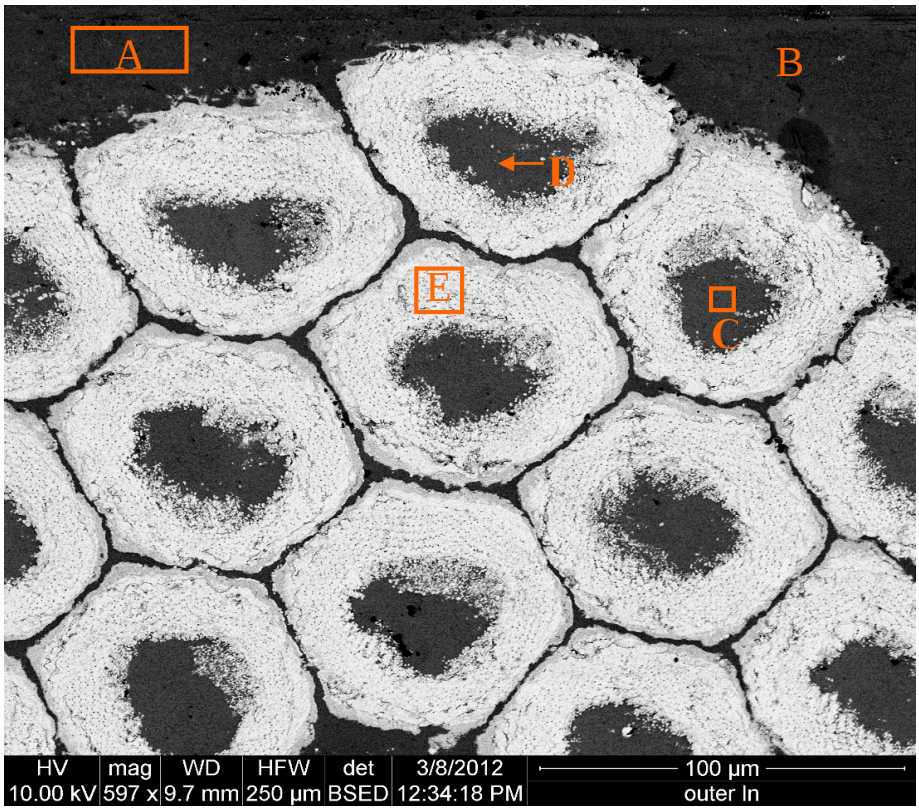

Figure 76: BSE Image of Pristine TAMU3 Reacted Outer Conductor

Table 14: Atomic % EDS Analysis of Reacted Outer Conductor

Location	Nb	Sn	Cu	Ta	O_2	Si	C	Al
A			76.3		6.0		14.3	3.4
B			69.5		13.1	1.3	16.0	
C		3.9	88.3		7.9			
D		2.7	77.2		4.5		15.5	
E	54.3	16.4	4.5	2.9	21.9			

During heat treatment the niobium, tin, and copper matrix becomes Nb_3Sn and bronze and thus the room temperature resistance increases. The calculated and measured resistance per length is presented in Table 16. The large range for the calculated resistance is due to the large composition range of the A15 Nb_3Sn with wide ranging resistivity [38].

Table 15: ImageJ® Cross Sections and Resistances of Reacted Cable Materials

Material	Area (mm^2)	Percent	ρ (Ω-m)
A15 High	0.137	32.3	8.00E-07
A15 Low			1.00E-07
Barriers	0.065	15.2	1.33E-07
Internal Cu	0.040	9.4	1.80E-07
Stabilizing Cu	0.183	43.0	1.58E-08

Table 16: Reacted Outer Cable Resistance per Length Calculated and Measured

Calculation	mΩ / m
Cable High	2.48
Cable Low	2.26
Measured	3.64

The uncertainty in the measurements is 0.10 mΩ / m and the uncertainty in the calculation is 0.22 mΩ / m from the given range above plus 15% of the measurement as determined by the unreacted analysis. The difference between the measured and the calculated quantities is nearly 2 standard deviations apart. This result is somewhat disconcerting and an indication that a large portion of the stabilizing conductor was possibly poisoned with tin and in a uniform fashion. The coil RRR will be the best indicator for stabilizing copper purity and will be measured during magnet cool down.

5.2.6.3 Unreacted and Reacted Inner Conductor

The inner conductor is 30 strands at 0.8 mm diameter. The strands were first annealed at 200°C for 4 hours and then cabled and rolled for a first pass compaction of 11.7%. S-Glass insulation was then successfully wound directly onto the cable. ImageJ® analysis was not performed on inner conductor for TAMU3a because the majority of the tin leaked out of the outer conductor. BSE images of TAMU3 inner conductor is shown in Figure 77 and Figure 78. The images of the unreacted cable in Figure 77 appears much cleaner than the reacted in Figure 78 even though the polish procedure is identical. The reacted A15 is much harder than all other materials and abrasively scratches the finish while polishing.

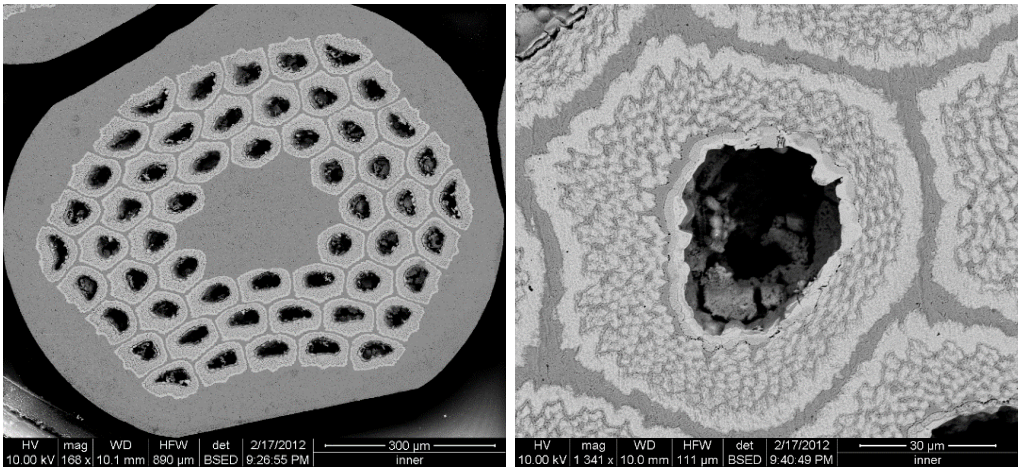

Figure 77: BSE SEM Images of Unreacted Inner Conductor

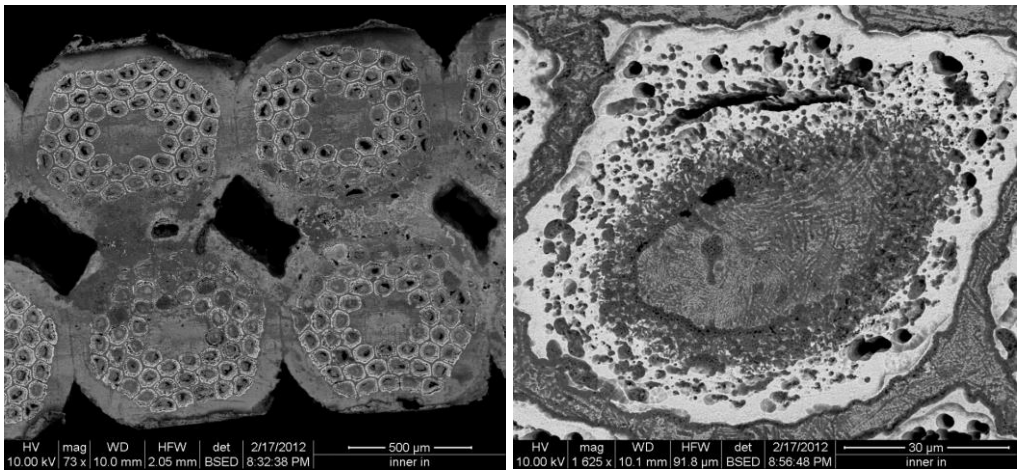

Figure 78: SEM Images of Reacted Inner Conductor

5.2.6.4 Conclusion

From heat treatment studies performed by Dietderich et al. [88] twenty years ago to the present [78, 89] and our imaging of unreacted and reacted cable we can safely say that the 210°C soak does not transform the entire tin core of an internal tin conductor. According to Mike Naus [90], it is much more likely that the solid diffusion soak fosters protective layers of ε and η phase bronze that encase the tin core and prevent bursts.

Therefore the omission of the 210°C soak prevented this protective layer to form and the tin burst forth through the weakest point at the welds.

From the reacted cable SEM images there are ample amounts of fine grain Nb_3Sn bundles that are sure to carry large current densities. The same images also reveal large poisoning of various bronze phases that will make current transfer into the superconductor at the leads difficult if not impossible. Therefore it was determined to perform short sample testing on the cut leads.

5.2.7 Short Sample Tests

From the first cut inch four samples were prepared for short sample testing. Sample preparation was made quite difficult because of short superconducting wire sample length (less than one inch) and strongly poisoned outer stabilizing copper. Each strand was already bonded to each other from the leaked tin forming bronze and made sample separation difficult to prevent damage to the brittle Nb_3Sn. Pictures of one of the samples is shown in Figure 79.

Figure 79: First Inch Short Sample Testing Setup

The amount of stabilizing copper on each strand was greatly compromised and inhibited any appreciable amount of current to be introduced into the superconductor in the short distance. For each sample the voltage of each joint and the voltage on the middle third of the superconductor was logged. The testing was carried out at the NHMFL in

Tallahassee, Florida in a liquid helium bath with a 0.2 μV / cm quench criterion. Of the four tested samples no transition was observed. The measured resistances from the I-V curve for each sample is presented in Table 17.

Table 17: First Inch Short Sample Resistances

Sample	Resistance (nΩ)
Inner in	62.6
Inner out	414
Outer in	856
Outer out	Broke lead

The expected joint resistance is between 1.5 and 6 μΩ as calculated by 0.020" thick stainless and similar thicknesses of solder across the joint including 5 tesla magnetoresistance at 4.2 kelvin. The test revealed no transition or voltage fluctuation and the maximum current applied was 200 amps. There is strong evidence of current sharing but not enough to observe a transition.

After the second inch of lead was cut off with the wire saw the same process was performed. With the inner conductor the samples separated easily and with sufficient clean copper wetted very well with standard solder. The outer samples where still poisoned with tin and were difficult to wet with solder.

The I-V short sample curves are presented below. Figure 80 displays the voltage range for the outer cable samples and Figure 81 for the inner cable samples. The outer cable samples did not display any superconducting transition. There was a transition between nucleate boiling and film boiling at about 0.9 W / cm^2. For the second cut inch the calculated bridge resistance without superconductor based on the cross section of stainless steel and solder should be between 9 and 15 μΩ. The measured resistances are indicated in Figure 80 for the outer conductor and are larger than if the superconductor was not present. This is a strong indication that little or no supercurrent was being transferred by the superconducting strand and thus no current sharing.

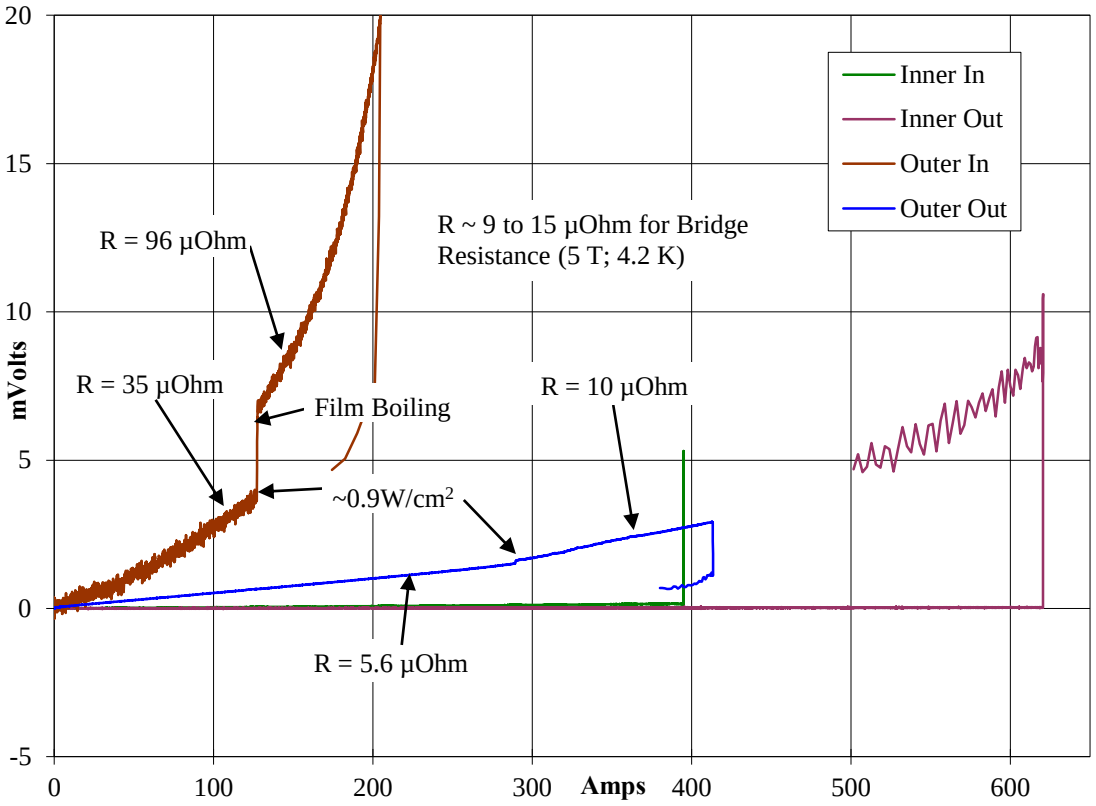

Figure 80: Voltage vs. Current for Cut Leads (High Voltage Scale)

The story in Figure 81 for inner conductor is much better. A sharp transition was witnessed in each sample with a critical current of 397 amps and 616 amps respectively at 5 tesla and 4.2 kelvin. The joint resistance was 398 nΩ for the inner in sample and 53 nΩ for the inner out sample.

The peak field at the leads is about 1.3 tesla from simulation and the samples were tested at 5 tesla. From load line data, the required current at 1.3 tesla and 4.2 kelvin is 420 amps for the inner conductor and 371 amps for the outer conductor. By looking the Ic ratio between 1.3 tesla and 5 tesla the current that each strand would need to carry at 5 tesla would need to be 175 amps for the inner conductor and 154 amps for the outer conductor.

The short sample tests for inner conductor was a success with each sample carrying almost 400 amps. The outer conductor short sample tests were a failure with no

superconducting transition. The failure of the outer conductor tests is largely thought to be due to our inability to introduce current into the superconductor through the lack of clean copper on each strand.

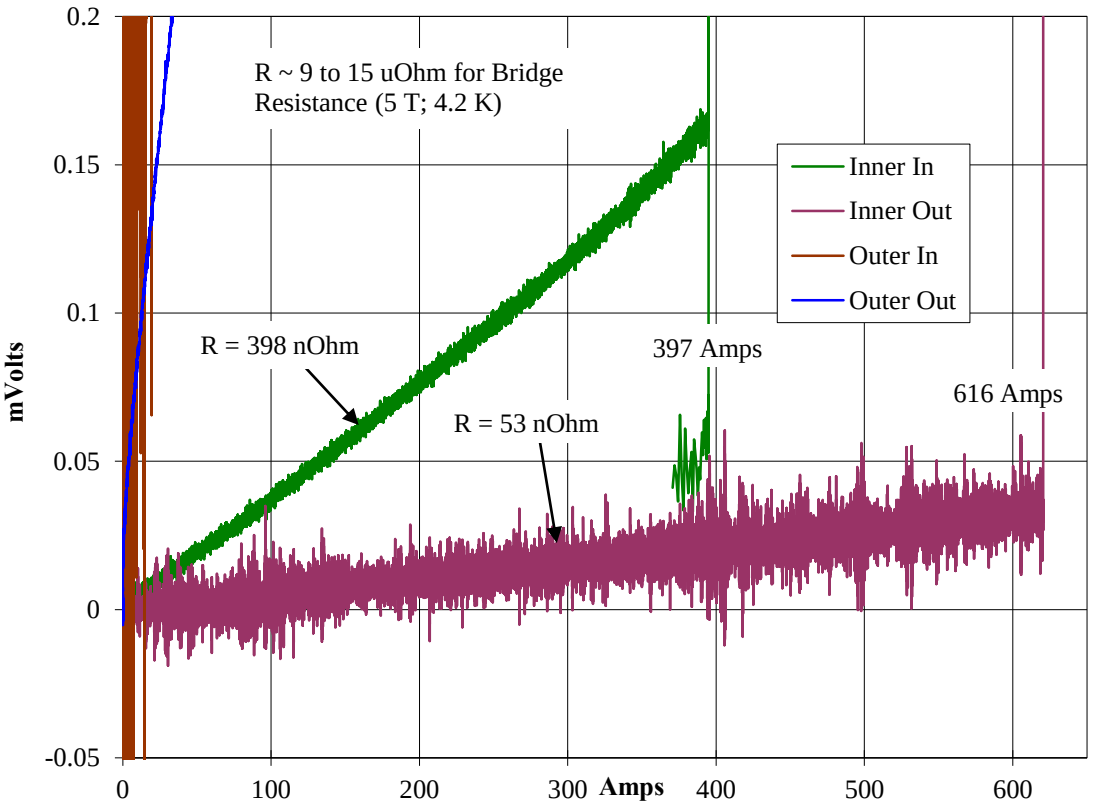

Figure 81: Voltage vs. Current for Cut Leads (Low Voltage Scale)

5.2.8 Conclusion

In conclusion, after heat treating TAMU3a several deposits of elemental tin were found along with dark discoloration along the central mandrel. The discoloration in the S-Glass was determined to be from the silane based sizing and lubricant used during the insulation process. The primary cause of the leaked tin was the omitted 210°C solid

diffusion stabilization soak. However, tin also leaked to a much lesser extent in TAMU3b and in tin leaked in the body of the magnet in TAMU3c despite including the 210°C solid diffusion stabilization soak for both coils. A secondary cause may be that the intermediate copper anneal while cabling enabled hard bronzes to form and break Niobium bundle barriers despite the cable forming process otherwise following standard parameters and operating procedures.

Construction of TAMU3a was terminated after determining that an insufficient amount of supercurrent could be transferred to the superconductor through the poisoned outer stabilizing copper at the leads despite strong evidence that the cable contained ample fine grain Nb_3Sn. Continuing the construction of TAMU3 was deemed irresponsible and the coil was then autopsied with the piece parts recycled for TAMU3c. There were no internal tin leaks besides the weld arc. The only other mentionable was that one of the Rutherford cables slightly deregistered at the lead end chicane.

5.3 Electrical Tests

There are three predominate resistances that are imperative to observe for a superconducting magnet; the coil resistance, the turn-turn resistance and the resistance to ground. The coil resistance is often presented as an RRR value rather than a bulk resistivity because it better indicates the purity of the stabilizing copper. The turn-turn resistance is difficult to measure directly because the resistance of the cable is small relative to any soft turn-turn short. The resistance to ground is very important for safely operating the magnet during a quench.

5.3.1 Coil Resistance

The cable resistances for TAMU3b and TAMU3c were measured in identical fashion to the process described in the TAMU3a analysis section. The inner cable is identical in both TAMU3c and TAMU3b. The outer conductor in TAMU3c is made with identical strand but a slightly different cabling procedure.

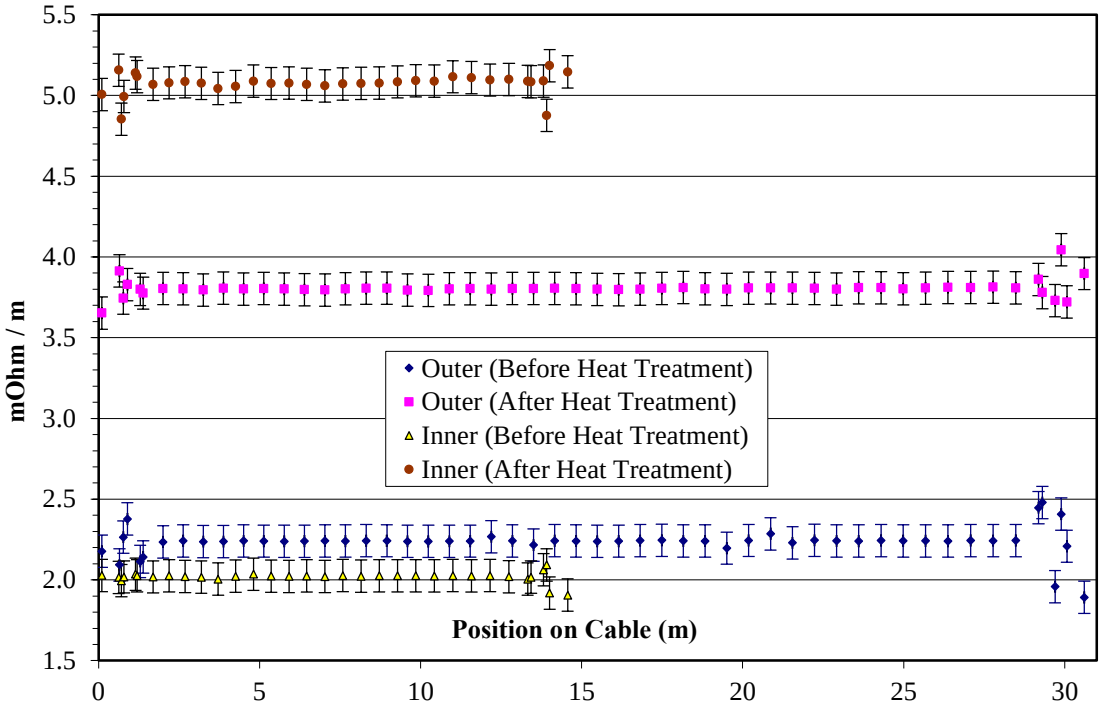

Figure 82: TAMU3b Coil Resistance per Length

5.3.1.1 TAMU3b Coil Resistance

The resistance per length of cable for TAMU3a is shown in Figure 82. Cross sections were re-analysed using ImageJ®. The calculated and measured resistance per length is presented in Table 18.

Table 18: Summary of Measured and Calculated Resistance per Length

(mΩ / m)	Measured		Calculated	
	Inner	Outer	Inner	Outer
Unreacted	2.03	2.24	2.08	2.35
Reacted	5.08	3.80	2.42	2.74

The results shown in Table 18 are very similar to those presented with TAMU3a. The unreacted measured and calculated resistance per length are in excellent agreement with just a few percent difference. The reacted resistances (calculated and measured) for the outer conductor disagree by about two and a half standard deviations which again is very similar to TAMU3a data. The reacted resistances (calculated and measured) for the inner conductor disagree by over 6 standard deviations.

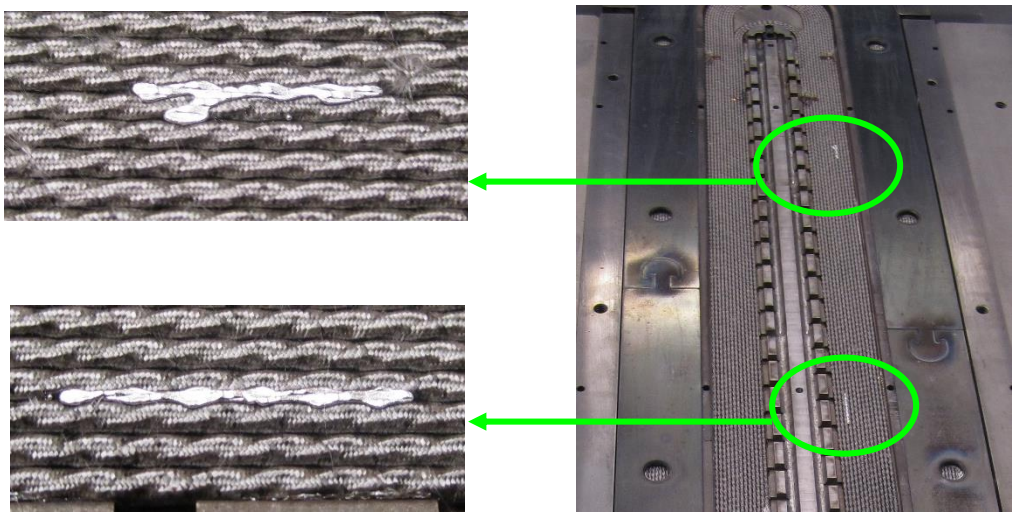

Figure 83: Locations of Leaked Tin in the Inner Coil Body of TAMU3b

Problems in the inner coil are further indicated by two loose segments of leaked elemental tin from the body of the inner coil in TAMU3b. A picture of the leaked tin locations are shown in Figure 83.

5.3.1.2 TAMU3c Coil Resistance

The outer conductor of TAMU3c is made of the same superconducting strand (54/61 RRP®) as TAMU3a and TAMU3b but with drastically different after heat treatment

resistivity. As Figure 82 and Figure 84 indicate the resistance per length decreased from 3.81 mΩ / m to 2.89 mΩ / m or a 25% decrease. All other resistance differences between coils were within a few percent. There was also large amounts of tin leakage in the body of the outer coil in TAMU3c as shown in Figure 85. There were no visible locations of leaked tin in the body of the inner coil of TAMU3c as there were in TAMU3b.

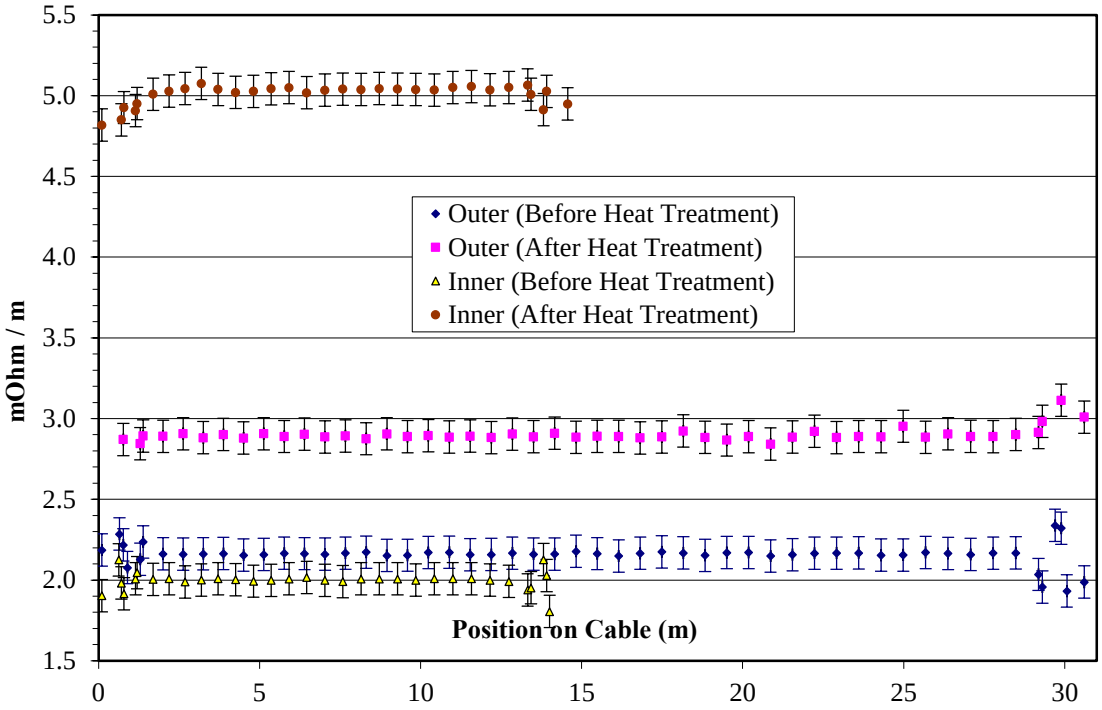

Figure 84: TAMU3c Coil Resistance per Length

One possible explanation for the decrease in resistance per length is that the new cabling procedure drastically weakened the integrity of the niobium barriers and allowed tin to locally burst out of the strands and through the S-Glass insulation. The S-Glass does not wick the tin and inhibits the tin from further poisoning the copper. With this localized absence of tin where the copper was previously being poisoned the resistance per length was allowed to remain low even after the heat treatment.

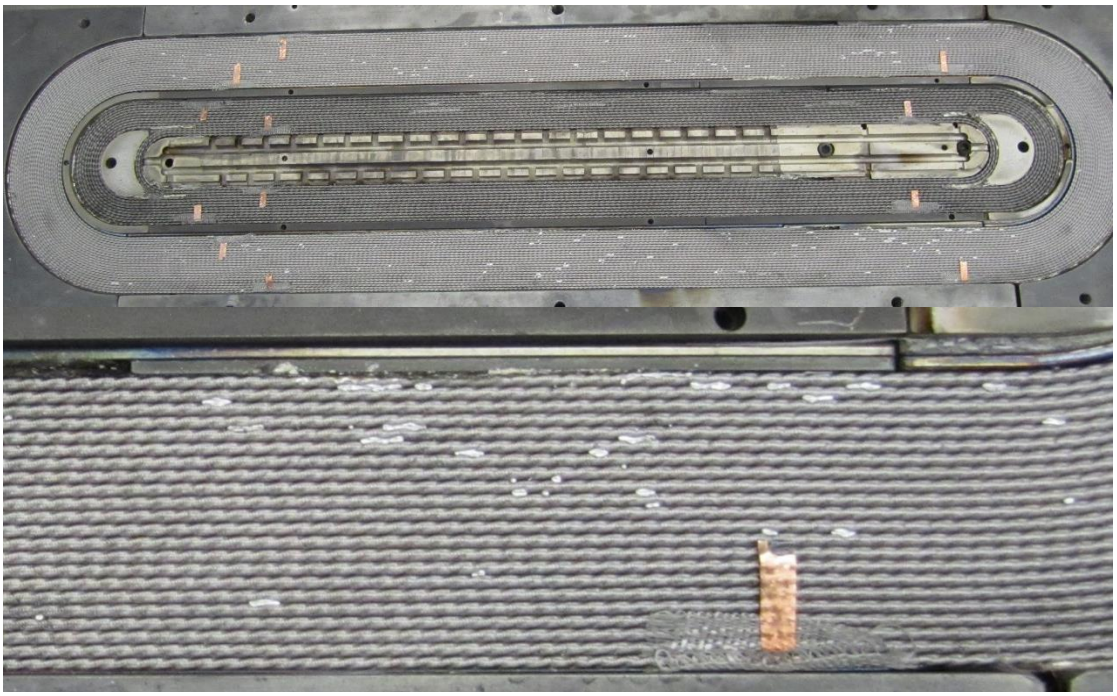

Figure 85: Leaked Tin in the Body of the Outer Coil in TAMU3c

5.3.1.3 Cabling Parameters

The cabling machine operators at LBNL have accumulated considerable data on how much deformation is acceptable for several different types of superconducting Rutherford type cable. According to Dietderich et al. [91] there are two parameters that define if a Rutherford cable will be damaged or mechanically stable. They are the thickness deformation:

$$Thickness\ Deformation\ (t) = \frac{cable\ thickness}{2 \times strand\ diameter} - 1 \quad \textbf{(8)}$$

and the *width deformation*:

$$Width\ Deformation\ (w) = \frac{cable\ width - theoretical\ width}{theoretical\ width} \quad \textbf{(9)}$$

where the *theoretical width* is given as:

$$theoretical\ width = \frac{Nd}{2\cos(PA)} + 0.72d \quad \textbf{(10)}$$

where N is the number of strands, PA is the Pitch Angle and d is the strand diameter.

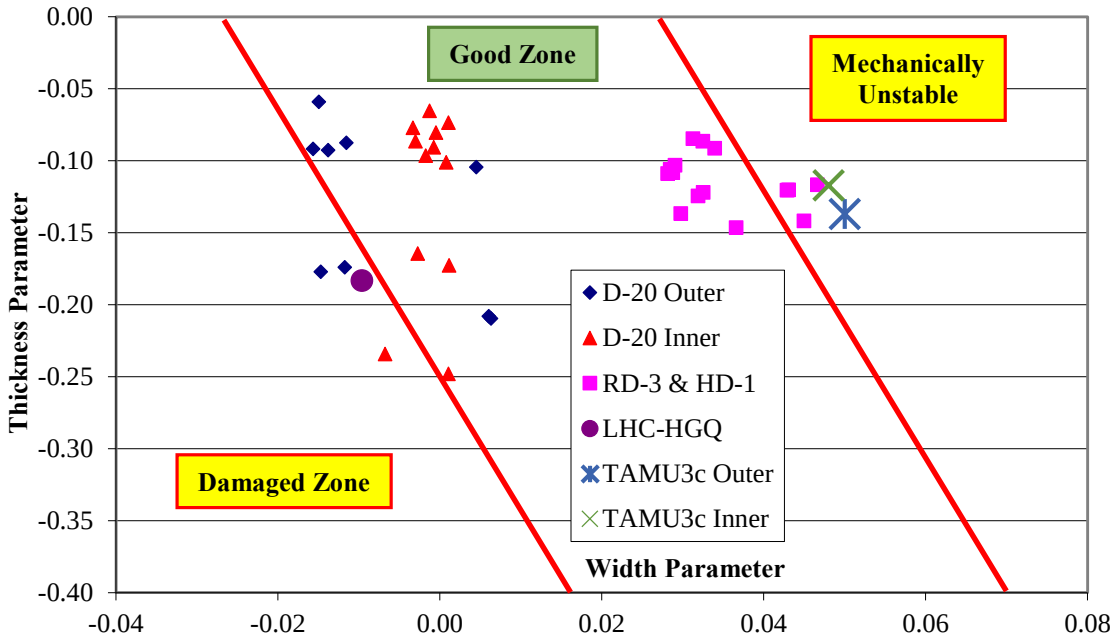

Figure 86: Internal Tin, MJR, and RRP Conductor and Deformation Parameters

The data in Figure 86 does not include the 0.72d following the precedence of Dietderich et al. [91]. From each data point listed in Figure 86 there were no reports of leaked tin. The cable in the damaged zone namely the HGQ and D-20 cable reported roughly a 5% decrease in J_c and 50% decrease in stability current. Using TAMU3 cable data the inner cable has a width and thickness deformation of 0.048 and -0.117 and the outer cable has a width and thickness deformation of 0.050 and -0.137 respectively. These two points are plotted in Figure 86 and fall within the mechanically unstable range. They are very safe in terms of potential over-cabling or keystone damage to the cable. Therefore it is very unlikely that over-cabling caused the leaked tin seen in TAMU3c outer conductor.

5.3.2 Turn-Turn Resistance

Based on the turn-turn voltages while measuring the resistance per length we can place a lower bounds on the turn-turn resistance between voltage measurements. By

assuming that the cable and the short are parallel resistances we derive what the lowest turn-turn resistance might be. The minimum turn-turn resistance $R_{turn\text{-}turn}$ can be found from:

$$R_{turn-turn} = \left(\frac{1}{r_{min}L} - \frac{1}{r_{coil}L}\right)^{-1} \quad \textbf{(11)}$$

where L is the length of one turn (1.3 meters), r_{coil} is the average resistance per length of the coil and r_{min} is the minimum resistance per length. From these assumptions and the data in Figure 82 and Figure 84, the minimum turn-turn resistance is about 120 Ω. This is sufficiently high of a resistance to safely protect the coil during a quench.

5.3.3 Resistance to Ground

The resistance to ground is constantly monitored while winding so that any problems can be quickly identified and remedied without having to disassemble any tooling. The cables are connected to a buzz box so that an audible signal is heard when a hard short forms. Prior to heat treatment the resistance between the coil and the magnet tooling is greater than 20 GΩ which is the highest sensitivity of a standard DMM. After heat treatment leaked tin at the welded ends of the cable created hard shorts. After removing the splice blocks there remained a 100Ω to several kΩ resistance between the cable and the magnet tooling.

The process of VPI effects the resistance to ground in varying degrees. A plot of the resistance to ground of the outer coil is shown in Figure 87. The resistance to ground as a function of time during VPI of the inner coil is shown in Figure 88.

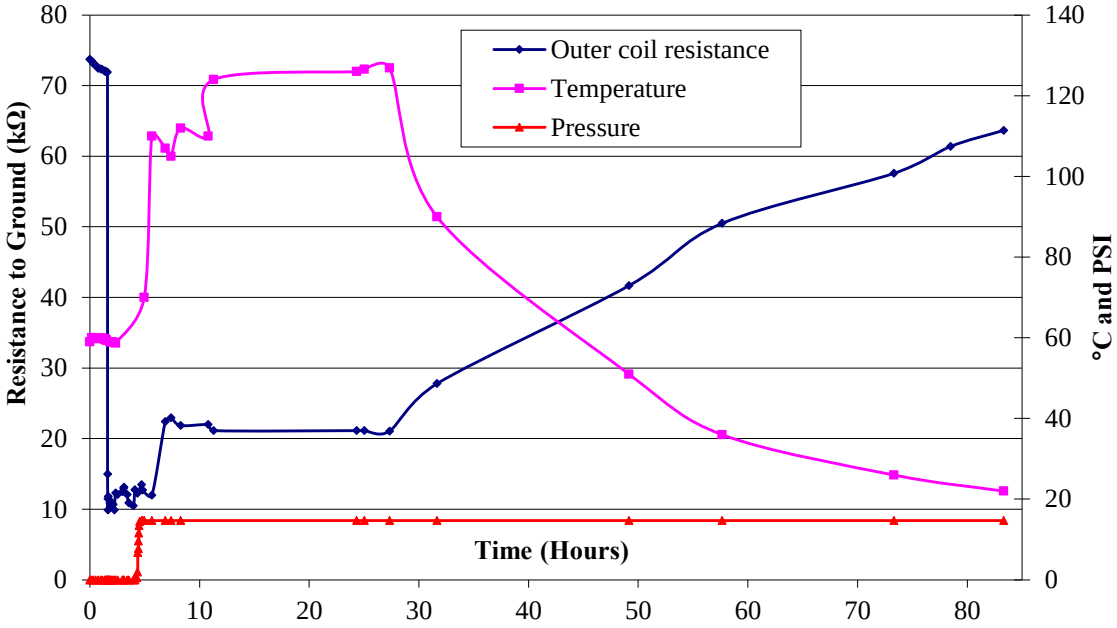

Figure 87: TAMU3b Outer Coil Resistance to Ground During VPI

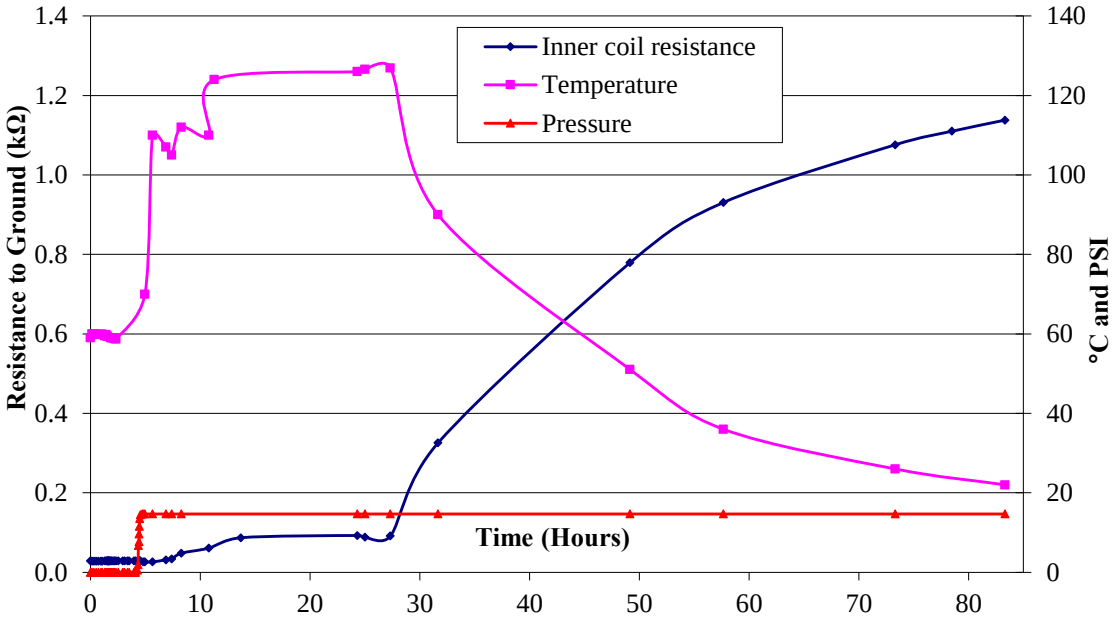

Figure 88: TAMU3b Inner Coil Resistance to Ground During VPI

After heat treatment the outer coil started at 72 kΩ and quickly plummeted to 10 kΩ over the span of 20 seconds as epoxy began flowing over the outer coil. The large drop was unexpected and the cause is unknown. The resistance quickly jumped to 22 kΩ when the curing cycle began and steadily climbed to 65 kΩ as the magnet cooled.

The resistance of the inner coil to ground started at 70 Ω after reaction bake. Applying pressure to the top of the winding package near the short as indicated in the top left arrow in Figure 89 caused the resistance to decrease. The resistance dropped to 22 Ω while soldering voltage taps and welding closed the magnet. The resistance stayed at that value while the epoxy was flowing. It increased to 29 Ω when the impregnation vessel was backfilled with air and decreased to 26 Ω when heat was first applied. The resistance increased to 90 Ω as the epoxy cured and rested at 1.08 kΩ when fully cured and at room temperature. The middle bottom arrow in Figure 89 indicates where the soft short was located after impregnation.

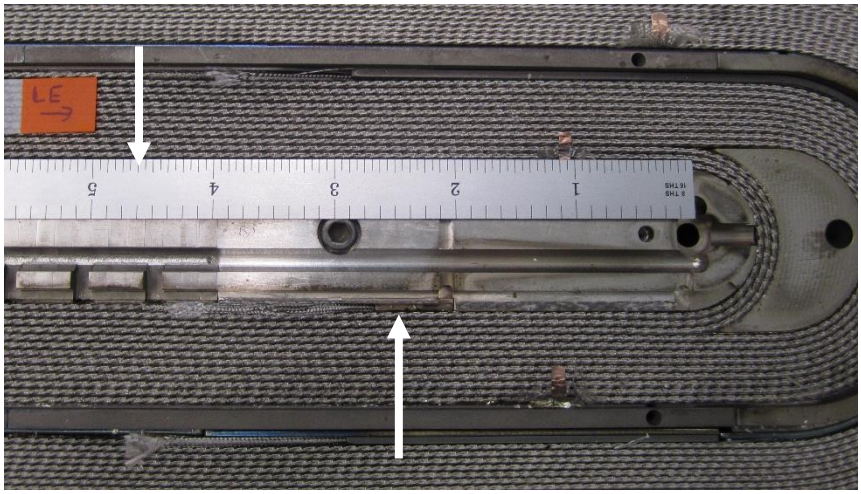

Figure 89: Lead End of TAMU3b After Heat Treatment

From the previous results the effect of VPI on the resistance to ground varies widely with the magnitude and location of the short. For TAMU3c, the inner resistance to ground increased from 125 Ω to 255 Ω and the outer coil resistance to ground increased from 1.2 kΩ to 2.5 kΩ. Therefore as a general rule for soft shorts, VPI is able to double the resistance to ground of superconducting coil.

5.4 Transducer and Strain Gauge Calibration

All transducers and strain gauges were developed, fabricated, and calibrated at the TAMU ARL. As previously discussed the accuracy and repeatability for both the transducers and strain gauges are quite remarkable.

5.4.1 Transducer Calibration

The raw data for each transducer in TAMU3 is presented in Table 19. The extrapolated capacitance at 0 psi is calculated from the slope of the capacitance between 2000 and 5000 psi. The calibration procedure included cycling the transducer to 5000 psi at room temperature to get a baseline response. Then the transducer was cycled while submerged in liquid nitrogen at 77 kelvin twice to 2000 psi, thrice to 5000 psi and thrice to 10,000 psi. Liquid nitrogen is an acceptable temperature to calibrate the transducers because 90% of the Young's modulus change for polyamide materials occurs between room temperature (210 ksi) and 77 kelvin (760 ksi at 77 kelvin and 820 ksi at 4 kelvin) [68]. This enabled a full test for any creep, instability, or failure to occur and be accounted for. Figure 90 shows a typical calibration curve for a TAMU3 transducer. The statistical spread of the calibration data is quite small. The average transducer response is 167 ± 6 ksi / nF with a baseline capacitance of 5.64 ± 0.20 nF at 77 kelvin and 0 psi.

Table 19: Laminar Stress Transducer Calibration Data

Capacitance (*nF*)		0 psi		2000 psi		5000 psi		Δ psi / Δ nF	
Transducer #		1 kHz	10 kHz	1 kHz	10 kHz	1 kHz	10 kHz	1 kHz	10 kHz
TAMU3b	1	5.858	5.852	5.871	5.864	5.890	5.882	1.600E+05	1.667E+05
	2	5.611	5.603	5.622	5.614	5.639	5.631	1.786E+05	1.786E+05
	3	6.041	6.033	6.053	6.045	6.071	6.063	1.667E+05	1.648E+05
	4	5.470	5.461	5.482	5.473	5.500	5.491	1.667E+05	1.667E+05
	5	5.673	5.665	5.685	5.677	5.702	5.695	1.744E+05	1.667E+05
	6	5.814	5.807	5.826	5.818	5.844	5.836	1.648E+05	1.705E+05
	7	5.662	5.654	5.675	5.667	5.695	5.686	1.515E+05	1.579E+05
TAMU3c	1	5.579	5.572	5.591	5.584	5.608	5.602	1.711E+05	1.648E+05
	2	5.352	5.345	5.364	5.357	5.381	5.374	1.731E+05	1.724E+05
	3	5.414	5.406	5.425	5.417	5.441	5.434	1.815E+05	1.751E+05
	4	5.727	5.717	5.740	5.730	5.759	5.749	1.568E+05	1.568E+05
	5	5.575	5.568	5.590	5.579	5.605	5.597	1.667E+05	1.724E+05
	6	5.286	5.278	5.299	5.291	5.317	5.310	1.630E+05	1.579E+05
	7	5.870	5.859	5.882	5.871	5.899	5.889	1.731E+05	1.698E+05
$\overline{C}$ =		5.652	5.644	5.664	5.656	5.682	5.674	1.675E+05	1.667E+05
σ_C=		0.207	0.206	0.207	0.207	0.207	0.207	7.8E+03	6.1E+03

Above roughly 500 psi the transducer response is very linear. The uncertainty associated with the statistical spread of the slopes shown in Table 19 is roughly 5%. The uncertainty in measuring pressure and the LCZ meter is ± 0.1 ksi and ± 0.001 nF respectively. For each measurement two data points are taken: one at 1 kHz and another at 10 kHz. For an example, at short sample the current is 13.72 kA and the force on the left lead end transducer of TAMU3b (transducer #1) is simulated to be 74.9 MPa ± 3.4 MPa based on Vector Field® simulation and current measurement uncertainties. By summing each error in quadrature the expected response of the transducer would be 74.9 MPa ± 3.1 MPa.

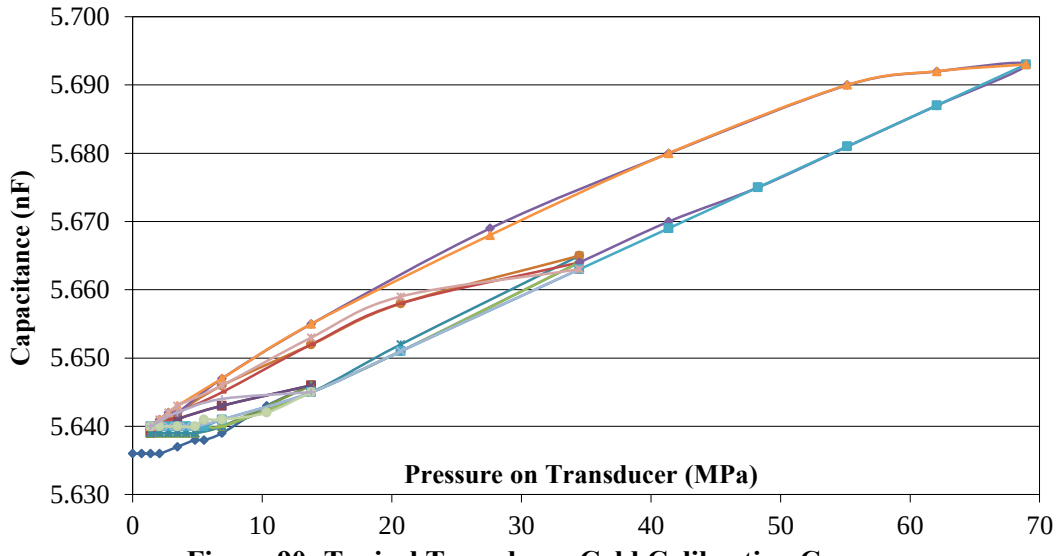

Figure 90: Typical Transducer Cold Calibration Curve

Transducer data collection will occur while the magnet is in DC mode because the kHz signal will trip the QDC and prematurely quench the magnet. Data from select transducers will be collected at both 1 and 10 kHz and compared to what is expected for a given magnet current. This is one of the primary tests for stress management.

5.4.2 Strain Gauge Calibration

There are 4 strain gauges that are placed between the end shoe of each coil and the support structure for a total of 16 strain gauges. A combination of force sensitivity and range requirements and available cross sectional footprint drove the current design used for the strain gauges. The strain gauges components were purchased from Vishay Micro-Measurements® division (Part # J2A-13-S108F-10C/SP62 with M-Bond 610®.) The recommended procedure for fabricating the strain gauges was carefully followed [92] and specialized fixturing was constructed to reduce non-uniformities and aid in the fine details of fabrication. Figure 91 shows a strain gauge puck during construction in the fabrication tooling. Figure 92 shows four completed strain gauges after being completely cured, wired and varnished.

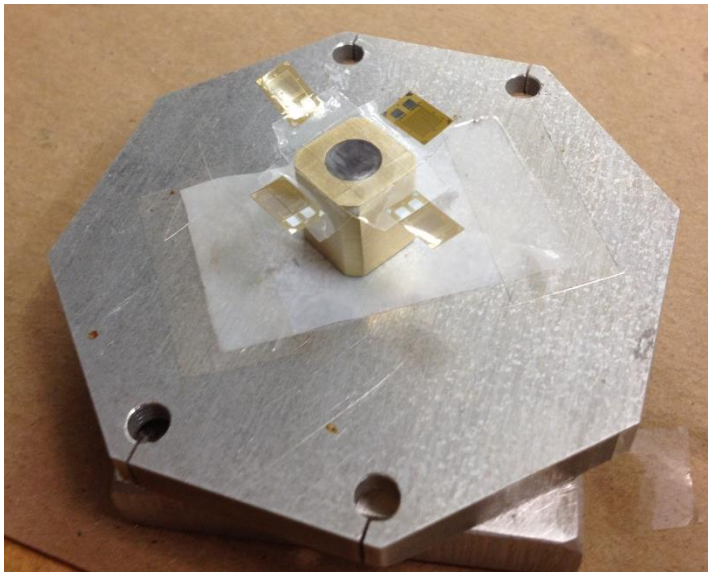

Figure 91: TAMU3 Strain Gauge During Fabrication

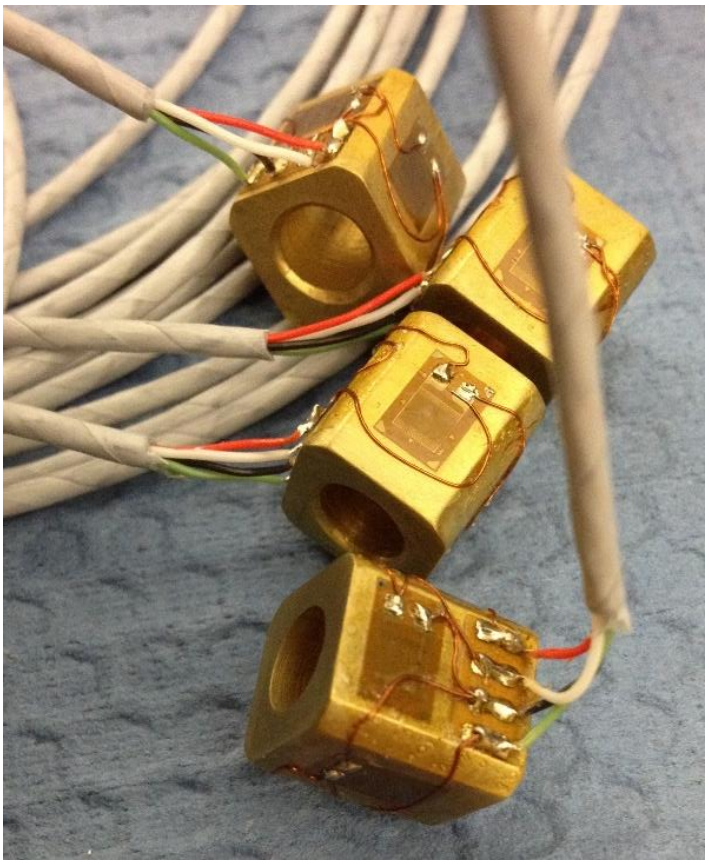

Figure 92: Completed Strain Gauges

TAMU2 was tested with half-bridges with a high rate of failure. The error associated with the data was also quite large. The TAMU3 gauges were constructed to form a full-bridge with four independent gauges comprising the full-bridge. They are designed to measure up to 12,000 lbf at ± 8.3 lbf accuracy as measured with a Model P3 strain gauge indicator recorder from Vishay® micro-measurements division as shown in Figure 93.

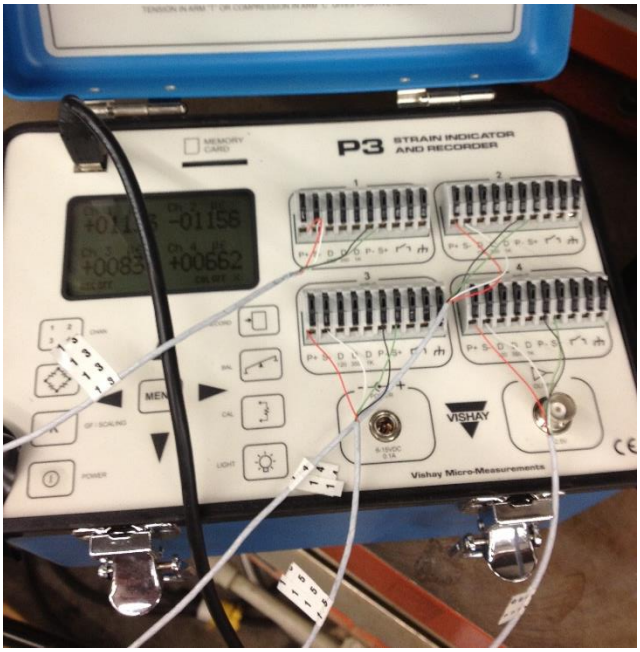

Figure 93: P3 Strain Indicator from Vishay Micro-Measurement®

The strain gauges were first warm tested to 12 ksi. Each gauge began to plastically deform at roughly 15 ksi at room temperature. The graphical results of this initial calibration is shown in Figure 94. The results are somewhat perplexing because the µ-strain at no pressure should be zero but the results are quite varied ranging from zero to 1500 µ-strain. The only sources of variation this large would only be fabrication inconsistencies and curing each gauge at elevated temperatures. The cure cycle is an hour at 160°C and an hour post cure at 210°C. Another potential source of variance could be

from the peak strain gauge temperature while soldering 38 gauge wires or differing surface pressures while curing the gauges. Despite the wide range of zero point strains, accurate calibration can still be obtained.

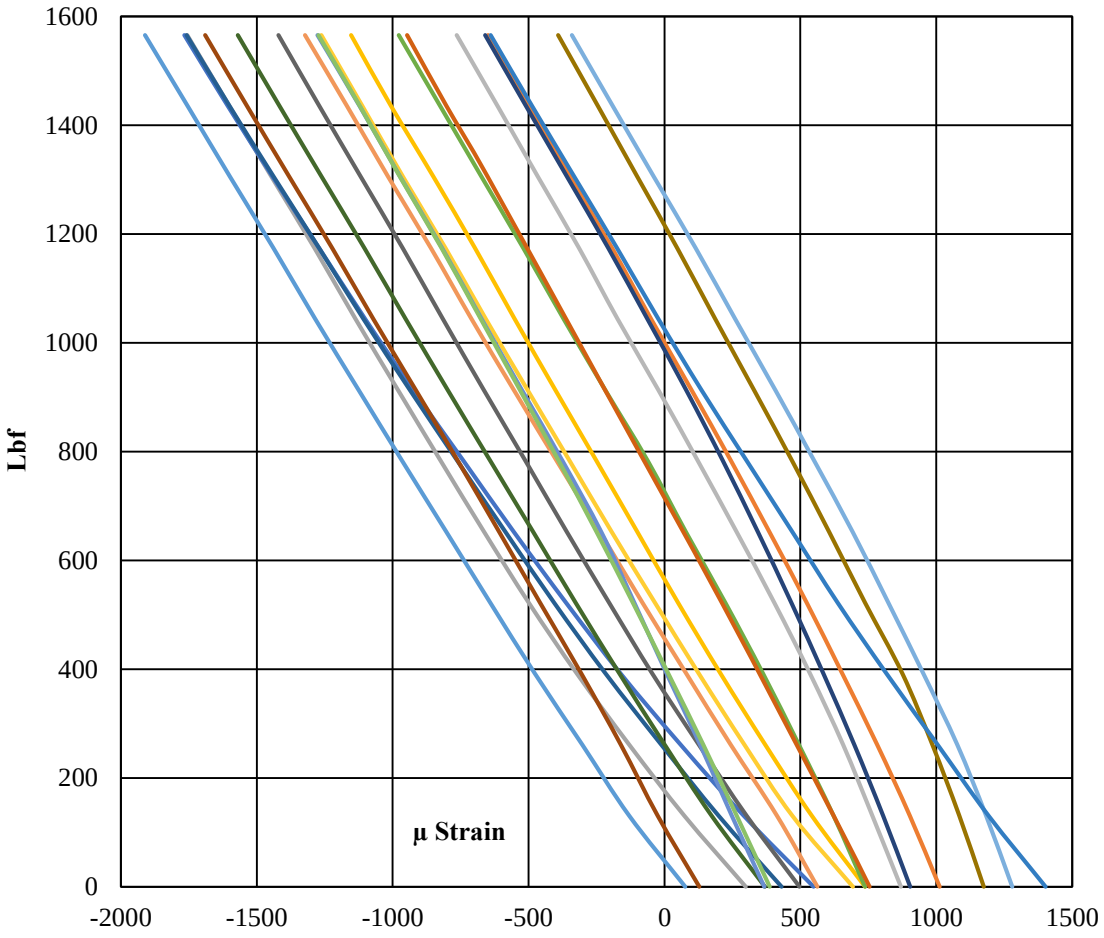

Figure 94: Warm Calibration Curves for 20 Strain Gauges

The quadratic calibration results are presented in Table 20. The formula for calculating the force from the measured μ-strain is given as

$$force\ (lbf) = a(\mu\varepsilon)^2 + b(\mu\varepsilon) + c \quad \textbf{(12)}$$

where $\mu\varepsilon$ is the μ-strain as measured by the P3 Strain Indicator and all other variables are given in Table 20. There are several uncertainties to account for when giving a final result for force: the uncertainty in Table 20, 0.1% error in reading, ± 3 counts from P3 Strain Indicator, and ± 1 count from zero point shifts.

It is difficult to present expected data from the strain gauge because friction-lock is an untested strategy for managing axial Lorentz force at high field. The base installation pressure is 500 lbf on each strain gauge. This corresponds to 60 ± 10 inch-lbf of torque for a dry bolt and 30 ± 5 inch-lbf of torque for a lightly lubricated bolt. At 500 lbf on each gauge the uncertainty in measurement would range anywhere between 6 and 14 lbf.

Table 20: Quadratic Strain Gauge Calibration

	Quadratic Regression				**Micro Strain Zero Points**	
SG#	a	b	c	σ_f[Lbf]	LN_2	RT
SG1	1.15E-05	-0.971	79.6	4.3	91	79
SG2	-1.01E-04	-1.043	1174.1	5.2	1022	1014
SG3	7.98E-05	-0.848	245.1	9.3	319	303
SG4	1.14E-04	-0.886	562.4	11.5	720	739
SG5	9.94E-05	-0.705	309.4	3.5	480	553
SG6	-1.34E-05	-1.096	706.2	7.7	654	739
SG7	8.87E-05	-0.768	303.7	2.5	421	434
SG8	-1.73E-05	-1.019	161.8	3.5	160	131
SG9	8.86E-05	-0.896	373.0	10.2	455	500
SG10	-6.73E-05	-1.052	1291.8	3.9	1140	1175
SG11	-1.15E-04	-1.059	1023.7	5.7	879	906
SG12	6.50E-05	-0.899	286.2	8.1	344	371
SG13	-8.57E-05	-1.045	1291.4	5.2	1131	1283
SG14	1.62E-05	-0.941	489.1	3.7	522	566
SG15	-4.40E-05	-1.078	921.7	3.4	831	873
SG16	3.45E-05	-1.024	647.9	6.4	660	697
SG17	-3.96E-05	-1.070	378.8	6.9	341	369
SG18	-1.12E-04	-1.161	465.0	7.4	384	390
SG19	6.59E-05	-0.908	1086.4	3.4	1333	1407
SG20	5.55E-05	-0.944	263.1	30.8	229	234

5.5 AC Losses and Effects

5.5.1 Introduction

A Type II superconductor is different than a Type I in that it allows flux to penetrate the superconductor in the form of trapped flux quanta inside current loops called fluxoids. AC losses arise in any Type II superconductor due to moving fluxoids. Changing currents or changing magnetic fields cause the fluxoids to move and create heat even though the material remains superconducting. The ideal superconductor has strong flux pinning centers that tend to inhibit fluxoid motion and have large transport current capabilities and less intrinsic AC loss. Another direct source of AC loss is in Faradays law applied in the normal metals. The driven eddy currents also create heat from changing flux.

The outpouring effects of AC loss wreak havoc on superconducting magnet use in AC applications including persistent current magnetization and the snap-back phenomenon first witnessed in the Tevatron and simulated and accounted for in every superconducting synchrotron since [93, 94]. Fast ramping magnets for GSI and the SIS100 and SIS300 synchrotrons in Germany are a pressing and challenging task [95-97]. These fast ramping magnets must have strongly decoupled strands and filaments to minimize all AC loss. This section will discuss both qualitatively and quantitatively the advantages that a block coil geometry has with respect to AC losses.

5.5.2 Snap-Back

At injection fields for a synchrotron the persistent current magnetization decays rather slowly with decay times on the order of hours or days. These persistent currents are relatively large and have a significant impact on the uniformity of field [98, 99]. Immediately upon beginning to ramp the field, the persistent current magnetization will suddenly reappear or snap-back to the original levels and the accelerated particle beam will disintegrate. The snap-back phenomenon originates from gradient forces on the magnetization current loops within the filaments. Equation (13) indicates the force placed on each current loop and how it is in the direction of the gradient of the magnetic field.

$$\vec{F} = (\vec{\mu} \cdot \vec{\nabla})\vec{B} \quad \textbf{(13)}$$

In a cosine theta magnet the gradient is predominately parallel to the broad face of the Rutherford cable and in a block geometry the gradient is perpendicular to the broad face. In a cosine theta magnet the magnetization currents travel the width of the cable and in a block dipole the magnetic moments travel the thickness of the cable. Snap-back is also suppressed with an iron boundary condition above and below the bore.

Another method to minimize the snap-back phenomenon is to introduce an iron sheet above and below the bore. The iron acts like a dipole boundary condition at field sufficiently below iron saturation and suppresses higher order multipoles due to persistent current magnetization. This flux plate is potentially able to suppresses the sextupole field by a factor of 5 [100].

5.5.3 Sources of AC Loss

The sources of AC loss are separated into intrinsic and extrinsic losses at the strand and cable levels. Intrinsic magnetization and intra-strand losses dominate at low field. At higher field strengths the inter-strand coupling losses are larger [101]. AC loss is minimized in the block coil geometry.

5.5.3.1 Intra-Strand Losses

Intra-strand AC losses are intrinsic to the superconducting wires that comprise the Rutherford type cable. There are three losses associated at a strand level: the hysteresis or magnetization loss, the transport current loss, and the inter-filament coupling current (IFCC) loss. Here we will briefly discuss the stability for a strand and how it relates to average power dissipated from the three aforementioned sources of intrinsic AC losses.

The magnetization loss per cycle for a single filament between fields B_1 and B_2 as derived by Niessen [102] is given as

$$Q_{hys} = \frac{4aJ_0B_0}{3\pi}\ln\left(\frac{|B_2| + B_0}{|B_1| + B_0}\right) \ [\mathrm{J/m^3/cycle}] \quad \textbf{(14)}$$

where J_0 is the current density at B_0 field and a is the effective filament diameter. For a single strand the total hysteresis loss is proportional to the effective filament diameter, the current density, and the magnetic field value. From G. H. Morgan [103] the average power dissipated per unit length for twisted multicore wire is given as the following:

$$\langle P \rangle = \left(N/\sqrt{3}\right)(2/\pi^2)\left(d^2L^2\dot{B}^2/\rho\right) \quad \textbf{(15)}$$

where N is the number of filaments, d is the filament twist diameter, L is the twist pitch, $\dot{B}$ is the changing magnetic field and ρ is an effective resistivity. Notice that the power loss is proportional to the square of the filament twist diameter, the square of the twist pitch, and the square of the field sweep rate. Minimizing the effective filament twist diameter and twisting the filaments in as short of distance as possible will minimize the intrinsic AC loss associated with the strand.

Coincidently there is a stability criterion for superconducting strands that is appropriate to include in this discussion. One form of conductor stability is determined when the specific heat of the surrounding material can take an equivalent energy increase from a flux jump which is a form of microscopic AC loss.

$$\gamma C(T - T_0) > \frac{\mu_0 J_C^2 a^2 (T - T_0)}{3(T_C - T_0)} \quad \textbf{(16)}$$

In equation (16), γ is the mass density, C is the specific heat, T is the temperature, T_0 is the cryogen temperature, T_C is the critical superconductor temperature, J_C is the current density and a is the filament diameter [10]. Equation (16) is called the adiabatic stability criterion for filamentary conductor. The primary link to intrinsic ac loss has to do with the filament diameter. The AC loss associated with a filament increases like the square of the filament diameter just as this stability criterion is dependent on the square of the filament diameter.

For our conductor (54/61 RRP®) the effective filament size is approximately 83 microns. Equation (16) can be used to determine adiabatic stability for the effective filament size and the result is given in Equation (17).

$$\frac{3\gamma C(T_C - T_0)}{\mu_0 J_C^2} > a^2 \quad \textbf{(17)}$$

The Nb_3Sn conductor is most unstable against flux jump instability at low field between 0 and 3 tesla where the current density is the highest. For TAMU3 conductor the ideal filament size would need to be roughly 24 microns. For full adiabatic stability against flux jumps in typical Nb_3Sn conductor the filament size needs to be between 11 and 35 microns [104, 105]. The current state of the art Nb_3Sn internal tin conductor (198/217 RRP®) has an effective filament diameter of 41 microns [106]. Full adiabatic stability and smaller filament size at 31 microns can be achieved with a powder-in-tube (PIT) Nb_3Sn conductor but with reduced current density [107].

5.5.3.2 Inter-Strand Losses

Inter-strand coupling currents (ISCCs) are created when non-insulated strands of a cable are exposed to time varying magnetic fields. This extrinsic effect adds to the intrinsic AC losses due to magnetization hysteresis and IFCCs. The most comprehensive treatment for AC current losses is by A.P. Verweij [101]. However a less robust approach can be taken for estimating losses and especially for comparing losses in different dipole geometries. The approach taken by M.N Wilson [10, 108, 109] will be followed where the cable is assumed to have infinite length with crossover and adjacent resistances.

First we define a crossover resistance, R_c, for a Rutherford type cable as the contact resistance between two crossing strands. We also define an adjacent resistance, R_a, as the contact resistance between two adjacent strands. The adjacent resistance is defined over the same length that defines the resistance R_c as shown in Figure 95.

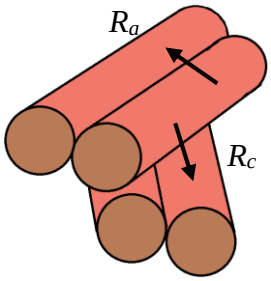

Figure 95: Crossover and Adjacent Resistances R_c and R_a

Now we are able to look at the three main inter-strand coupling losses. The first is the cable coupling from the crossover resistance in transverse field.

$$P_{tc} = \frac{1}{120}\frac{\dot{B}_t^2 cos^2\varphi}{R_c}\frac{c}{b}pN(N-1) \quad \textbf{(18)}$$

P_{tc} is the coupling loss from the crossover resistance in transverse field per unit volume of cable in W / m^3. In Equation (18), p is the cable twist pitch (not to be confused with the filament twist pitch L), $\dot{B}_t^2$ is the rate of change of field transverse to the axis of the cable, N is the number of strands, φ is the angle between the transverse magnetic field and the unit vector normal to the broad face of the cable, and finally c and b are the half width and half thickness of the cable. The second cable coupling is from the adjacent resistance in transverse field.

$$P_{ta} = \frac{1}{24}\frac{\dot{B}_t^2 cos^2\varphi}{R_a}(N-1)\frac{p}{cos^2\theta} \quad \textbf{(19)}$$

P_{ta} is the coupling loss from the adjacent resistance in transverse field per unit volume of cable in W / m^3. In Equation (19), θ is the slope angle of the wire relative to the cable length. The final cable coupling is from the adjacent resistance in parallel field.

$$P_{pa} = \frac{1}{32}\frac{\dot{B}_p^2}{R_a}(N-1)\left(\frac{b}{c}\right)^2\frac{p}{cos^2\theta} \quad \textbf{(20)}$$

P_{pa} is the coupling loss from the adjacent resistance in parallel field per unit volume of cable in W / m^3. In Equation (20), $\dot{B}_p^2$ is the rate of change of field parallel to the cable.

Now we can analyse Equations (18), (19), and (20) by taking ratios of each contribution to the total AC loss. Immediately from the b / c ratio in Equation (20) we can say that the contribution to AC loss from parallel field is negligible in comparison to transverse field. Also in accelerator dipole geometries the parallel field is nearly zero from the symmetry. So we can safely neglect AC loss from parallel field. From Equation (18) and Equation (19) we see that

$$\frac{P_{tc}}{P_{ta}} = \frac{R_a}{R_c}\left(\frac{N}{5}\frac{c}{b}\cos^2\theta\right) \quad \textbf{(21)}$$

where typical values in the parenthesis are between 40 and 60. This implies that R_c has ~50 times more effect on total AC loss in comparison to R_a. The most common method to

reduce AC loss is to increase R_c by placing a high resistivity core in Rutherford type cable [96, 97, 110-112]. This core is usually a foil on the order of 25 μm thick and is usually made of stainless steel. If the crossover resistance becomes too high then the amount of current share between strands is inhibited and the cable becomes unstable at low to intermediate ramp rates [108].

Now the most important variable in each of these inter-strand AC loss equations is φ, the angle between the transverse field and the broad face normal vector. The AC loss is maximized when the field is perpendicular to the broad face. This occurs when φ is zero as in the mid-plane of a cosine theta magnet as shown in Figure 96. The highlighted lines indicate the largest and smallest path for current for a typical ISCC where the pink is current in the back side of the Rutherford cable. The AC loss is minimized when the field is parallel to the broad face as in the pole turns of a block dipole and to a lesser extent the pole turns of a cosine theta magnet as shown in Figure 97.

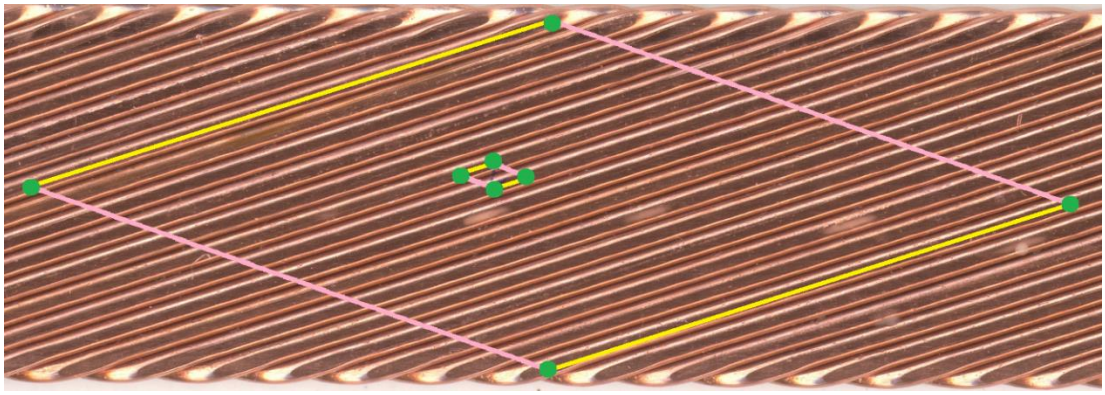

Figure 96: Broad Face of TAMU3 Rutherford Cable

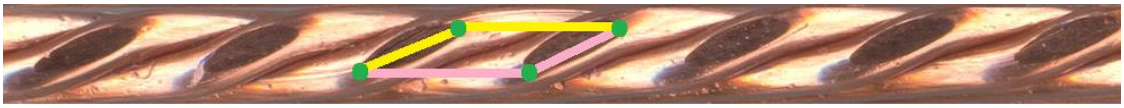

Figure 97: Edge View of TAMU3 Rutherford Cable

Figure 98 and Figure 99 are for a 1 m long LHC type dipole called the Pink Book Dipole (PBD) taken from Verweij's dissertation [101]. Figure 98 shows each winding block and each turn and Figure 99 gives the energy loss per ramp cycle for each block and each turn of the PBD magnet.

In Figure 99 notice that the AC losses are much smaller in the low field windings and that the losses are dominated by filament hysteresis or magnetization loss as discussed above. This is because magnetization loss is maximized at low field where the conductor margin is large and inter-strand loss is minimized because the field change is relatively small. This is also because in the PBD magnet the transverse cross sectional area of each outer coil turn is smaller than each inner coil turn. In the high field region each turn successively reaches a higher magnetic field strength which causes the filament hysteresis and inter-filament losses to gradually increase.

The inter-strand losses are very interesting. In the B3 block the field is perpendicular to the cable face as indicated in Figure 98 and thus the ISCC is at a peak. Even though the magnetic field increases with each successive turn the ISCC decreases because the angle between the cable face and the magnetic field (φ) increases.

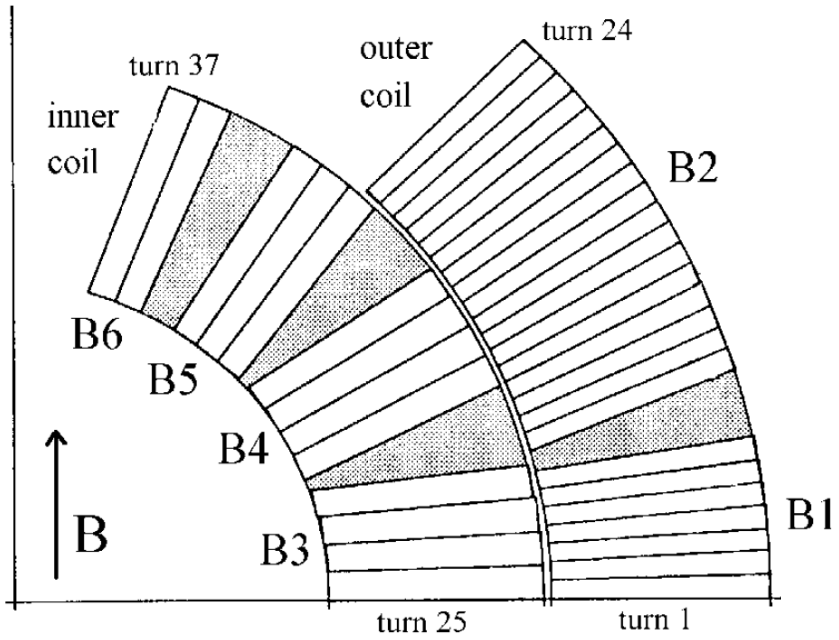

Figure 98: Quadrant of an LHC Type Dipole [101]

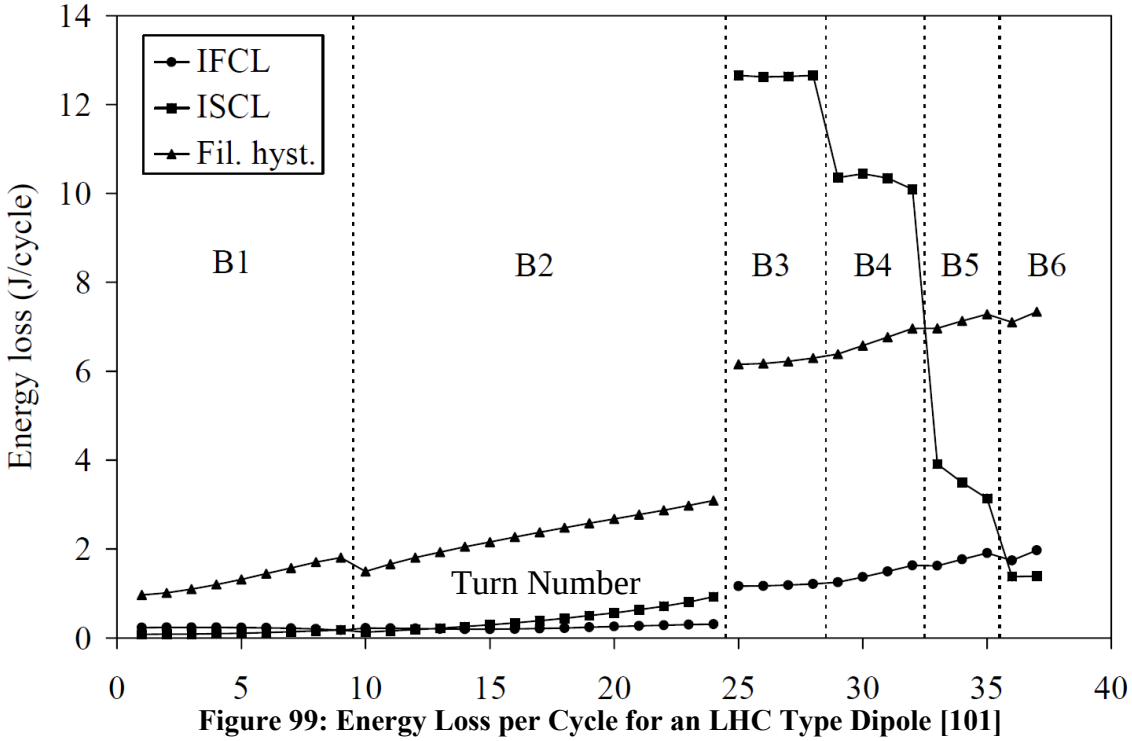

Figure 99: Energy Loss per Cycle for an LHC Type Dipole [101]

In the block dipole TAMU2, the suppression of AC loss was strongly evident. TAMU2 was able to reach 85% of short sample field even at the unheard of rate of 4 tesla per second. This was the fastest that LBNL could ramp a magnet. TAMU2 was AC loss optimized with high inter-filament and inter-strand resistances due to chrome plating bronze-process ITER conductor as well as cable-field orientation. TAMU3 is more susceptible to AC losses because the filaments are larger with less inter-filament and inter-strand resistance. Having a block geometry only reduces the extrinsic inter-strand AC losses in comparison to other geometries. The intrinsic losses are largely unaffected by cable orientation.

5.5.3.3 Boundary Induced Coupling Currents

Boundary induced coupling currents (BICCs) are generated when there are variations in the magnetic field sweep and inter-strand resistances. Simply put, BICCs are long range ISCCs. Most common field and resistance variations occur at splice joints and small radius bends of the Rutherford type cable in accelerator magnets. The mechanics are very similar to ISCCs but with characteristic lengths and times much larger than those originating within the cable pitch length. BICCs are suppressed with the same mechanisms that are used for snap-back and ISCC suppression. BICC losses are proportional to the square of the cosine of the angle between the field direction and cable normal vector and are therefore minimized in the block geometry. For accelerator magnets the BICCs represent only 10% or less of the power loss due to ISCCs [101].

6. CONCLUSION

The Accelerator Research Laboratory in the Department of Physics at Texas A&M University has developed technology in a series of block dipoles to use advanced superconductors to obtain the highest fields possible by employing stress management in the windings. The program has successfully completed and tested TAMU1 and TAMU2 and has completed the fabrication of TAMU3. The next step will be to cryogenically test TAMU3 at LBNL.

6.1 Testing TAMU3

Testing TAMU3 will be a joint effort between the Accelerator Research Lab and LBNL. The test will include low field checks to verify the quench protection circuitry and initialize the transducer data collection. Then a series of high field tests will be performed to observe any training or lack thereof, to document quench propagation, and to determine the peak field dependence on ramp rate. During the high field test stress management will be verified by comparing strain gauge data and capacitive stress transducer data to expected values. Magnet analysis preparation for this test is complete and results will be published after the conclusion of testing and is not included as part of this dissertation.

6.2 Summary

Stress management is a promising scheme to maximize the current capacity of superconducting cable by limiting the strain induced current degradation. The stress management scheme requires that a block coil geometry incorporate a pier and beam matrix and a laminar spring to mechanically isolate windings. Stress management also requires sheer release with mica paper and hydraulic preloading with pressurized Wood's metal filled bladders to minimize stick-slip motion. Capacitive and resistive transducers were developed, constructed, and calibrated to measure the Lorentz force and verify stress management effectiveness. The magnetics, quench dynamics, and mechanics have been simulated and compared with data from piece parts and other magnets and will ultimately

be compared to TAMU3. Electrical analysis was performed on a failed coil to test its viability and a replacement coil was fabricated.

In conclusion, TAMU3 is an advanced prototype dipole with multiple technological advances that have not been employed in any other dipole. Pursuing this uniqueness along with unforseen difficulty has slowed the completion of the magnet but was necessary to fulfil the charge to the ARL to develop and demonstrate the feasibility of obtaining the highest and most efficient accelerator dipoles possible. To that effect the Accelerator Research Lab with the notes, documentation, collaboration, and technology it leaves behind with TAMU3 has been successful.

REFERENCES

[1] C. Battle, R. Blackburn, N. Diaczenko, T. Elliott, R. Gaedke, W. Henchel, E. Hillt, M. Johnson, H. Kautzky, A. McInturff, J. McIntyre, P. McIntyre, A. Sattarov, R. Benjegerdes, P. Bish, D. Byford, R. Hannaford and A. Lietzke, *Testing of TAMU1: A Single-Aperture Block-Coil Dipole*, presented at the Particle Accelerator Conference, Chicago, IL, (2001).

[2] C. Battle, P. Bish, R. Blackburn, N. Diaczenko, T. Elliott, R. Gaedke, R. Hannaford, W. Henchel, E. Hill, M. Johnson, H. Kautzky, A. Lietzke, A. McInturff, J. McIntyre, P. McIntyre and A. Sattarov, *Testing of TAMU1 Dipole*, Texas A&M University, College Station, TX, p. 11, http://people.physics.tamu.edu/mcintyre/Testing_of_TAMU1_Dipole.pdf, (2001).

[3] A. McInturff, P. Bish, R. Blackburn, N. Diaczenko, T. Elliott, Jr. R. Hafalia, W. Henchel, A. Jaisle, W. Lau, A. Lietzke, P. McIntyre, P. Noyes and A. Sattarov, IEEE Transactions on Applied Superconductivity **17** (2), pp. 1157, (2007).

[4] P. Noyes, R. Blackburn, N. Diaczenko, T. Elliott, W. Henchel, A. Jaisle, A. McInturff, P. McIntyre and A. Sattarov, IEEE Transactions on Applied Superconductivity **16** (2), pp. 391, (2006).

[5] Raymond Blackburn, Tim Elliott, William Henchel, Al McInturff, Peter McIntyre and Akhdior Sattarov, IEEE Transactions on Applied Superconductivity **13** (2), pp. 1355, (2003).

[6] E.F. Holik, C. P. Benson, R. Blackburn, N. Diaczenko, T. Elliott, A. Jaisle, A.D. McInturff, P.M. McIntyre and A. Sattarov, Advances in Cryogenic Engineering **1434**, pp. 649, (2012).

[7] E.F. Holik, A.D. McInturff, C. P. Benson, R. Blackburn, N. Diaczenko, T. Elliott, A. Jaisle, P.M. McIntyre and A. Sattarov, *Current Progress of TAMU3: A Block Coil Stress-Managed High Field (>12T) Nb_3Sn Dipole*, presented at the Particle Accelerator Conference, New York, NY, (2011).

[8] A. McInturff, R. Blackburn, N. Diaczenko, T. Elliott, T. Holik, A. Jaisle, P. McIntyre and A. Sattarov, IEEE Transactions on Applied Superconductivity **21** (3), pp. 1620, (2011).

[9] Steve J. St. Lorant, *Harmony in Science: Superconductivity and High Energy Physics*, SLAC, Stanford, CA, SLAC-PUB-2237, p. 8, (1978).

[10] Martin N. Wilson, *Superconducting Magnets*. (Clarendon Press, Oxford, England, 1983).

[11] Hatch, Mott and MacDonald, *Estimate of Heavy Civil Underground Construction Costs for a Very Large Hadron Collider in Northern Illinois*, C. C. Engineers, Fermi National Accelerator Laboratory, Batavia, IL, p. 199, (2001).

[12] Douglas G. Taskert, James H. Goforth, Dennis H. Herrera, David T. Torres, James C. King and Henn Oona, *High Current, Low Jitter, Explosive Closing Switches*, presented at the Proceedings of the Pulsed Power Conference, Monterey, CA, (2005).

[13] James E. Brau, *The Science and Challenges for Future Detector Development in High Energy Physics*, presented at the SNIC Symposium, Stanford, CA, (2006).

[14] M. Stanley Livingston, *Particle Accelerators: A Brief History*. (Harvard University Press, Cambridge, MA, 1969).

[15] Alexander Chao, Ronald Davidson, Alexander Dragt, Gerald Dugan, Norbert Holtkamp, Chan Joshi, Thomas Roser, Ronald Ruth, John Seeman and Jim Strait, *2001 Snowmass Accelerator R&D Report*, Stanford University, SLAC, Stanford, CA SLAC-PUB-9483, (2001).

[16] Andrew Robert Steere, *A Timeline of Major Particle Acclerators*, Michigan State University, East Lansing, MI, (Thesis, 2005).

[17] Peter McIntyre and A. Sattarov, *On the Feasibility of a Tripler Upgrade for LHC* presented at the Particle Accelerator Conference, Knoxville, TN, (2005).

[18] P. McIntyre and A. Sattarov, *PETAVAC: 100 TeV Proton-Antiproton collider in SSC Tunnel*, presented at the Particle Accelerator Conference, Vancouver, BC, Canada, (2009).

[19] N.V. Mokhov, Y.I. Alexahin, V.V. Kashikhin, S.I. Striganov and A.V. Zlobin, Physical Review Special Topics - Accelerators and Beams **14** (061001), (2011).

[20] N.V. Mokhov, V.V. Kashikhin, I. Novitski and A.V. Zlobin, *Radiation Effects in a Muon Collider Ring and Dipole Magnet Protection*, presented at the Particle Accelerator Conference, New York, NY, (2011).

[21] P. M. McIntyre and A. Sattarov, *Dynamics of Decay Electrons and Synchrotron Radiation in a TeV Muon Collider*, presented at the Particle Accelerator Conference, Chicago, IL, (2011).

[22] Eric Prebys, Giorgio Ambrosio, Rama Calaga, John Fox, Tom Markiewicz, GianLuca Sabbi, Peter Wanderer and Alexander Zlobin, *Strategic Plan for the LHC Accelerator Research Program*, Stanford University, SLAC, Stanford, CA, 21, p. 17, (2012).

[23] Gijs de Rijk, *EuCARD Magnet Development*, presented at the IEEE/CSC & ESAS/ESNF, Paris, France, (2011).

[24] D. R. Read, Cryogenics **18** (10), pp. 579, (1978).

[25] Yen-Huei Hon, Jian-Yih Wang and Yung-Ning Pan, Materials Transactions **44** (11), pp. 2384, (2003).

[26] A. Godeke, P. Acosta, D. Cheng, D.R. Dietderich, M.G.T. Mentink, S.O. Prestemon, G.L. Sabbi, M. Meinesz, S. Hong, Y. Huang, H. Miao and J. Parrell, Superconducting Science and Technology **23** (3), (2010).

[27] Peter J. Lee, in *Excel*, (Applied Supercon Center, Tallahassee, FL, 2013).

[28] E. Hellstrom, P. Chen, N. Craig, M. Dalban-Canassy, J. Jiang, F. Kametani, D. Larbalestier, M. Matras and U. Trociewitz, *Increasing Critical Current Density in Bi-2212 Round Wires by Overpressure Processing*, presented at the CEC-ICMC, Anchorage, AK, (2013).

[29] Joong Byeon, Chris English, Al McInturff, Peter McIntyre and Akhdiyor Sattarov, IEEE Transactions on Applied Superconductivity **18** (2), pp. 513, (2008).

[30] P.M. McIntyre, K. Damborsky, E.F. Holik, F. Lu, A.D. McInturff, N. Pogue, A. Sattarov and E. Sooby, IEEE/CSC & ESAS European Superconductivity News Forum **1** (16), (2011).

[31] A. Nijhuis, Y. Ilyin and W. Abbas, Superconducting Science and Technology **21** (065001), pp. 1, (2008).

[32] J.W. Ekin, IEEE Transactions on Magnetics **13** (1), pp. 127, (1977).

[33] G. Rupp, Cryogenics **18**, pp. 663, (1978).

[34] Bennie ten Haken, Herman H. J. ten Kate and J. Tenbrink, IEEE Transactions on Applied Superconductivity **5** (2), pp. 1298, (1995).

[35] Bennie ten Haken, Arno Godeke, Henk-Jan Schuver and Herman H. J. ten Kate, IEEE Transactions on Magnetics **32** (4), pp. 2720, (1996).

[36] X. F. Lu, N. Cheggour, T. C. Stauffer, C. C. Clickner, L. F. Goodrich, U. Trociewitz, D. Myers and T. G. Holesinger, IEEE Transactions on Applied Superconductivity **21** (3), pp. 3086, (2011).

[37] H.H.J. ten Kate, H. Weijers, S. Wessel, H. Boschman and L.J.M. van de Klundert, IEEE Transactions on Magnetics **28** (1), pp. 715, (1992).

[38] A. Godeke, *Performance Boundaries in Nb_3Sn Superconductors*, University of Twente, The Netherlands, (Thesis, 2005).

[39] S. A. Gourlay, K. Chow, D. R. Dietderich, R. Gupta, R. Hannaford, W. Harnden, A. Lietzke, A. D. Mcinturff, G. A. Millos, L. Morrison, M. Morrison and R. M. Scanlan, *Fabrication and Test Results of a Prototype, Nb_3Sn Superconducting Racetrack Dipole Magnet*, SC MAG 628, Lawrence Berkeley National Lab, Berkeley, CA, LBNL-41575, p. 5, (1998).

[40] N. Diaczenko, T. Elliott, R. Gaedke, A. Jaisle, D. Latypov, P. McIntyre, P. McJunkins, L. Richards, W. Shen, R. Soika and D. Wendt, *Stress Management in High-Field Dipoles*, presented at the Proceedings of the Particle Accelerator Conference, Vancouver, Canada, (1997).

[41] K. Chow, D.R. Dietderich, S.A. Gourlay, R. Gupta, W. Harnden, A. Lietzke, A.D. McInturff, G.Millos, L. Morrison, M. Morrison and R.M. Scanlan, *Design and Fabrication of Racetrack Coil Accelerator Magnets*, presented at the 6th European Particle Accelerator Conference, Stockholm, Sweden, (1998).

[42] Gian Luca Sabbi, IEEE Transactions on Applied Superconductivity **12** (1), pp. 236, (2002).

[43] Pier Paolo Granieri, Clément Lorin and Ezio Todesco, IEEE Transactions on Applied Superconductivity **21** (5), pp. 3555, (2011).

[44] A.F. Lietzke, R. Benjegerdes, S. Caspi, D. Dell'Orco, W. Harnden, A.D. McInturff, M. Morrison, R. M. Scanlan, C.E. Taylor and J.M. van Oort, IEEE Transactions on Applied Superconductivity **7** (2), pp. 739, (1997).

[45] L. Chiesa, S. Caspi, M. Coccoli, D.R. Dietderich, P. Ferracin, S.A. Gourlay, R.R. Hafalia, A.F. Lietzke, A.D. Mcinturff, G. Sabbi and R.M. Scanlan, IEEE Transactions on Applied Superconductivity **13** (2), pp. 1254, (2003).

[46] A. F. Lietzke, S. E. Bartlett, P. Bish, S. Caspi, D. Dietderich, P. Ferracin, S. A. Gourlay, A. R. Hafalia, C. R. Hannaford, H. Higley, W. Lau, N. Liggins, S. Mattafirri, M. Nyman, G. Sabbi, R. Scanlan and J. Swanson, IEEE Transactions on Applied Superconductivity **15** (2), pp. 1123, (2005).

[47] A. F. Lietzke, S. Bartlett, P. Bish, S. Caspi, L. Chiesa, D. Dietderich, P. Ferracin, S. A. Gourlay, M. Goli, R. R. Hafalia, H. Higley, R. Hannaford, W. Lau, N. Liggens, S. Mattafirri, A. McInturff, M. Nyman, G. Sabbi, R. Scanlan and J. Swanson, IEEE Transactions on Applied Superconductivity **14** (2), pp. 345, (2004).

[48] Paolo Ferracin, Scott E. Bartlett, Shlomo Caspi, Daniel R. Dietderich, Steve A. Gourlay, Carles R. Hannaford, Aurelio R. Hafalia, Alan F. Lietzke, Sara Mattafirri and Gianluca Sabbi, IEEE Transactions on Applied Superconductivity **15** (2), pp. 1119, (2005).

[49] Bolton Metal Products, *Specifications* (Bellefonte, PA, 2013), Vol. 2013, Physical properties of Cerrolow-147.

[50] Shlomo Caspi, Steve Gourlay, Ray Hafalia, Alan Lietzke, Jim ONeill, Clyde Taylor and Alan Jackson, IEEE Transactions on Applied Superconductivity **11** (1), pp. 2272, (2001).

[51] Yu. A. Kiselev and A. V. Nazarenko, Izmeritel'naya Tekhnika (12), pp. 43, (1983).

[52] C.L. Goodzeit, M.D. Anerella and G.L. Ganetis, IEEE Transactions on Magnetics **25** (2), pp. 1463, (1989).

[53] J. P. Ozelis, *Capacitance Strain Gauges - an Introduction and Modest Proposal*, Fermilab, Batavia, IL, TS-96-020, p. 4, (1996).

[54] N.Siegel, D.Tommasini and I.Vanenkov, *Design and Use of Capacitive Force Transducers for Superconducting Magnet Models for the LHC*, CERN, Geneva, Switzerland, p. 5, (1998).

[55] P. Bauer, N. Andreev, D. Chichili, K. Ewald, J. Ozelis and I. Novitski, *Test Fixture and Test Preparation for Mechanical Ten-Stack Measurements for the Common Coil Dipole model magnet*, Fermilab, Batavia, IL, TD-00-040, p. 8, (2000).

[56] J.S. Xia, L. Yin, E.D. Adams and N.S. Sullivan, *A Compact Capacitive Pressure Transducer*, presented at the 25th International Conference on Low Tmperature Physics, Amsterdam, The Netherlands, (2009).

[57] C. P. Benson, E. F. Holik, A. Jaisle, A. D. McInturff and P. M. McIntyre, Advances in Cryogenic Engineering **1434**, pp. 1337, (2012).

[58] Robert Blake Ragland, *Capacitive Stress Gauges in Model Dipole Magnets*, Texas A&M, College Station, TX, (Thesis, 2009).

[59] Christopher Pete Benson, *Capacitive Stress Transducers in Model Dipole Magnets*, Texas A&M, College Station, TX, (Thesis, 2010).

[60] Raymond Blackburn, David Fecko, Andrew Jaisle, Al McInturff, Peter McIntyre and Tom Story, IEEE Transactions on Applied Superconductivity **18** (2), pp. 1391, (2008).

[61] D. Bocian, G. Ambrosio and G. M. Whitson, AIP Conference Proceedings **1435** (1), pp. 193, (2012).

[62] Damir Latypov, Peter McIntyre and Weijun Shen, *Quench simulation for 16T dipole built at Texas A&M University* presented at the Proceedings of the Particle Accelerator Conference, Vancouver, BC, Canada, (1997).

[63] A. McInturff, *QUCERN*. (CERN, Geneva, Switzerland, 1989).

[64] A.V. Zlobin, I. Novitski and R. Yamada, *Quench Protection Analysis of a Single-Aperture 11T Nb_3Sn Demonstrator Dipole for LHC Upgrades*, presented at the International Particle Accelerator Conference, New Orleans, LA, (2012).

[65] L. Imbasciati, G. Ambrosio, P. Bauer, V. Kashikin, S.W. Kim and A.V. Zlobin, *Quench Protection Study of the Single Layer Common Coil Dipole Magnet*, Fermilab National Accelerator Laboratory, Batavia, IL, TD-00-057, p. 14, (2000).

[66] Giulio Manfreda, *Review of ROXIE's Material Properties Database for Quench Simulation*, CERN, TE Technology Department, Geneva, Switzerland (2011).

[67] K. Melconian, K. Damborsky, N. Glasser, E. Holik, J. Kellams, P. McIntyre, N. Pogue and A. Sattarov, Advances in Cryogenic Engineering **1573**, pp. 739, (2014).

[68] J.E. Jensen, W.A. Tuttle, R.B. Stewart, H. Brechna and A.G. Prodel, *Selected Cryogenic Data Notebook*, Brookhaven National Laboratory, Brookhaven, NY, BNL 10200-R, (1980).

[69] Yukikazu Iwasa, *Case Studies in Superconducting Magnets; Design and Operational Issues*, 2nd ed. (Springer, Cambridge, MA, 2009).

[70] Anil K. Sinha and John J. Moore, Metallography **19**, pp. 87, (1986).

[71] Anil K. Sinha, Metallography **20**, pp. 37, (1987).

[72] Special Metals, *Inconel Alloy X-750*, Special Metals Corporation, Huntington, WV, SMC-067, p. 28, (2004).

[73] Composite Technology Development Inc., *CTD-101K Epoxy Resin System Datasheet*, Lafayette, CO, http://www.ctd-materials.com/papers, p. 3, (2003).

[74] E.F. Holik, R. Garrison, N. Diaczenko, T. Elliott, A. Jaisle, A.D. McInturff, P. McIntyre and A. Sattarov, Advances in Cryogenic Engineering **1573**, pp. 1535, (2014).

[75] N. Andreev, E. Barzi, D.R. Chichili, S. Mattafirri and A.V. Zlobin, Advances in Cryogenic Engineering **48**, pp. 941, (2002).

[76] N. Mitchell, Cryogenics **45**, pp. 501, (2005).

[77] D.R. Dietderich, J.R. Litty and R.M. Scanlan, Advances in Cryogenic Engineering **44** (B), pp. 1013, (1997).

[78] Dustin M. McRae and Robert P. Walsh, IEEE Transactions on Applied Superconductivity **23** (3), (2013).

[79] Special Metals, *Inconel Alloy 718*, Special Metals Corporation, Huntington, WV, SMC-045, p. 28, (2007).

[80] G. Pottlacher, H. Hosaeus, E. Kaschnitz and A. Seifter, Scandinavian Journal of Metallurgy **31**, pp. 161, (2002).

[81] Peter Hidnert, Journal of Research of the National Bureau of Standards **30**, pp. 101, (1943).

[82] J.E. Daw, J.L. Rempe, D.L. Knudson and J.C. Crepeau, Journal of Nuclear Materials **376** (2), pp. 211, (2008).

[83] Touloukian Y.S., Kirby R.K., Taylor R.E. and Desai P.D., *Thermophysical Properties of Matter: Metallic Elements and Alloys*. (Plenum Publishing Company, Purdue University, Lafayette, IN, 1975).

[84] Christian Scheuerlein, Marco Di Michiel, Gonzalo Arnau Izquierdo and Florin Buta, IEEE Transactions on Applied Superconductivity **18** (4), pp. 1754, (2008).

[85] Jyri Outinen and Pentti Mäkeläinen, Fire and Materials Special Issue: Structures in Fires **28** (2-4), pp. 237, (2004).

[86] S. V. Verkhoturov, M. J. Eller, R. D. Rickman, S. Della-Negra and E. A. Schweikert, Journal of Physical Chemistry C **114** (12), pp. 5637, (2010).

[87] M.D. Abramoff, Magalhaes, P.J., Ram, S.J., Biophotonics International **11** (7), pp. 36, (2004).

[88] D.R. Dietderich, J. Glazer, C. Lea, W.V. Hassenzahl and J.W. Morris, Jr., IEEE Transactions on Magnetics **21** (2), pp. 297, (1985).

[89] R. Taillard and C. Verwaerde, *Phase Transformations During the Manufacturing Process of Nb_3Sn Superconducting Composites*, presented at the Euromat 95, Venice, Italy, (1995).

[90] Michael Naus, *Optimization of Internal-Sn Nb_3Sn Composits*, University of Wisconsin, Madison, WI, (Thesis, 2002).

[91] D.R. Dietderich, A. Godeke, N.L. Liggins and H.C. Higley, *Development of High Current Nb_3Sn Rutherford Cables for NED and LARP*, presented at the Workshop on Accelerator Magnet, Superconductor, Design and Optimization (WAMSDO), Zurich, Switzerland, (2008).

[92] Vishay Micro-Measurements, *Strain Gage Installations with M-Bond 43-B, 600, and 610 Adhesive Systems*, Malvern, PA, http://www.intertechnology.com/Vishay/pdfs/Instruction_Bulletins/B-130-15.pdf, p. 4, (2013).

[93] L. Bottura, L. Walckiers and R. Wolf, IEEE Transactions on Applied Superconductivity **7** (2), pp. 602, (1997).

[94] G. Ambrosio, P. Bauer, L. Bottura, M. Haverkamp, T. Pieloni, S. Sanfilippo and G. Velev, IEEE Transactions on Applied Superconductivity **15** (2), pp. 1217, (2005).

[95] Walter F. Henning, *The Future GSI Facility: Beams of Ions and Antiprotons*, presented at the Particle Acclerator Conference, Portland, OR, (2003).

[96] Bogdanov I., Chirkov P., Keilin V., Kozub S., Shcherbakov P., Slabodchikov P., Sytnik V., Tkachenko L., Zintchenko S. and Zubko V., *Design of 6T Superconducting Dipoles for the SIS 300*, B. Stavissky, Moscow, Russia, (2003).

[97] G. Moritz, *Fast-Pulsed SC Magnets*, presented at the Proceedings of EPAC 2004, Lucerne, Switzerland, (2004).

[98] Markus Haverkamp, *Decay and Snapback in Superconducting Accelerator Magnets*, University of Twente, The Netherlands, (Thesis, 2003).

[99] L. Bottura, T. Pieloni, S. Sanfilippo, G. Ambrosio, P. Bauer and M. Haverkamp, *A Scaling Law for Predicting Snap-Back in Superconducting Accelerator Magnets*, presented at the European Partical Accelerator Conference, Lucerne, Switzerland, (2004).

[100] A. McInturff, P. M. McIntyre and A. Sattarov, *Rapid-Cycling Dipole Using Block-Coil Geometry and Bronze-Process Nb_3Sn Superconductor*, presented at the Particle Accelerator Conference, Albuquerque, NM, (2007).

[101] Arjan Peter Verweij, *Electrodynamics of Superconducting Cables in Accelerator Magnets*, University of Twente, The Netherlands, (Thesis, 1995).

[102] E.M.J. Niessen, *Continuum Electromagnetics of Composite Superconductors*, University of Twente, The Netherlands, (Thesis, 1993).

[103] G. H. Morgan, Journal of Applied Physics **41** (9), pp. 3673, (1970).

[104] Arup K. Ghosh, Eric Gregory and Xuan Peng, IEEE Transactions on Applied Superconductivity **21** (3), pp. 2380, (2011).

[105] YinShun Wang, Xiao Li, Chi Xue and LianQi Zhao, Sci. China Technol. Sci. **55** (7), (2012).

[106] B. Bordini, D. Richter, P. Alknes, A. Ballarino, L. Bottura and L. Oberli, IEEE Transactions on Applied Superconductivity **23** (3), (2013).

[107] Leszek R. Motowidlo, Emanuela Barzi, Daniele Turrioni, Najib Cheggour and Loren F. Goodrich, IEEE Transactions on Applied Superconductivity **19** (3), pp. 2598, (2009).

[108] M. N. Wilson, A. K. Ghosh, B. ten Haken, W. V. Hassenzahl, J. Kaugerts, G. Moritz, C. Muehle, A. den Ouden, R. Soika, P. Wanderer and W. A. J. Wessel, IEEE Transactions on Applied Superconductivity **13** (2), pp. 1704, (2003).

[109] M. N. Wilson, *Review of Cable Loss Formulae*, GSI Fast–Pulsed Synchrotron Project, Cambridge, England, (2004).

[110] Emanuela Barzi, Michela Fratini, Hugh C. Higley, Ron M. Scanlan, Ryuji Yamada and Alexander V. Zlobin, IEEE Transactions on Applied Superconductivity **11** (1), pp. 2134, (2001).

[111] P. Bauer, G. Ambrosio, N. Andreev, E. Barzi, D. Dietderich, K. Ewald, M. Fratini, A.K. Ghosh, H.C. Higley, S.W. Kim, G. Miller, J. Miller, J. Ozelis and R.M. Scanlan, IEEE Transactions on Applied Superconductivity **11** (1), pp. 2457, (2001).

[112] Luca Bottura, Gijs de Rijk, Lucio Rossi and Ezio Todesco, IEEE Transactions on Applied Superconductivity **22** (3), (2012).

[113] Mark Glajchen, to E. Holik, Recommended Heat Treatment Schedule, (Oxford Superconducting Technology, Carteret, NJ, 2012).

[114] R. Bossert, D. Chichili, S. Feher, T. Heger, J. Kerby, A. Nobrega, I. Novitski, J. P. Ozelis and A. V. Zlobin, IEEE Transactions on Applied Superconductivity **9** (2), pp. 459, (1999).

[115] E. Barzi, G. Ambrosio, N. Andreev, R. Bossert, R. Carcagno, S. Feher, V.S. Kashikhin, V.V.Kashikhin, M.J. Lamm, F. Nobrega, I. Novitski, Y. Pishalnikov, C. Sylvester, M. Tartaglia, D.Turrioni, R. Yamada, A.V. Zlobin, M. Field, S. Hong, J. Parrell and Y. Zhang, IEEE Transactions on Applied Superconductivity **17**, pp. 2718, (2007).

[116] A.R. Hafalia, S.E. Bartlett, S. Caspi, L. Chiesa, D.R. Dietderich, P. Ferracin, M. Goli, S.A. Gourlay, C.R. Hannaford, H. Higley, A.F. Lietzke, N. Liggins, S. Mattafirri, A.D. McInturff, M. Nyman, G.L. Sabbi, R.M. Scanlan and J. Swanson, IEEE Transactions on Applied Superconductivity **14** (2), pp. 283, (2003).

[117] S. Mattafirri, S. E. Bartlett, P. A. Bish, S. Caspi, D. R. Dietderich, P. Ferracin, S. A. Gourlay, C. R. Hannaford, A. R. Hafalia, W. G. Lau, A. F. Lietzke, A. D. McInturff, M. Nyman, G. L. Sabbi and R. M. Scanlan, IEEE Transactions on Applied Superconductivity **15** (2), pp. 1156, (2005).

[118] P. Ferracin, S. Caspi, D. W. Cheng, D. R. Dietderich, A. R. Hafalia, C. R. Hannaford, H. Higley, A. F. Lietzke, J. Lizarazo, A. D. McInturff and G. Sabbi, IEEE Transactions on Applied Superconductivity **18** (2), pp. 277, (2008).

[119] A. K. Ghosh, L. D. Cooley, J. A. Parrell, M. B. Field, Y. Zhang and S. Hong, IEEE Transactions on Applied Superconductivity **17** (2), pp. 2623, (2007).

[120] P. He, Z. M. Chen, W. G. Chen and Y. F. Tan, IEEE Transactions on Applied Superconductivity **20** (6), pp. 2397, (2010).

APPENDIX A: SPLICING PROCEDURES

This procedure in final form represents over four months of development from a tooling to testing prospective. The bulk of the procedure deals with construction of components and setup. At the end of each splice a summary was made and appended to this procedure. Finally a preliminary inter-coil splice procedure is included.

Page

A. Kapton Production Procedure

1. Cut out rectangles of 0.003” Kapton of dimension determined by the Splice Kapton Cutting Form. Place two sheets of Kapton film over the top of the aluminum Kapton die.
2. Arrange the Kapton sheets and press slightly into the die as in Figure 100.

Figure 100: Kapton Die Form

3. Use the top half of the die set to flatten the edges of the Kapton. This fosters symmetric setting of the Kapton during coining.
4. Now symmetrically and slowly place the top of the die set in the Kapton wedge and press into place. For repeatability always orient the die set with the chamfered edge matching.

Figure 101: Kapton Former and Softening Furnace

5. Hand-tighten bolts to no more than roughly 30 inch-pounds.
6. Place in Furnace at 200°C for at least an hour as shown in Figure 101. And let cool for at least 2 hours or until the die set is below 40°C. Prematurely removing the die out of the furnace or out of the die set will result in the Kapton not taking a full

set. There is no benefit to going to 250°C because it will take longer to cool and 150°C doesn't anneal the Kapton enough.

7. After the die set cools, remove the bolts and the top of the die set. The top should be easy to remove by hand without using the jacking threads.
8. Now the top of the die set can be utilized to remove the coined Kapton piece. Slide the top of the die set from one edge to the other, thus sliding out the coined Kapton as shown in Figure 102.
9. Leave the two pieces of Kapton pressed together and store in the red storage box. They will be removed from each other when they are needed for splicing. If the coined Kapton is uneven, it may have to be trimmed with scissors or the paper cutter to fit into the splice block groove.

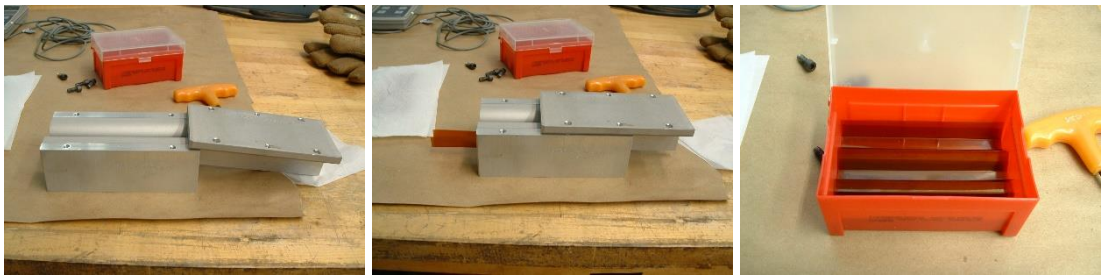

Figure 102: Kapton Removal and Storage

B. Solder Production Procedure

1. Calculate and cut the amount of solder needed for the joint. See the Solder Calculation section for more details. Add 10% to the ideal amount. For TAMU3b joints, 4.0" and 3.6" of 1/8" flux free Sn60 Solder is needed for the Inner and Outer joints respectively.

NOTE: The inner (outer) 4.0" (3.6") of solder was split so that 2.5" (2.1") was touching the Nb_3Sn piece and 1.5" (1.5") was touching the copper cans.

2. Place the solder wires on the ground tool steel dies. The direction of the surface texture from grinding the tool steel effects the amount of compression of the solder wire. Use the same solder orientation as in Figure 103.

3. Compress the solder in the center of the large press until the 1/8” solder wire is flattened to 0.041” thick. This puts the width of the ribbon to 0.300” wide so it can comfortably fit in the 0.330” wide aluminum solder rollers. This is accomplished by compressing to about 2400 lbs / inch of solder for about ~45 seconds. Both time and pressure affect the amount the solder compresses (1 minute is too long and 30 seconds isn’t long enough.) In Figure 103 there was 11.6” of Solder for a total dial pressure of 420.5 psi (recall that the cylinder area is 66.3 square inches.) Remember to zero the dial from the platen weight.

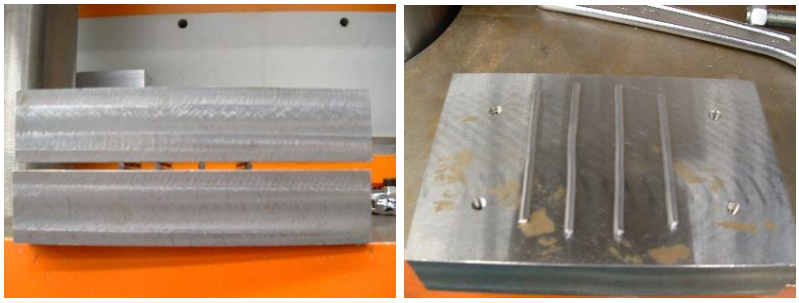

Figure 103: Solder Flattening Orientation

4. Use the aluminum solder rollers to flatten the solder tapes to ~0.015” thick. It should take about 2 passes through the rollers. Measure the roller spacing as shown in Figure 104. Note that the ruler part of the calliper is resting on the rods and that the rods were being measured on the top gap part of the calliper and not on the ground surface. This assures a square and repeatable measurement. Set both sides to 3.612”. An error of only a 0.0015 will cause the solder tape to taper and curl.

Figure 104: Flattened Solder and Die Measurement

5. Roll the pieces until they are tactfully less than 15 inches (3.75” x 4). This is accomplished by setting the handle side of the roller to 3.6045” and the back side to 3.6060” as previously measured and rolling the inner 3 times and the outer 5 times as shown in Figure 105.
6. Cut the ribbons into 4 equal lengths and place back on the ground tool steel die. Press the ribbons to at least 500 psi to remove the edge curl from the aluminum rollers.
7. This procedure should produce ~0.350” wide and 0.007” and 0.008” thick ribbons for the respective outer and inner splice joints.

Figure 105: Solder Die Measurement and Orientation

C. Copper Can Production Procedure

1. EDM 0.032” Cu rectangles for the cover (.525” by 3.75”) and the can (1.297” by 3.75”). The width of the can rectangle is determined by the die slot width (1.3”).

Figure 106: Copper Can Anneal Setup

2. Anneal the Copper in Argon at 600C for at least 10 minutes before the first forming to soften the Cu as shown in Figure 106.

Figure 107: Copper Can Former Operation

3. Form the can in the punch and die using the arbor press (near the CNC mill under the crane). The punch and die can be separated using the wooden fixture and the rubber pad as shown in Figure 107. The copper piece can be removed from the punch by hand. Repeat steps 2 and 3 for the copper cans. This will allow the bottom of the can to be square and flat for proper cable seating and dimensioning during the splice.

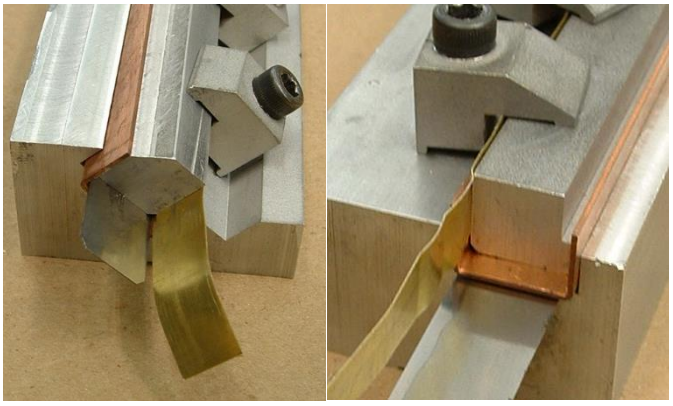

Figure 108: Tall Copper Can Machining Orientation

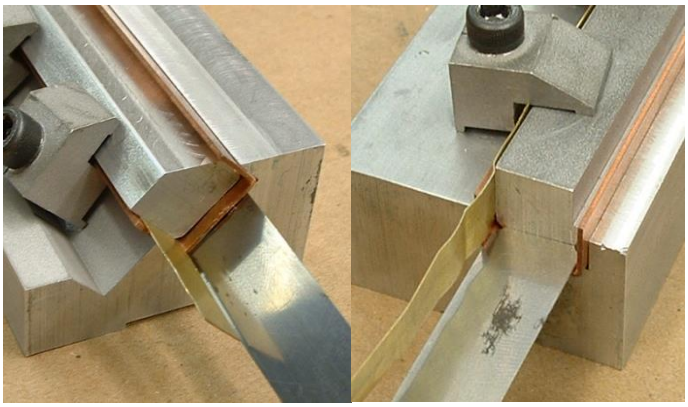

Figure 109: Short Copper Can Machining Orientation

4. Machine the square and angled edges of the formed cans using the two aluminum fixtures.
    a. The inner cable can is 0.230” tall and the outer can is 0.222” tall. Machining both pieces in the same fixture is accomplished with an 0.008” shim.
        i. Place the shim below the copper ‘C’ for the outer can as shown in Figure 108.
        ii. Place the shim above the copper ‘C’ for the inner can as shown in Figure 109.
        iii. The brass shim compensates for the can size modifications.
    b. Be careful not to remove material from the aluminum fixture but come in close contact with the aluminum. Close contact is important to remain within tolerance and for proper copper support. Remember the copper is dead soft.
    c. The best results are accomplished with the cutting edge rotating away from the center of the can on the 90° edge and toward the center of the can on the 45° edge. This makes the burrs on the outer side for the 90° edge and allows the aluminum fixture to better support the dead soft copper. See Figure 110 for the bit orientation.
5. Completely de-burr all edges. Pay special attention to the inner edges so that the can cover can easily slide into the ‘C’ and center itself if slightly out of alignment during the actual splice.

6. Re-anneal the copper cans. This final anneal removes any internal stress to foster the highest RRR for the copper. For test pieces this step isn't necessary.
7. For good measure, scuff the internal sides of the copper cans and covers with a green scotch-bright pad to remove the oxide layer. Clean any particulates on the copper thoroughly with soap and then with alcohol.

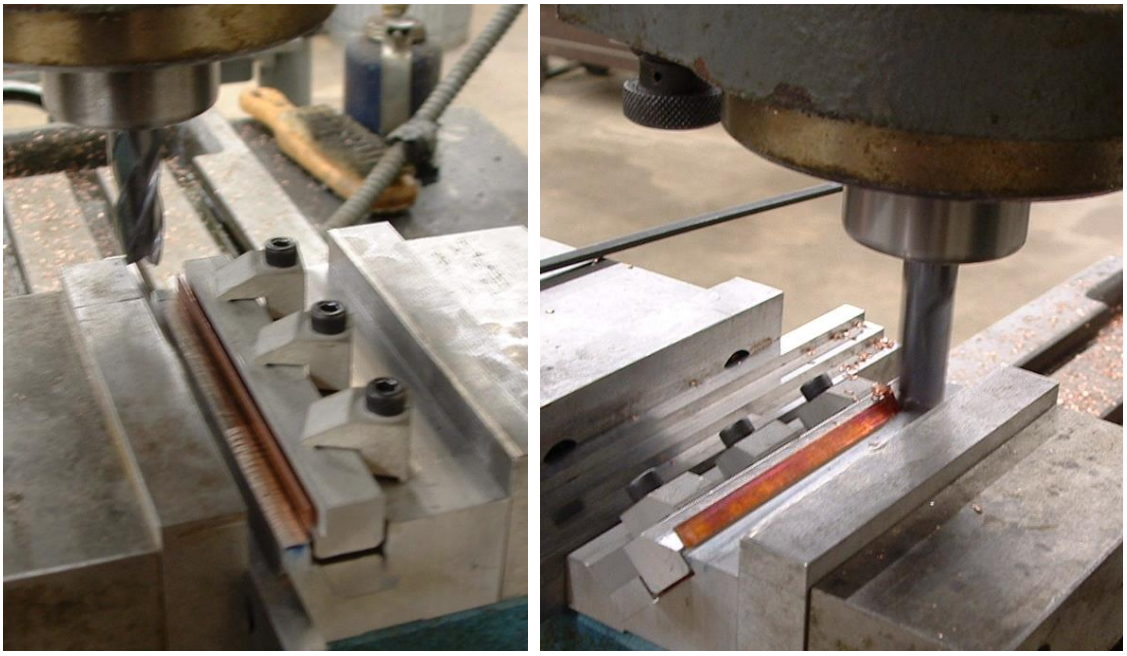

Figure 110: Copper Can Cutter Orientation

D. Inner Splice Setup

1. Complete the Solder Production Procedure, the Kapton Production Procedure, and the Copper Can Production Procedures. All splice parts are kept together in the splicing box.

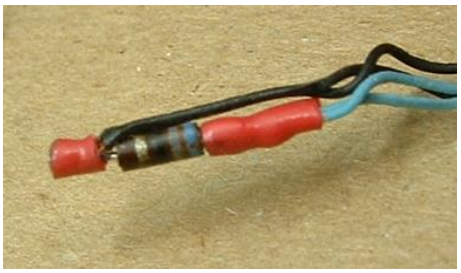

Figure 111: Splicing Carbon Resistor

2. Prepare two carbon resistor assemblies and voltage taps.
    a. Document the marked resistance. Also document the measured resistance before and after soldering.
    b. Use 4 leads of the 32 AWG, double Formvar insulated and PVC coated, manganin wire. Use > 2’ of leader for each wire as in Figure 111.

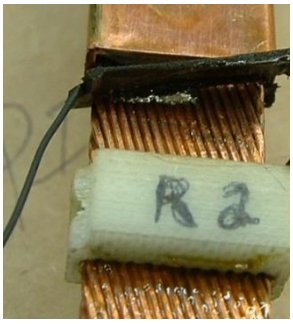

Figure 112: Transition Gaping Element Orientation

    c. Pre-tin each wire and resistor lead to aid assembly. Also pre-tin ½” of a wire for the magnet side voltage tap to be soldered in place during the actual splice joint as indicated in Figure 112.

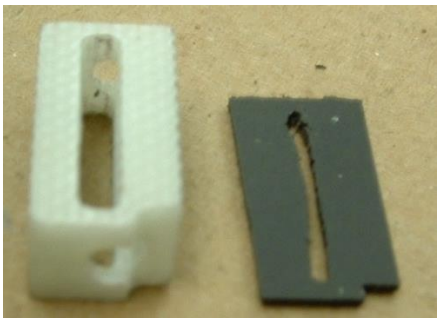

Figure 113: Transition Gaping Element and Rubberized Gasket

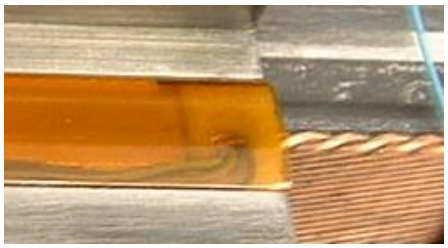

Figure 114: Voltage Tap and Carbon Resistor Leads

d. Use heat shrink tubing to insulate the wires from the Rutherford cable.

3. Prepare the appropriate G-7 Gapping elements and associated components.
    a. The existing holes are 5/64". Carefully redrill the hole with a 32 drill bit as in Figure 113. Then use a needle file to shape the hole so that the carbon resistor assembly fits with little resistance with Nb_3Sn cable in place so that it can fit as in Figure 114.
    b. Use a razor and cut out a solder gasket out of the rubber foam sheet. The gasket should be the same cross section as the G-7 gapping element with a simple slit for the cable as shown in Figure 113.

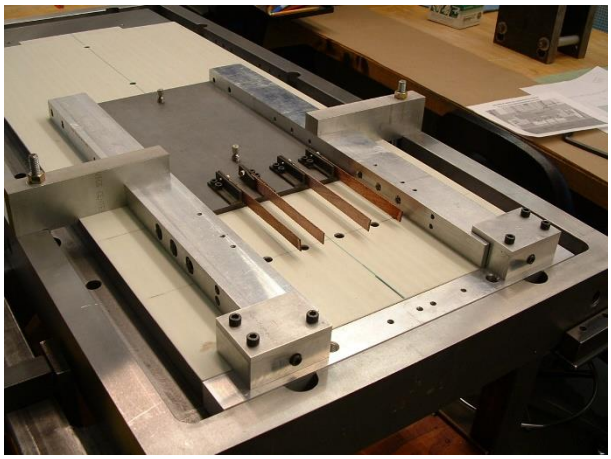

Figure 115: Splice Test Fixturing

4. Scuff the NbTi cable with a green scotch-bright and clean with isopropanol. Clean all other splice components ultrasonically if necessary and then with isopropanol.

5. Assemble all of the support structure parts on the coffin base as indicated in Figure 115 and Figure 116.
    a. Make sure that the side clamps are in intimate contact with the coffin moat as in Figure 117. Failure to do so will result in the aluminum side bars shifting while tightening the splice blocks.
    b. Do not adjust or loosen the cable clamps. They are currently adjusted for the location of the cable in TAMU3.
    c. **Support and protect the exposed cable at all times.** Both for joint testing and practice for splicing actual magnet.

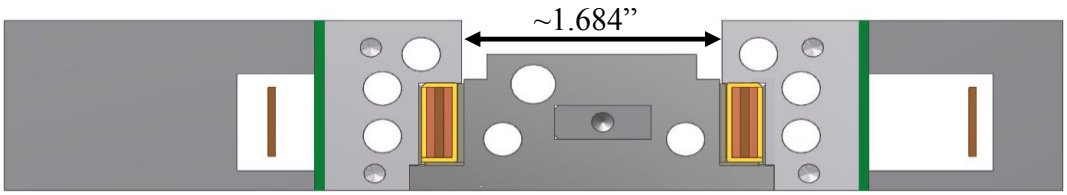

Figure 116: Cross Section of Inner Coil Splicing

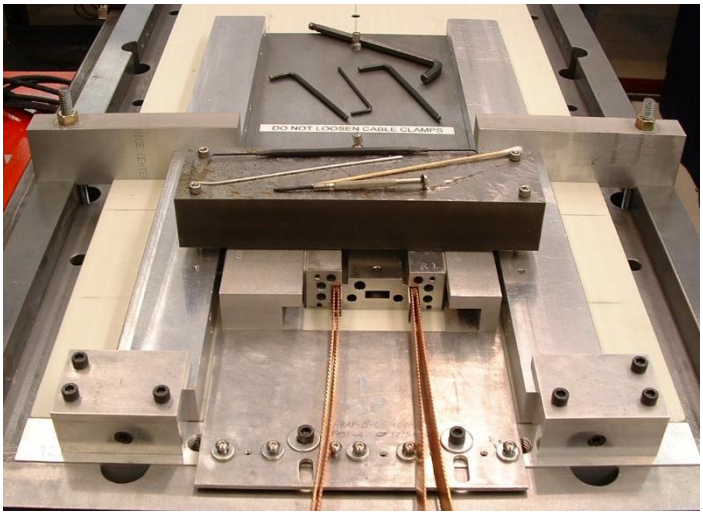

Figure 117: Inner Test Splice Setup

6. Assemble an inner splice as shown in Figure 118 without flux or solder.
    a. First tighten the four bolts of the top flattening beam to roughly 5 inch-pounds. Just enough to keep the heater blocks square.

b. Then tighten the six side loading bolts to roughly 50 inch-pounds.
    i. Use whatever fine tip tools necessary to make the elements level and square with the copper can. Make sure the tools don't damage the cable or dent the copper cans.
    ii. Make sure that the splice and heater blocks are square with the magnet base and that the magnet bore hole on the center splice block is on center of the cable holder.

7. Measure the distance between the aluminum heater blocks as indicated in Figure 116. This measurement is the target dimension to compress the cable to during the actual test. The first test measured 1.684 inches.

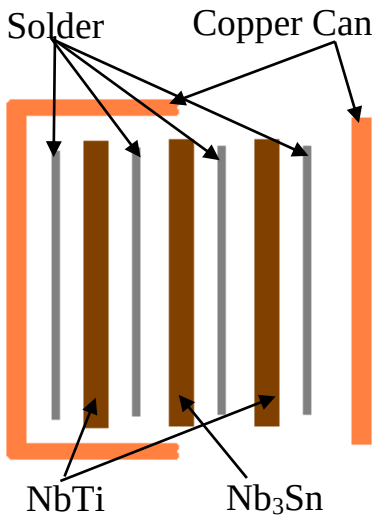

Figure 118: Splice Assembly Schematic

8. Assemble an inner splice as in step 6 with flux and solder.
    a. Only use a Q-tip or toothbrush to clean or apply flux. Using a finger, towel, Kim wipe, or rag has a high probability of damaging the leads.
    b. Place all of the tapered ends of the solder strips towards the magnet side of the joint. This assists the excess solder to flush through the front of the joint rather than between the joint and the magnet.

c. Use the NoKorode® flux as found with the splice kit. Make sure every surface inside the joint is coated (solder strips, inside copper can, and cable). Try to keep the flux off of surfaces outside the joint (shims, backing spacers, outside copper can, and splice and heating blocks. Only use an amount that is necessary for a thin meniscus of flux on each surface. The flux should have little to no thickness on the surfaces.

Figure 119: Placeholder for Carbon Resistor

d. Make sure the solder strips remain centered on the cable. Be patient with the alignment. Preparation is the most crucial component for a successful joint.
e. Place a non-metallic rod of similar diameter as that of the carbon resistor assembly as a temporary spacer that can easily be removed as shown in Figure 119. It should be non-metallic so that if solder comes in contact it will not tin itself.
f. The measurement as indicated in Figure 116 should be approximately 1.76 inches.
g. Place voltage tape wires in joint.

9. Familiarize yourself with the splice cart equipment and verify that each thermocouple and heating element is operational and that the copper cooling system is functioning without leaks. Make the temperature controller set point to

320°F. This brings the cable temperature to roughly 380°F which is 10°F higher than the 60/40 solder melting point.

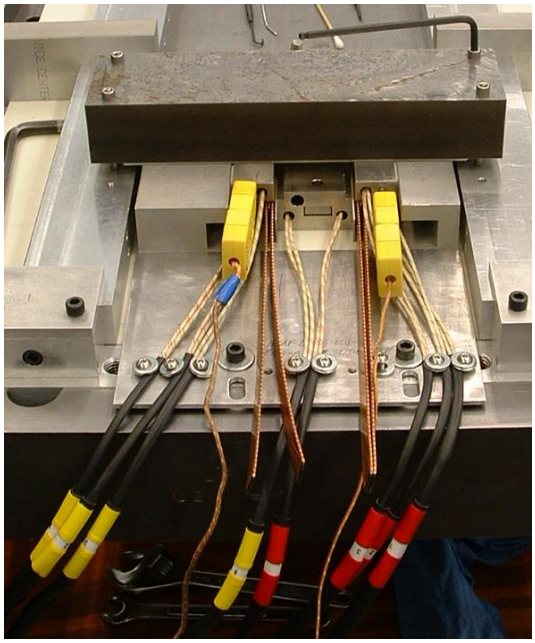

Figure 120: Cartridge Heaters for Inner Test Splice

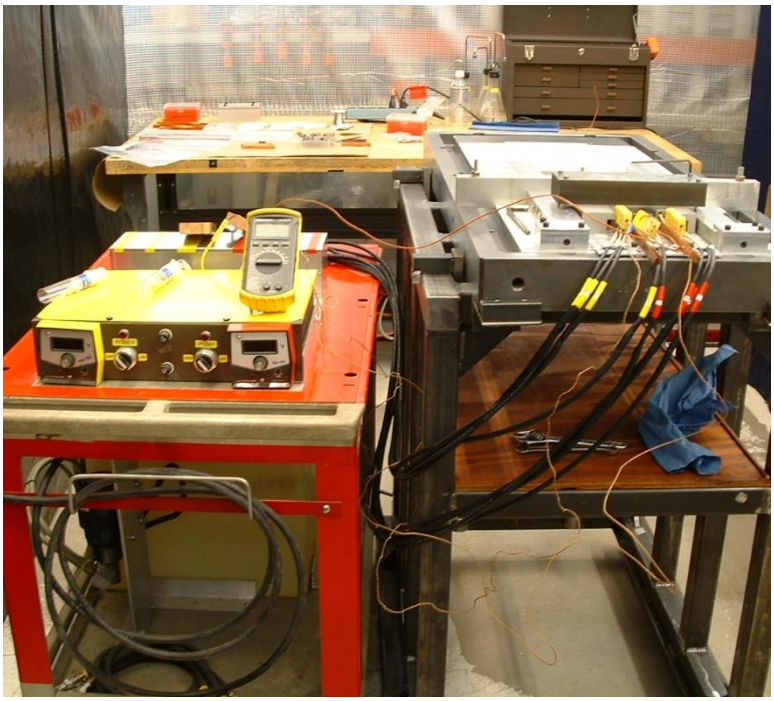

Figure 121: Equipment Schematic for Splice Test

10. Connect all thermocouples and heating elements as shown in Figure 120 and Figure 121.

E. Inner Splice

1. Collect 2 separate 5/16” Allen wrenches to simultaneously tighten both sides of the splice. **Support and protect the exposed Nb_3Sn cable at all times.**

Figure 122: Splice Block Temperature Controllers

2. Turn on the heating controllers and make sure the set point is at 320°F as indicated in Figure 122.
    a. Keep slight pressure on the side bolts so that when the solder begins to melt the copper can remains aligned.
    b. It takes roughly 3 minutes for the solder to melt.
3. Uniformly and simultaneously keep roughly 50 inch-pounds of torque on all 6 side bolts.
    a. It takes about 20 seconds for all of the solder to melt.
    b. Make sure the copper can cover is aligned and adjust if necessary.
    c. Use the fine strand copper wire to wick away excess solder.
    d. Keep tightening the side bolts until it stops compressing and you are within 0.002” of the measurement taken without solder (1.684” to 1.686”).

4. Turn off power to the temperature controllers and place a heavily dampened blue paper towel.
    a. Make sure the towel will not leave puddles of water under the splice blocks.
    b. This will remove more heat initially in comparison to the copper blocks as shown in Figure 123.

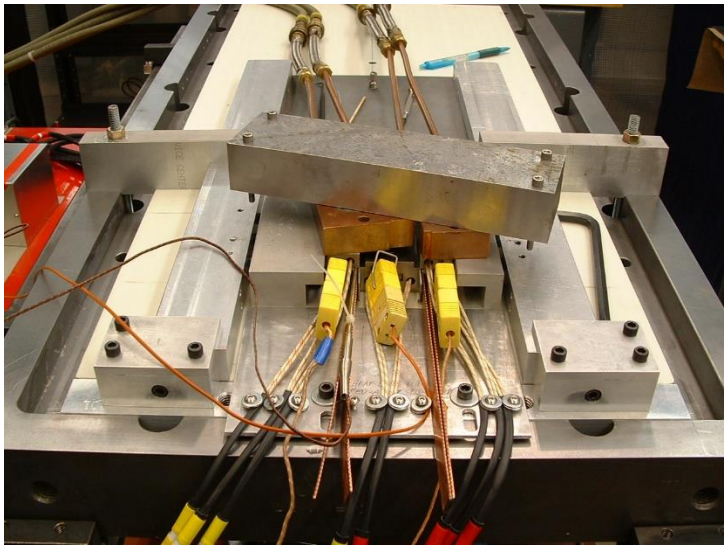

Figure 123: Post Splice Cooling Setup

5. Once the solder is solidified, remove the top flattening beam and the damp paper towel and replace with the copper blocks. Place the top flattening beam over the copper blocks to help hold them down.
6. After the blocks are below 100°F the joint is complete and you may remove all thermocouples and heating elements and loosen the 6 side bolts. **Support and protect the cable at all times.**

F. Outer Splice Setup

1. Repeat the Inner Splice Setup Procedure with the following differences shown in Figure 124 and Figure 125.

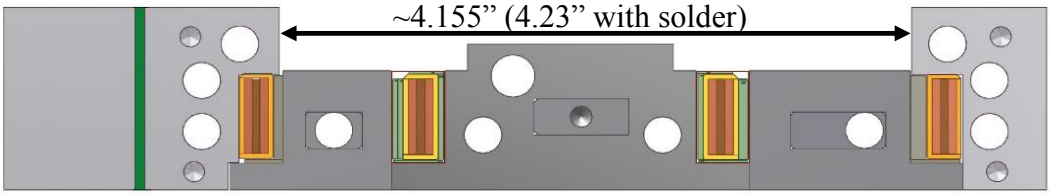

Figure 124: Outer Splice Cross Section

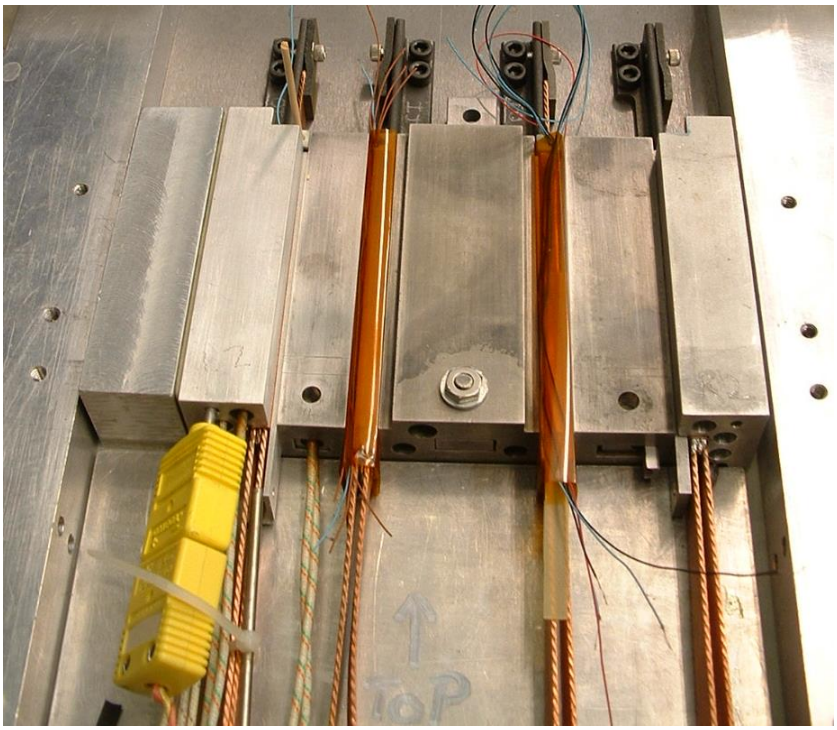

Figure 125: Post Splice Insulation Setup

G. Outer Splice

The Outer splice procedure is the same as the inner splice procedure accept the target dimension is 4.155 inches.

H. Post Splice Procedure

1. Continue to take every precaution to protect the leads from bending. Even with the splice blocks in place the leads can still be bent upwards!!

1. Clean up the leads.
    a. Remove any pooled solder from the front of each lead using the soldering iron.
    b. Remove any pooled flux from each lead and adjacent splice blocks.
        i. **Extreme care must be taken to protect the leads from being bent.**
        ii. Remove with a soldering iron or a small file any protruding solder from body length edges of each joint.
2. Install Pre-Impregnation package.
    a. Install shim package.
        i. See the splicing conclusions for shim sizing.
        ii. Shims should be snug. Not immovable and not loose.
    b. Install electrical components
        i. Install and verify voltage taps
            1. Nb_3Sn cable voltage tap on the magnet side of the joint.
            2. NbTi cable voltage tap on the lead side of the joint.
            3. Twist these leads from each joint.
        ii. Install and verify carbon resistors
            1. Twist a wire pair for measuring voltage and a pair for current supply
            2. Then twist the two pairs of wire together for the four lead resistance measurement
            3. The resistance should be on the order of 54 Ω.
3. Completely install the splice block components
    a. Install the outer blocks and all reference rods.
    b. Install the splice block covers and the tapered dowel pins.

I. Solder Calculation

INNER					Caliper measured	
Pitch Length	91	mm	3.5827	in	88.8	mm
# strands	30					
Pitch Angle	13.45	degrees	(as calculated from cable width)		14.39	degrees
Pitch Angle	15.39	degrees	(as calculated from pitch length)		15.78	degrees
Cable Thick	1.413	mm	0.0556	in	0.0568	in
Cable Width	13.005	mm	0.5120	in	0.5140	in
Strand Size	0.805	mm	0.0317	in		
Total Cable Area	18.38	mm^2	0.0285	in^2		
Theoretical Packing Factors						
Edge PF	0.583					
Edge PF length	1.13	mm				
Middle PF	0.785					
Middle PF length	10.75	mm				
Filled Cable Area	15.71	mm^2				
Solder Area =	**2.67**	mm^2				
Estimate from Angles and strand data						
Strand Area	0.53	mm				
Filled Cable Area	15.80	mm^2				
Solder Area =	**2.58**	mm^2				

OUTER					Caliper measured	
Pitch Length	91	mm	3.5827	in	94.8	mm
# strands	34					
Pitch Angle	17.02	degrees	(as calculated from cable width)		17.64	degrees
Pitch Angle	15.23	degrees	(as calculated from pitch length)		14.60	degrees
Cable Thick	1.2077	mm	0.0475	in	0.0480	in
Cable Width	13.013	mm	0.5123	in	0.5140	in
Strand Size	0.703	mm	0.0277	in		
Total Cable Area	15.72	mm^2	0.0244	in^2		
Theoretical Packing Factors						
Edge PF	0.582					
Edge PF length	0.98	mm				
Middle PF	0.785					
Middle PF length	11.05	mm				
Filled Cable Area	13.81	mm^2				
Solder Area =	**1.91**	mm^2				
Estimate from Angles and strand data						
Strand Area	0.40	mm				
Filled Cable Area	13.65	mm^2				
Solder Area =	**2.07**	mm^2				

NbTi					Caliper measured	
Pitch Length	91	mm	3.5827	in	89.2	mm
# strands	30					
Pitch Angle	15.00	degrees	(as calculated from cable width)		15.17	degrees
Pitch Angle	15.39	degrees	(as calculated from pitch length)		15.71	degrees
Cable Thick	1.32	mm	0.0520	in	0.0531	in
Cable Width	13.09	mm	0.5154	in	0.5157	in
Strand Size	0.805	mm	0.0317	in		
Total Cable Area	17.28	mm^2	0.0268	in^2		
Theoretical Packing Factors						
Edge PF	0.583					
Edge PF length	1.13	mm				
Middle PF	0.785					
Middle PF length	10.84	mm				
Filled Cable Area	15.82	mm^2				
Solder Area =	**1.46**	mm^2				
Estimate from Angles and strand data						
Strand Area	0.53	mm				
Filled Cable Area	15.80	mm^2				
Solder Area =	**1.48**	mm^2				

Figure 126: Cable Data for Calculating Solder

Total Area = width of the three cables * height of Can
Strand Cross-Section from above sections
Total Solder Volume Needed = (Total Area - Strand Cross-Section) * Joint Length

Total Solder Volume from 4 ribbons of 1/8" Sn60 Solder at 3.75" long				
	3016.5	mm^3	0.184	in^3
Total Solder Volume from 4 ribbons of .010" Sn62 Solder at 3.75" long and 0.5" wide (LBNL)				
	1229.0	mm^3	0.075	in^3
Total Solder Volume from 4 ribbons of .010" Sn60 Solder at 3.75" long and 0.32" wide (TAMU die)				
	786.6	mm^3	0.048	in^3

Inner Joint				
Total Area =	54.05	mm^2		
Strand Area =	47.34	mm^2		
Solder Area =	6.70	mm^2	0.0104	in^2
Solder Volume =	638.41	mm^3	0.0390	in^3
0.5" Solder Thickness	0.13	mm	0.0052	in
0.32" Solder Thickness	0.21	mm	0.0081	in
1/8" Raw Solder Length	80.6	mm	3.17	in
+ 10% =	**88.7**	**mm**	**3.49**	**in**

Outer Joint				
Total Area =	51.31	mm^2		
Strand Area =	45.44	mm^2		
Solder Area =	5.87	mm^2	0.0091	in^2
Solder Volume =	558.66	mm^3	0.0341	in^3
0.5" Solder Thickness	0.12	mm	0.0045	in
0.32" Solder Thickness	0.18	mm	0.0071	in
1/8" Raw Solder Length	70.6	mm	2.78	
+ 10% =	**77.6**	**mm**	**3.06**	**in**

Figure 127: Solder Calculations

J. Assembly Images

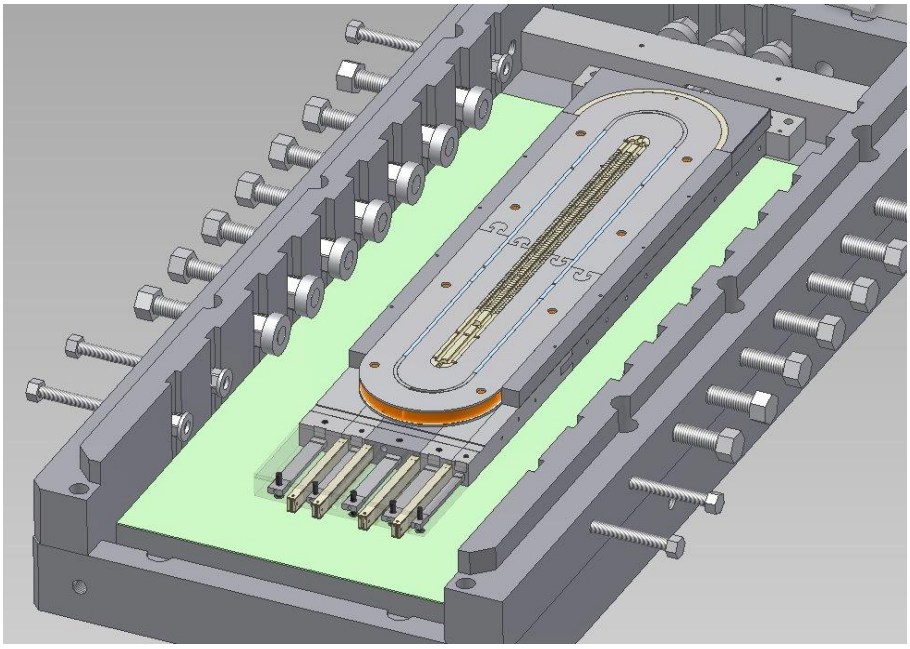

Figure 128: Magnet Inside Coffin for Splicing

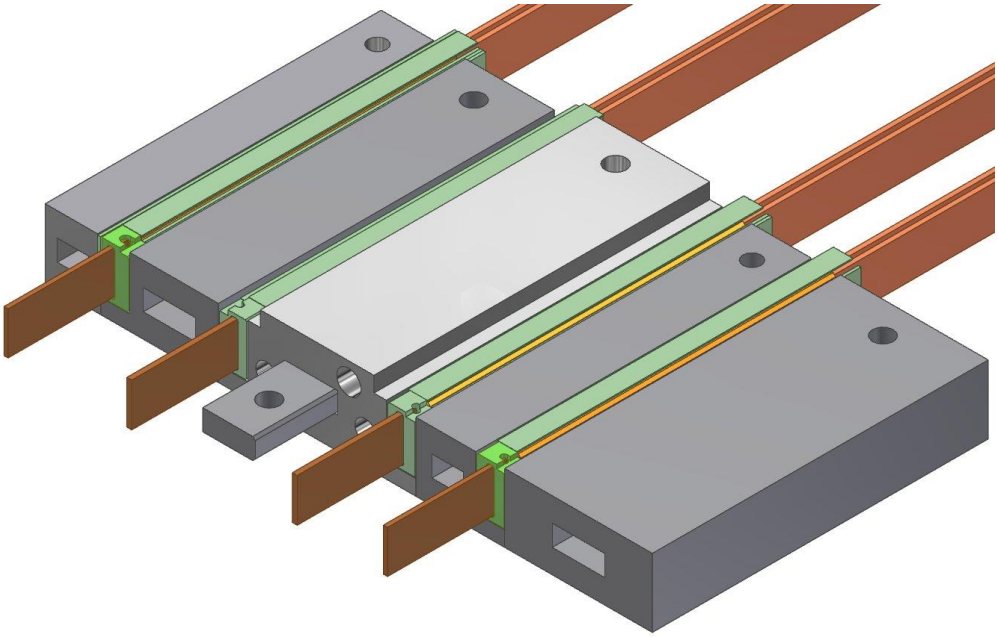

Figure 129: Insulation After Splicing is Complete

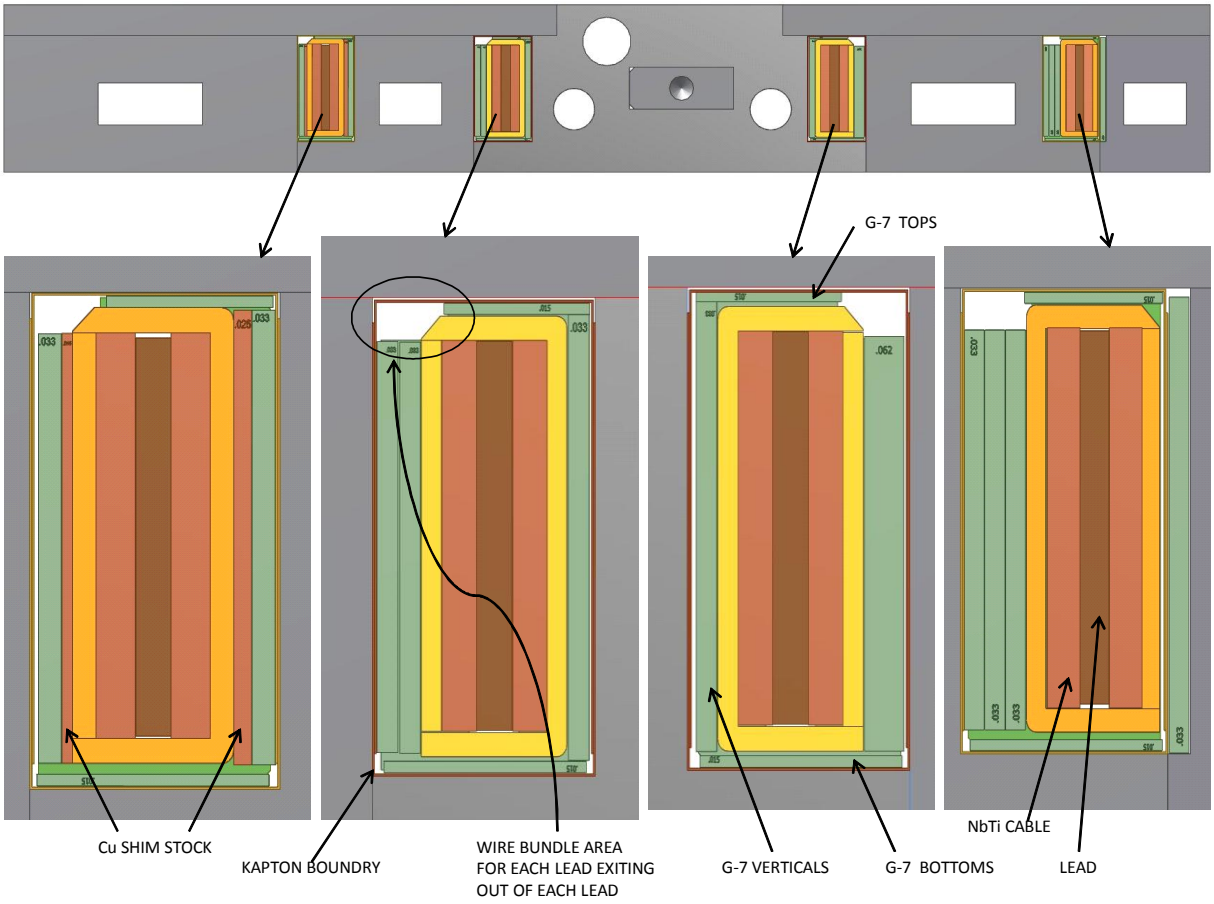

Figure 130: Insulation Package Cross Section After Splicing

K. TAMU3b Splicing Conclusion

1/25/2013: Began splice procedure on Tuesday. Performed inner splices Tuesday evening. Performed outer splices Wednesday afternoon. Completed lead voltage tap and carbon resistor insulation and check on Thursday night.

Each joint compressed as designed accept for the Outer In. The heater block was tilted during the compression. The bottom of the joint closed as designed and the top is 0.011" large.

Splicing Shims

Inner In	Left	Right
	SS 0.015"	Al 0.037"
		Al 0.010"
		Al 0.010"
Inner Out	Left	Right
	Al 0.037"	SS 0.015"
Outer In	Left	Right
	NONE	Al 0.060"
Outer Out	Left	Right
	Al 0.125"	NONE

Pre-Impreg Shims

Inner In	Left	Right
	G-10 0.033" (short)	Cu 0.015"
	Cu 0.015" (short)	G-10 0.033" (tall)
Inner Out	Left	Right
	G-10 0.030"	G-10 0.062"
Outer In	Left	Right
	G-10 0.033" (short)	Cu 0.015"
		G-10 0.033" (tall)
Outer Out	Left	Right
	G-10 0.033" X3 (short)	G-10 0.030" (extra tall)

Carbon resistor measurements with Fluke DVM

II	52.7 Ω
IO	55.8 Ω
OI	53.9 Ω
OO	52.9 Ω

Inner Coil to ground = 214 Ω

Outer Coil to ground = 140 kΩ

L. TAMU3c Splicing Conclusion

9/25/2013: Began splice procedure on Monday evening. Performed inner splices Tuesday morning and outer splice Tuesday night. Completed lead voltage tap, carbon resistor insulation, and packaging by Wednesday evening.

Each joint compressed as designed. The final distance between heater blocks for the inner joints was 0.014" too large, but the copper can size of both the inner in and inner out was within tolerance. A pool of solder collected on the top of the outer in joint on the coil side, but it was not attached and was removed with tweezers.

Splicing Shims

Inner In	Left	Right
	SS 0.015"	Al 0.037"
		Al 0.010" X2
Inner Out	Left	Right
	Al 0.037"	NONE
	SS 0.015"	
Outer In	Left	Right
	NONE	Al 0.060"
Outer Out	Left	Right
	Al 0.125"	NONE

Pre-Impreg Shims

Inner In	Left	Right
	G-10 0.033" (short)	Cu 0.015"
	Cu 0.015" (short)	G-10 0.033" (tall)
		Cu 0.003" X2
Inner Out	Left	Right
	G-10 0.033" (tall)	G-10 0.033"
	Cu 0.015"	Cu 0.024" (shortened)
Outer In	Left	Right
	G-10 0.033" (short)	Cu 0.024"
	Cu 0.003" X2	G-10 0.033" (tall)
Outer Out	Left	Right
	G-10 0.033" X2 (short)	G-10 0.030" (extra tall)
	G-10 0.030" (short)	

Carbon resistor measurements with Fluke DVM

II	53.48 Ω
IO	54.92 Ω
OI	54.20 Ω
OO	54.57 Ω

Inner Coil to ground = 0.559 kΩ

Outer Coil to ground = 29.3 kΩ

M. Inter-coil Splicing Procedure

1. Assemble the inter-coil splice fixture and verify that the cartridge heaters fit in the appropriate holes.
2. Use the same procedure for producing solder strips as used for the Nb3Sn – NbTi splicing procedure. Roughly 6” of 1/8” diameter solder in 4” ribbons x5.

Figure 131: Inter-Coil Splicing Setup

Figure 132: Pre-Bending Inter-Coil Joint

3. Apply flux to solder strips and NbTi cable. Gloves are recommended.
4. Pre-bend the NbTi conductors in roughly the same shape as the die set and insert solder strips as shown in Figure 131 and Figure 132.
5. After assembling the inner solder strips between cables, place the inner splice fixture piece on the cable and compress the cable with two small clamps. Leave these clamps on until the splice joint is completed. This keeps the cable from bowing out.

Figure 133: Applying Solder Between Cables

6. Place the final solder strip in place and finger tighten the outer splice fixture halves as shown in Figure 133. Over tightening the clamps will inhibit the cartridge heaters from fitting.
7. Place the cartridge heaters in place and fully tighten the outer fixture clamps.
8. Install the thermocouples as shown in Figure 134.
9. Turn on power to the cartridge heaters with the set point equal to 320°F on the cart shown in Figure 135.
10. The solder should begin to melt in roughly one minute. Tighten the outer halves of the splice fixture until the fixture is completely compressed

11. Cool the joint with a damp cloth and remove extra solder with an iron until you have a completed joint as in Figure 136.

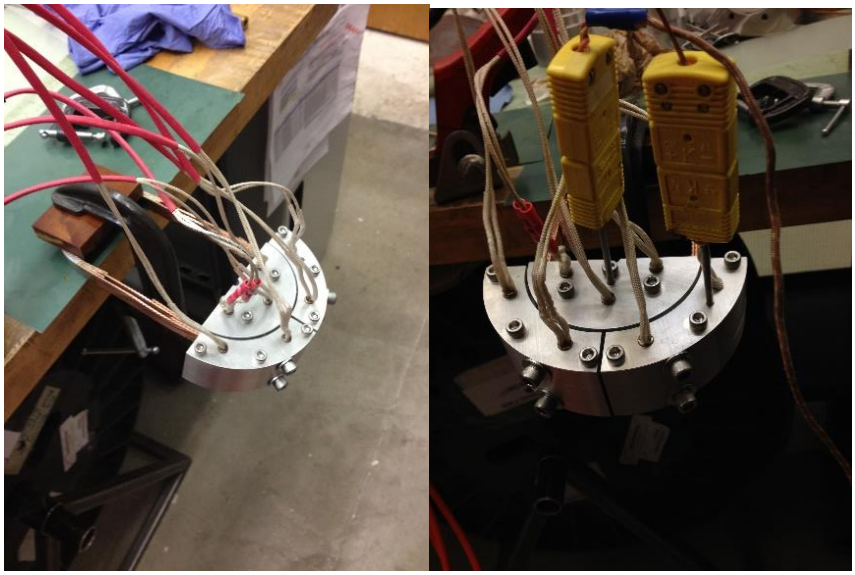

Figure 134: Inter-Coil Splicing Fixture with Short Cartridge Heaters

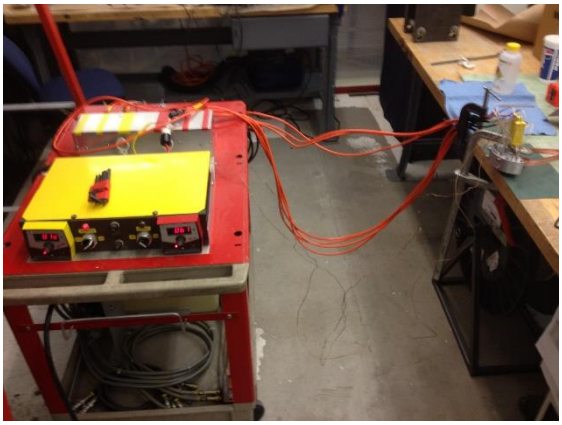

Figure 135: Splicing Heating Cart

Figure 136: Completed Joint

APPENDIX B: HEAT TREATMENT PROCEDURES

This procedure was developed over the span of roughly one year of plumbing, wiring, and calibrating the reaction bake furnace to maintain tight and automated control of the temperature as well as gas flow. The majority of that time was performing test heat treatments on a dummy coffin to fine tune the Proportional, Integrative, and Derivative (PID) variables to control the extremely large thermal mass of the magnet and coffin.

1. Make sure power is off to the heating elements by plugging the interlock into the storage position for crane operation.
2. Make sure that each interlock is connected to the bracket on the chain link fence for crane operation.
3. Correctly install all K-type thermocouples inside the coffin.
    a. Check each thermocouple for shorts by warming the end with your hand
    b. Install a primary and a backup thermocouple at each of the following locations:
        i. Top Zone on magnet base
        ii. Middle Zone on magnet base
        iii. Bottom Zone on magnet base
        iv. Top Zone on magnet base for over-temperature safety switch
        v. See Figure 138 and Figure 137 for all other locations.
    c. Install other thermocouples in the coffin.
    d. Document and take pictures of thermocouple locations.

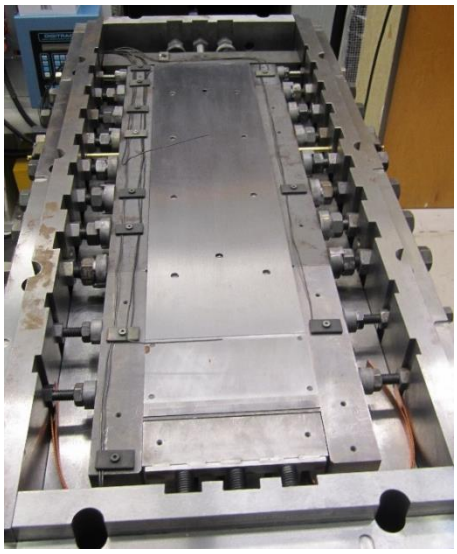

Figure 137: Thermocouple Distribution in Coffin Retort

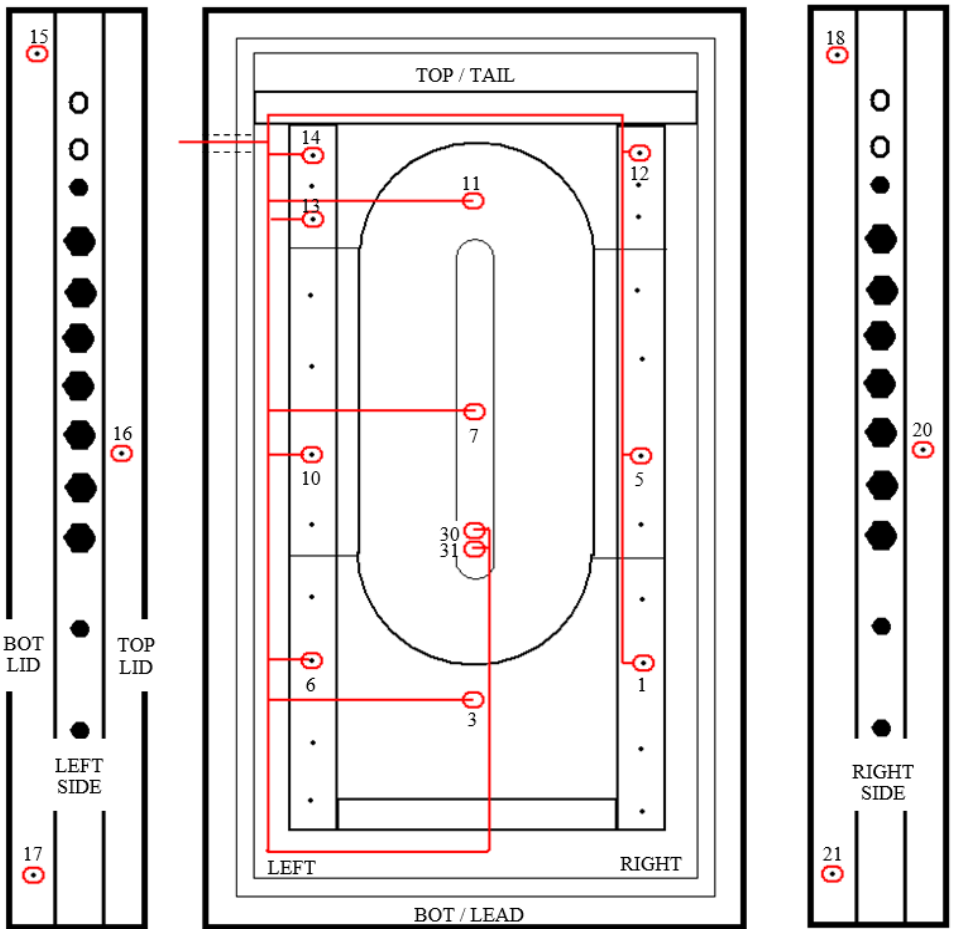

Figure 138: Heat Treatment Thermocouple Map

4. Install all gas lines from the inside of the coffin to the outside of the coffin. Document and take pictures.
5. Bolt the coffin closed.
6. Place the coffin inside of the furnace with the leads down and the gas manifold facing the SS inlet tubes.
7. Connect all of the gas lines inside of the furnace one subsystem at a time. Flow check each subsystem to be sure inlets and outlets are properly identified.
    a. Blow out the Gas lines before installation to remove particulates.
    b. A supply and return line for the inner windings
    c. A supply and return line for the outer windings

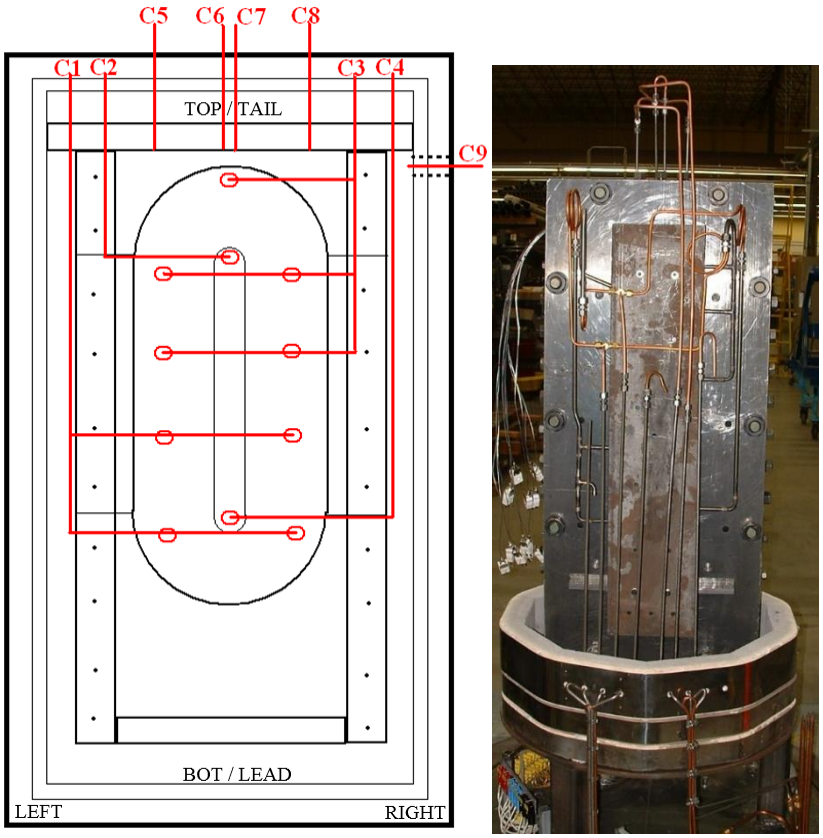

Figure 139: Heat Treatment Argon Flow Map and Flow Lines

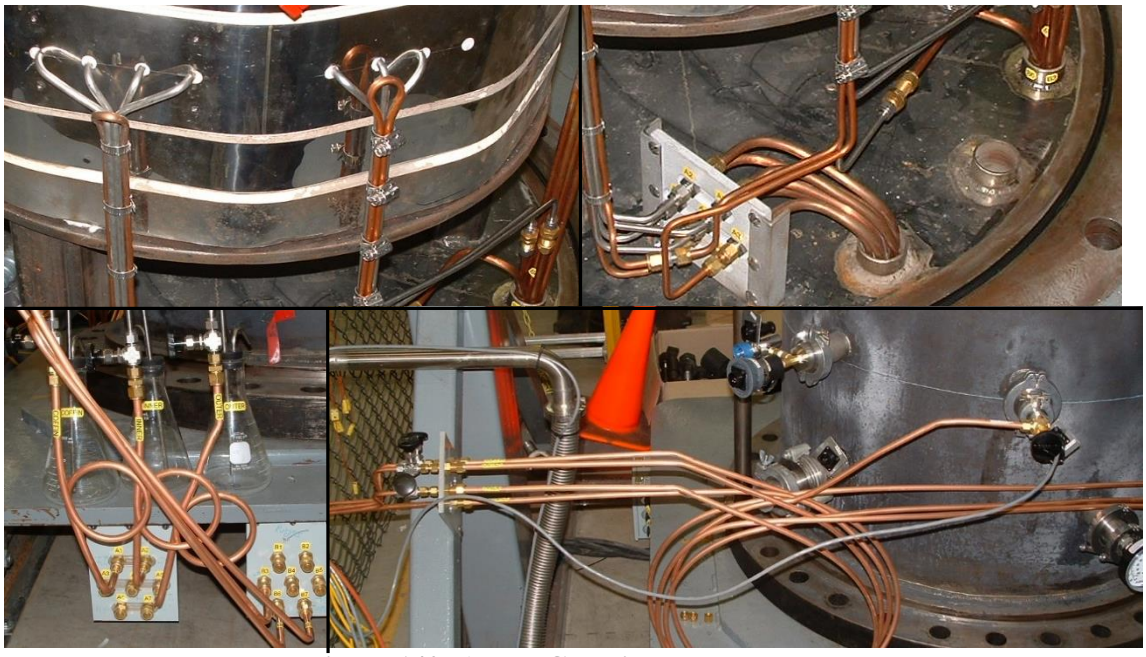

Figure 140: Argon Gas Lines and Bubblers

d. A supply and return line for the body of the coffin.

e. See Figure 139, Figure 140, and Table 21 for connections.

f. Document and take pictures of all gas lines.

Table 21: Argon Connections

Line Labels	Location
C1&C3 – F2 – A5	Outlet from outer coil
C2&C4 – F3 – A2	Outlet from inner coil
C5&C8 – F5 – B6	Inlet to outer coil
C6&C7 – F6 – B7	Inlet to inner coil
C9 – F7 – B3	Inlet to coffin retort
OPEN – F4 – A1	Outlet from coffin
A6 – (F5 to F7) (F1 to F4) – A7	Cooling line
F1-A4	Extra feed
A3, B1, B2, B4, B5	Blank offs

8. Place all heating elements on the furnace base in order with heating element #6 on bottom and #1 on top.

   a. Install the thermocouples that are on the outside of the coffin.

   b. Carefully allow all thermocouple leads to be placed between elements.

c. Connect each thermocouple appropriately (See Figure 138.)
d. Connect each heating element appropriately.
e. Check each wire and gas line to assure proper clearance with the furnace cover.
f. Document and take pictures.

9. Perform resistance tests of thermocouple elements at junction block at the edge of the furnace base. Check for continuity and for shorts to heating elements.
10. Perform resistance tests of heater elements at junction block at the edge of the furnace base. Check for continuity and for shorts to heating ground.
11. Screw in the 3 furnace cover guide rails and clean the O-ring grove and surface on the furnace cover and base.
12. Turn the power on to the crane.
13. Lift the furnace cover with the crane, roll the furnace base beneath the cover, and lower the furnace cover. Be careful not to gouge the O-ring surface with the guide rails. Put the data logger in place and put up the yellow safety chain around the furnace.
14. Bolt the furnace cover in place and load the bolts uniformly (Tightening every 5^{th} bolt should be adequate.) This step may be completed during pump down.
15. Connect the back-fill gas and vacuum lines, the vacuum gauge, and all interlocks onto the body of the furnace.
16. Connect the appropriate thermocouples.
    a. Connect the three zones to the controller and the data logger. Use the labeled TC splitter extension wires.
    b. Connect all additional internal and external furnace thermocouples to the data logger (See Figure 138)
    c. Connect the over-temperature safety switch (set to cut power to heating elements at 705ºC) thermocouple. Use the labeled TC splitter extension wire.
    d. Document and take pictures.

17. Connect and flow test the gas lines on the outside of the furnace one at a time to verify identity of flow meter and bubbler:
    a. A supply and return line for the inner windings
    b. A supply and return line for the outer windings
    c. A supply and return line for the body of the coffin
    d. Each supply line should have a valved flow meter with a low pressure regulated argon supply
    e. Each return line should be valved and have a water bubbler to collect silane effluent
    f. Document and take pictures
    g. Note: the back-fill gas supply is located on the side of the furnace cover and should already be connected.
18. Close the backfill gas valve and the inlet and bubbler gas valves and pump down the furnace for several hours until the vacuum is better than 100 mTorr. Back-fill with Argon to atmospheric pressure. Repeat 2 more times. Note: 50 mTorr will take 10 hours and 30 mTorr will take a day from STP.
19. Initialize the 3 Zone controllers.
20. During the pump and back-fill cycles the temperature controllers should be programmed and the data logger verified.
    a. Program the Ramp-Soak periods for each zone as follows:
        i. See the controller manual in control panel door for programming instructions and Table 22.
        ii. Note that the temperatures in the table incorporate the calibration curves of each TC against a NIST calibrated TC.
        iii. The actual Heat treatment is as follows:
            1. Ramp at 50ºC / hour to 210ºC and soak for 48 hours.
            2. Ramp at 50ºC / hour to 340ºC and soak for 48 hours.
            3. Ramp at 37ºC / hour to 670ºC and soak for 70 hours then furnace cool.

iv. OST recommended HT [113]

Table 22: Three Zone Heat Treatment Schedule

Procedure	TOP SP	Time (min)	MID SP	Time (min)	BOT SP	Time (min)
4-0	19.4	19	22.4	1	25.4	1
4-1	34.4	14	34.4	32	34.4	32
4-2	184.7	192	196.2	206	178.2	185
4-3	184.7	4	196.2	15	178.2	10
4-4	205.9	25	206.5	11	206.9	32
4-5	208.9	294	209.5	336	209.9	318
4-6 to 5-1	208.9	2880	209.5	2827	209.9	2850
5-2	208.9	19	219.5	19	219.9	1
5-3	217.9	11	219.5	11	219.9	29
5-4	325.8	150	324.1	125	333.7	137
5-5	325.8	49	324.1	88	333.7	90
5-6	335.0	28	333.8	53	335.3	41
5-7	340.0	180	339.9	300	341.2	190
6-0 to 6-3	340.0	2880	339.9	2721	341.2	2829
6-4	341.0	10	349.9	12	351.2	1
6-5	350.0	20	349.9	18	351.2	29
6-6	672.0	522	660.9	505	661.2	506
6-7	672.0	0	660.9	10	661.2	0
7-0	672.0	0	671.4	17	671.1	16
7-1 to 7-5	672.0	4200	671.4	4190	671.1	4200
7-6	0.0	1	0.0	1	0.0	1

1. 210ºC / 48 hours – duration should increase if large temperature uncertainty
2. 400ºC / 48 hours
3. 640 - 695ºC / 50 - 220 hours
    a. FNL 640-650ºC / 48-50 hours [61, 114, 115]
    b. LBNL 650-665ºC / 80-200 hours [116-118]
    c. NHMFL 640ºC / 60 hours [78]
    d. BNL 650ºC / 80 hours [119]
    e. CHMFL 640ºC / 80 hours [120]
4. Forming Nb_3Sn at 670ºC for 70 hours should produce roughly 2800 A/mm^2 (12 T, 4.2 K) and a RRR of 30.

v. The initial temperature is assumed to be 23.4ºC. The first ramp is optimized for 50ºC / hour and the second ramp for 37ºC / hour.

This is the fastest that the furnace can ramp the coffin to minimize temperature gradients in the magnet and minimize parasitic phase formation at intermediate temperatures.

vi. The procedure step 0-2 duration will be calculated from the 50ºC / hour ramp rate and current temperature

b. Program the PID and I_{offset} according to Table 23 and the instructions in the control panel door.

Table 23: Heat Treatment PID Parameters

ZONE	PID#	Set Point	P (ºC)	I (sec)	D (sec)	I_{offset} %
TOP	0	5.0 ºC	25.0	0	0	25.0
MID	0	5.0 ºC	18.4	0	0	48.0
BOT	0	5.0 ºC	3.5	0	0	100.0
TOP	1	338.0 ºC	60.0	3000	313	6.8
MID	1	338.0 ºC	98.0	5040	525	0.6
BOT	1	338.0 ºC	28.0	7776	810	11.3
TOP	2	350.0 ºC	16.0	0	0	25.0
MID	2	350.0 ºC	11.0	0	0	48.0
BOT	2	350.0 ºC	3.0	0	0	100.0
TOP	3	658.0 ºC	12.4	1469	153	22.2
MID	3	658.0 ºC	47.5	4342	452	7.2
BOT	3	658.0 ºC	10.5	4309	449	31.9

c. Test the Data Logger by collecting data for a few hours and verifying the output. Set the Data Logger to take data every minute for a manageable file size.

21. After the pump and back-fill cycles, start gas flow through windings and coffin for one or two bubbles per second.
    a. Always maintain a positive pressure in the magnet relative to the coffin.
        i. Only flow gas into the inner and outer windings and close off the coffin and furnace inlets.
            1. Set the inner and outer winding flow rates to the same value as indicated on the flow meters.

2. Adjust the three bubbler valves so that gas is flowing through each roughly the same amount.
3. Three to Four bubbles per second is adequate.

22. Initialize the Controllers and Data Logger.
23. Test the UPS by disconnecting and reconnecting the 480V plug.
24. Start the Reaction/Formation Bake at the controllers and Data Logger (DAQ). Start the DAQ exactly 10 minutes before the controllers to collect RT values
    a. Do not remove the thermocouples from the controllers. This causes the Integral of Error to reset and will change the % output accordingly.
    b. Do not remove the over-temperature safety TC as this will cut power to heating elements.
25. Carefully observe the furnace for at least an hour to make sure the temperatures are ramping together. Be present and observe each line or step being processed for the entire heat treatment schedule. Figure 141 shows the dummy load result from the preceding parameters.

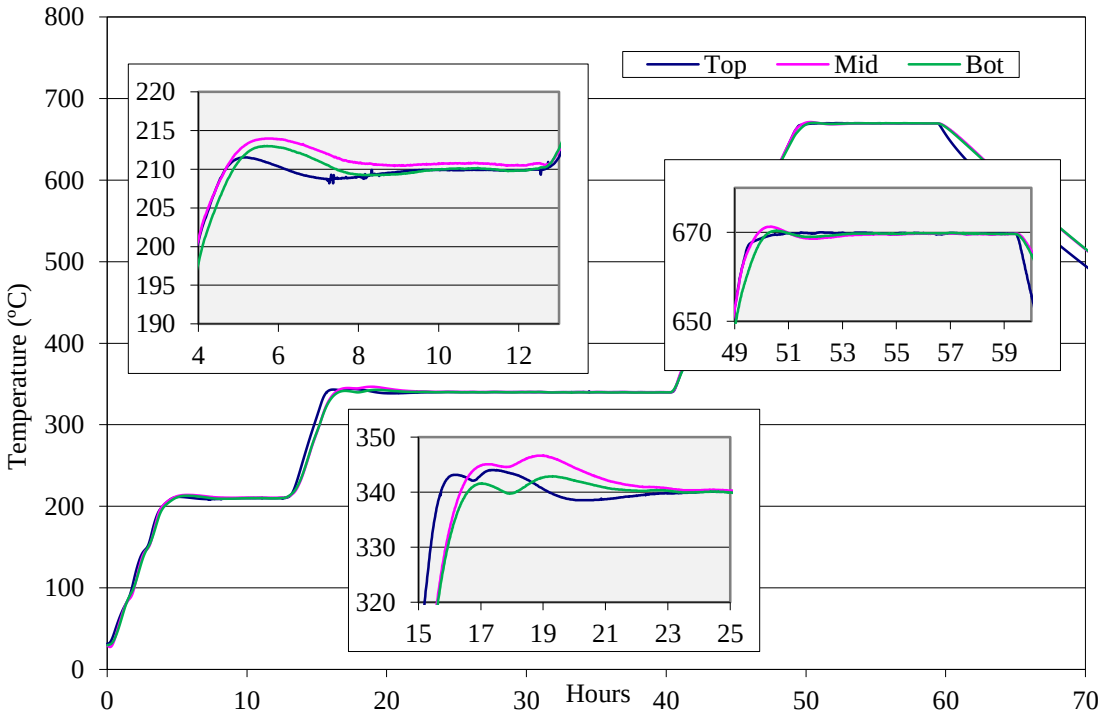

Figure 141: Heat Treatment Soak Overshoots

26. PID Parameter Adjustment

a. Adjusting parameters during actual bake is **STRONGLY** ill advised. This resets the built up integral of error and derivative values and will cause the temperature to decrease for several hours after adjustment.
b. If excessive overshoot is eminent, unplug the power to the pertinent zone rather than adjusting the controllers.
c. PID Settings
    i. Proportional Band (**P**) – Increasing the PB will make the output **less** aggressive according to the following relation:
        a. **Error**/**P** *100% = % output
        b. **Error** = Set Point – Process Variable
    ii. Integral Time (**I**) – The integral time is the time it takes for the percent output from the error to double. Increasing the integral time decreases the % output according to the following relation:
        a. $1/(\mathbf{P}*\mathbf{I})\int \mathbf{Error}\,dt$ * 100% = additional % output
        b. Integral of **Error** = $\int \mathbf{Error}\,dt$
    iii. Derivative Time (D) – The derivative time is how long in the future the controller looks if the current change in **Error** was maintained and adjusts the % output accordingly. Increasing the derivative time increases the % output according to the following relation:
        a. **D**/**P** * d/dt (**Error**) * 100% = additional % output
    iv. So in total the output is the following:
        a. $\%\,\text{output} = \frac{1}{\mathbf{P}}\left(\mathbf{Error} + \frac{1}{\mathbf{I}}\int \mathbf{Error}\,dt + \mathbf{D}\frac{d}{dt}\mathbf{Error}\right)*100\%$
        b. The lag time is roughly 30 minutes and adjusting these parameters is highly dependent on the current

temperature distribution of the load relative to the set point.

v. The Integral offset ($\mathbf{I}_{offset}$) is the initial percent output when the Controller is in **PID** mode and **Error** is zero.
    1. In other words this gives an initial value to the integral of **Error**.
    2. The $\mathbf{I}_{offset}$ only works in PID mode and not in RAMP/SOAK mode.
        a. In RAMP/SOAK mode the controller calculates or maintains the Integral of **Error** from previous segments of the ramp/soak procedure.
        b. When **I** and **D** are set to zero the initial Integral of **Error** is not effected. This is why **I** and **D** terms are zero during ramps. Otherwise the integral of **Error** would accumulate and be too large.

d. Set Points
    i. When the controller is in automatic mode the PID setting (0, 1, 2, or 3) is chosen with the closest Set Point.
        1. PID #0 is for the initial ramp
        2. PID #1 is for the 210ºC and the 340ºC soak
        3. PID #2 is for the last ramp
        4. PID #3 is for the 670ºC soak
    ii. The differences in settings for each zone at procedure step 0-2, 1-3, and 2-4 are there so that the Integral of the error has time to become large enough to adequately affect the output.
        1. The times and temperatures are set to maintain the 50ºC/hour rate on the first ramp and the 37 ºC/hour rate on the second ramp.

2. Increasing the time (decreasing the temperature) increases the integral of the error and thus the % output or overshoot would increase.

iii. At step 0-2 the PID # automatically changes from 0 to 1

iv. At step 2-3 the PID # automatically changes from 1 to 2

v. At step 2-4 the PID # automatically changes from 2 to 3

vi. The changes in settings at procedure step 0-0, 1-2, and 2-2 are there so that the different zones will ramp together.

e. Failure Modes

i. If power to the temperature controller is interrupted, the controller resets itself and starts the program over upon powering back up.

ii. If the thermocouple is removed or disconnected and then reconnected, the cumulative Integral of **Error** is reset.

1. This will cause the process variable to decrease and remain low by 4 or 5 degrees (depending on the zone and Integral time) for approximately 4 to 5 hours until the Integral of **Error** increases.

2. If this is unacceptable then the controller can be set to PID mode where the integral offset is programmed and the decrease in process variable will be minimized. However, the controller will need to be reprogrammed so that the ramp/soak temperatures and times are correct when changing back to ramp soak. This would be very difficult and risky to do if incorrectly programmed.

iii. If a zone is over the set point temperature by an uncomfortable amount, power to that particular zone can be disconnected.

1. Disconnect the labeled 480V zone plugs on the right side of the control panel.

2. A large overshoot or over temperature would indicate that a zone controller was improperly programmed or a catastrophic failure.
    a. Look at the % output of the controller.
    b. Look at the PID values and the program procedure.

APPENDIX C: S-GLASS AND MICA PRODUCTION PROCEDURES

In preparing this procedure for producing S-Glass and Mica magnet pieces the author has taken time to be as thorough as possible. If in the process of making pieces you develop a more sophisticated method or trick, or if places seem overly complicated or vague please ignore. Working with mica is much more forgiving and so more attention has been given to cutting S-Glass with this procedure.

Page

WARNING: If not using the downdraft table, wear a breathing mask and covering clothes to minimize contact with S-Glass strands.

WARNING: Always cut and handle magnet material with cotton gloves to prevent contamination.

A. Material Preparation

1. S-Glass

Figure 142: Mica and S-Glass Storage Cabinet

1. Prepare a clean surface upon which to place the cut material.
2. The S-Glass is stored in the wooden cabinet in the winding room. Open the drawer-shelf below the S-Glass Roller Mount. Extend the metal flaps and fold over the drawer-shelf extension as shown in Figure 142.
3. Remove the plastic and Velcro protection sheet. Be careful not to snag the Velcro on the S-Glass.
4. Slowly unroll the S-Glass until it reaches the end of the extension.
5. Using fresh scissors, cut out a rectangle that is 2 inches larger in width and length than the template being used and place the piece on your clean surface.

NOTE: If a pen or marker was used, please remove the marked portion from the roll.

WARNING: Do not have any marked portion be placed between the templates. The carbon is a conductor and could short consecutive windings if implanted in the epoxy during impregnation.

6. Gently role the remaining material back onto the S-Glass roller mount, retract the shelf extension, and replace plastic and Velcro protection sheet.
7. Using the butane hand held torch in the flammables cabinet in the winding room, gently sear the ends of the cut piece of S-Glass to prevent excessive fraying.

WARNING: Pay close attention to what is around you and what is behind the S-Glass edge when using the butane torch. Soot from anything that catches fire will contaminate the S-Glass.

2. Mica

NOTE: Pay close attention to whether you are cutting the 0.002" or 0.004" mica. The rolls and the Garolite storage sheets are labeled.

WARNING: Be careful not to jar or jolt the roll because it easily fractures.

WARNING: When unrolling the mica do not allow the weight of the roll to rest on the table. Use a partner if necessary. Unrolling the mica like Christmas paper will result in creases and flakes forming and the destruction of large amounts of material.

1. Prepare a large clean table top upon which to place the material.
2. Place 2 or 3 layers of brown paper to protect the tabletop when cutting with a razor.
3. The mica is stored in the wooden cabinet in the winding room.
4. Unroll whatever amount is needed without allowing the weight of the roll to touch the table top. The weight of the roll on the thin mica creates creases.

Figure 143: Razor Cutting Illustration

5. Using a fresh razor, cut out a rectangle that is tactfully (2 inches) larger in length and width than the template. See Figure 143 for cutting with the razor. Push with roughly 4 or 5 lbs of force.

NOTE: If a pen or marker was used, please remove the marked portion from the roll.

WARNING: Do not have any marked portion be placed between the templates. The carbon in the ink will create a short between windings in the magnet and cause a premature quench during ramp.

6. Gently wrap excess material back onto the roll without allowing the weight of the roll to rest on the table. Place roll back into wooden cabinet.

3. Templates

1. Make sure that the template surfaces that mate to the material are smooth and polished.
2. Use a fine grit flat stone or sand paper backed by a flat object to remove rough spots on the mating surface.

NOTE: Don't use sanding paper alone because it will create high spots on the template.

3. Remove all shavings and residue once with acetone and repeatedly with alcohol. Continue with alcohol until little or no discoloration occurs with a Kimwipe®.

B. Material and Template Configuration

NOTE: The alignment and fastening procedure is the same for mica and S-Glass.

1. Initial Alignment with Large Clamps

NOTE: The templates are filed and polished on only one side using fine grit stones. Using the wrong side on the template fixture may result in tears or an uneven material finish. Have the 6 large deep throw C-clamps, the box of small screw clamps, the sharp scissors, and a flashlight ready.

1. First clean off the surfaces of the template holding fixture on the downdraft table.

2. Mount half of the cleaned template on the holding fixture with the polished side up.
3. Then roughly center the pre-cut material on the template in the holding fixture.
4. Then slowly place the second half of the template centered on the material with the polished side down and in the same orientation as the first half of the template.
5. With your eyes and the flashlight in the same plane of the material and along one long straight edge, align the top and bottom halves of the template as shown in Figure 144 and Figure 145.

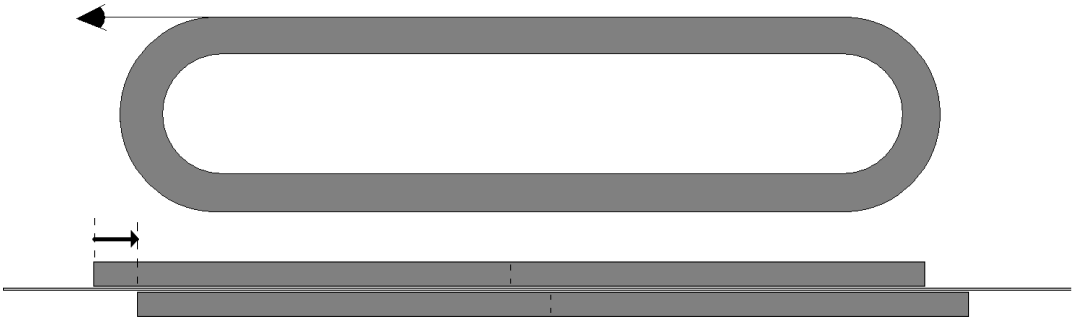

Figure 144: Template Alignment Illustration

6. Repeat step 6 on the 3 remaining corners.
7. With your eyes and the flashlight in the same plane of the material and along the tangent line created by the apex of one curve, align the top and bottom halves of the template.

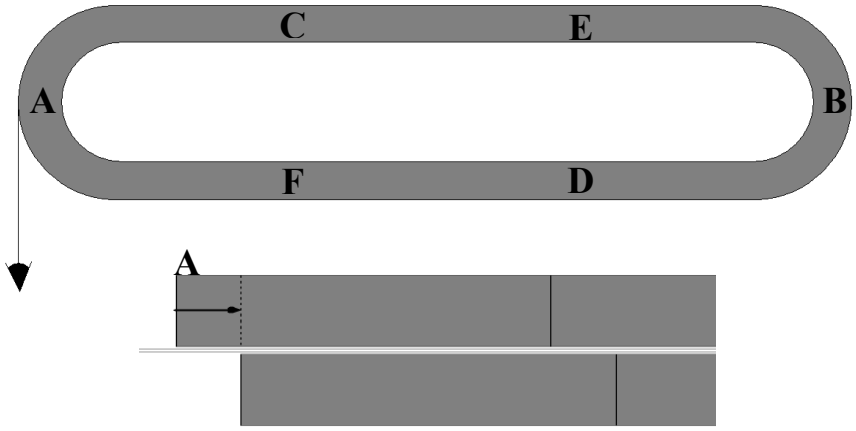

Figure 145: Horizontal Template Alignment

NOTE: The solid lines on the right on Figure 145 are the transition lines between the straight edges and the curves.

8. Repeat step 8 on the other end of the template.
9. Gently tighten 2 large deep throw C-clamps at points A and B of Figure 145.

NOTE: The small screw clamps will securely and tightly fasten the templates together later. The large C-clamps are only temporary for alignment purposes.

10. Repeat steps 6 through 9 after placing the C-clamps at the ends.

HINT: Loosen the two clamps until they barely touch the holding fixture table top. This will keep the clamps in contact so that the templates don't move easily but will allow fine adjustment.

NOTE: If necessary, you may carefully use scissors to trim away excess material to increase visibility of the edges.

NOTE: The templates are built to high precision with the EDM. It is possible to align the templates to within a few thousandths of an inch. Failure to do so causes fraying when cleaning the edges.

11. Tighten two more clamps at points C and D of Figure 145.
12. Repeat steps 6 through 9 until perfectly aligned visually.
13. Tighten the last two clamps at points E and F of Figure 145 and repeat steps 6 through 9 if necessary.

2. Fastening the Templates for Cutting

NOTE: There are 26 small screw clamps to disperse.

1. Make a plan where to lay out the clamps under the following guidelines (see Figure 146 for an example):
    a. Plan on having at least one clamp at each of the four corners that are in contact with the template holding fixture.
        i. This is to lift the templates off of the holding fixture surface so that the fixture doesn't deflect the cutting flame.
        ii. It also prevents the template and the holding fixture from overheating.
    b. The templates have anywhere between 0 and 6 joints where they were TIG welded. The templates aren't perfectly flat at these points. Place a clamp roughly half an inch on each side of the joint to minimize gaps. Places on the template that aren't flush cause fraying when cleaning the edges.
    c. Pay close attention to the rounded edges. They are prone to gaps between the templates when cleaning.
    d. Save the last 6 small screw clamps to replace the large C-clamps.

Figure 146: Template Clamping Schematic

2. Next use the scissors to make V- groves in the material so that the small screw clamps can be fastened where needed. See Figure 147.

NOTE: Be careful not to cut closer than an eighth inch to the template.

WARNING: If cutting S-Glass, do not pull loose strands that are weaved perpendicular to the edge of the templates or else damage will occur to the internal weave.

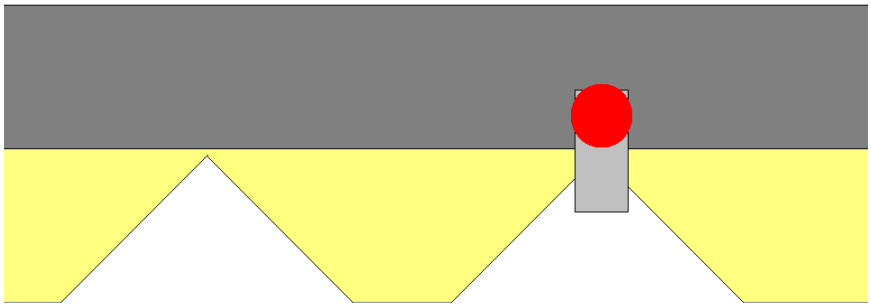

Figure 147: Clamping Illustration

3. After hand tightening the screw clamps remove the deep throw C-clamps and replace with the remaining 6 screw clamps.
4. At this point you may want to gently tighten the clamps roughly an eighth to a quarter of a turn with a pair of pliers.
5. If the clamps are tight, the templates are aligned, and the layout looks something like Figure 148, you are ready to begin cutting the inside of the template.

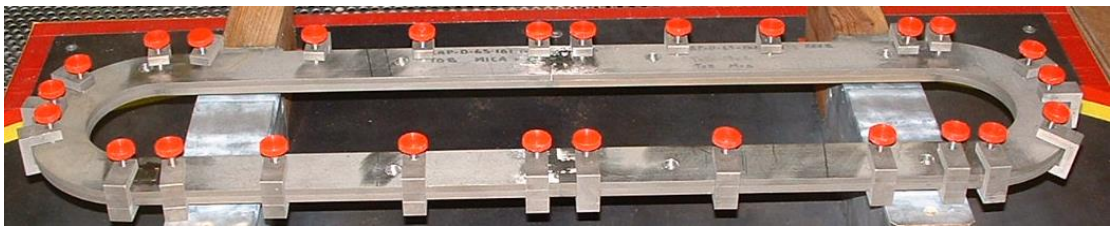

Figure 148: Clamp Spacing

C. Torch Operation

1. Needle Torch Setup

NOTE: The 5 or 7 tip may be used without adverse effects.

1. Use the number 6 tip on the needle torch.
2. Make sure a flash inhibitor is in series with the acetylene.

3. Open the oxygen valve on the tank 1½ rounds and the oxygen on the needle torch one round and set the pressure to roughly 8 psi on the regulator.
4. Close the oxygen needle torch valve.
5. Open the acetylene valve on the tank 1½ rounds and the acetylene on the needle torch one round and set the pressure to roughly 2.25 psi on the regulator.
6. Close the acetylene needle torch valve.

NOTE: Do not over tighten the needle valves.

2. Needle Torch Ignition

WARNING: When igniting the torch it is important to minimize carbonization (soot) of the acetylene. The carbon is a conductor and could short consecutive windings if implanted in the epoxy during impregnation.

1. After setting the torch up, open BOTH the oxygen and the acetylene valves on the needle torch as close as possible to ¾ of a turn.
2. With the LightningBug® striker ignite the torch.
3. Leave the acetylene at ¾ of a turn open and turn down the oxygen until the bright blue part of the flame is 1 inch tall.
4. Then open up the oxygen valve until only a pencil tip or 1/8th of an inch of the bright blue flame is visible.

NOTE: This is not typical oxy-acetylene ignition procedure but will not create soot.

3. Needle Torch Extinguishing

WARNING: It is important to extinguish the torch without carbonization to minimize contamination of the magnet material.

(a) The Preferred Method

1. Turn down the acetylene without extinguishing the flame.
2. Then turn down the oxygen without extinguishing the flame.
3. Repeat steps 1 and 2 until the flame is extinguished by turbulence.

(b) The Quick Method

1. Totally cut off the acetylene of the needle torch.
2. Then cut off the oxygen.

WARNING: When the torch is especially hot, the loud pop created by lingering acetylene may expand the diameter of the number 6 needle torch tip. Use this option only if you need to quickly extinguish the torch.

D. Cutting Instructions

WARNING: Soot from almost anything that catches fire will contaminate the material.

NOTE: Before making any cuts it is strongly suggested that you practice on scrap material.

NOTE: The angle of the torch head relative to the handle is 45º. You have freedom to rotate the torch head so that you have maximum support to remain steady.

1. Cutting Edges

NOTE: The parameters for cutting Mica is the same but the surface speed may be increased from 3 seconds per inch to 1.5 seconds per inch.

1. Always clear out behind the templates anything flammable.

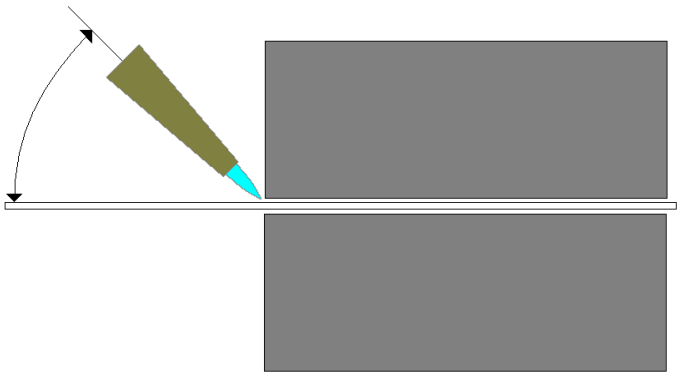

Figure 149: Torch Angle Illustration (Cross Sectional View)

2. See Torch Operation for igniting the torch.

3. Hold the light blue tip of the flame directly at the point where the material meets the template crevice.
4. Looking along the edge of the Template hold the torch at a 45º angle relative to the plane of the material and the edge of the template. See Figure 149.

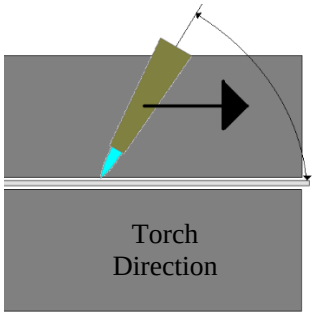

Figure 150: Torch Angle Illustration (Longitudinal View)

5. Looking at the side face of the templates, hold the torch at a 60º angle relative to the material. See Figure 150.
6. Pull and don't push the flame across the crevice described in step 3.

NOTE: Pushing the tip causes build-up of glass beads and excessive melting of material. Take roughly 3 seconds to move 1 inch. (0.3 inch / second)

NOTE: Practice will help to follow this instruction. Too slow will melt the material between the templates excessively and create excessive build-up of microscopic glass shards after cleaning the edges. Going too fast will sear and singe the edge poorly and cause fraying after cleaning the glass beads.

WARNING: Going too slow may potentially melt the templates.

7. Extinguish the needle torch.

NOTE: Do not over tighten the needle valves of the torch.

2. Cutting Holes

NOTE: The hole diameter for the templates is 3/8 of an inch.

1. See Torch Operation for igniting the torch.

2. Hold the light blue tip of the flame directly at the point where the material meets the template inside the hole.
3. Hold the handle of the torch vertical. The angle of the torch tip head is roughly 45º relative to the axis of the hole.
4. Smoothly rotate the handle of the torch at one revolution in 3 seconds.

WARNING: Going too slow may potentially melt the templates

5. Extinguish the needle torch.

E. Edge Cleaning Instructions

NOTE: Throughout the cleaning process for both materials constantly inspect the edge with the loupe or hand held lens. This will help you refine the procedure, perfect the technique, and understand the process.

1. S-Glass

NOTE: The goal of this process is to effectively remove the build-up of melted S-Glass material from the edges. Under large Lorentz force any glass beads potentially can pierce the conductor.

(a) Preparing the Spatula Edge

Figure 151: Spatula for Removing Beads

1. The rounded end (the right side end of Figure 151) doesn't need to be filed or ground.
2. The square end (the left side end of Figure 151) needs to have the following specifications
    a. The edge should be polished to have a sharpness of roughly 8 to 10 thousandths of an inch.

i. The theoretical width of the S-Glass is 9 thousandths thick and the measured spacing between the layers of the template is 12 thousandths.

ii. With 4 or 5 lbs. of pressure on the spatula on the crevice between the templates, the spatula should penetrate beneath the surface roughly 10 thousandths.

b. You may gently bend the spatula an inch or so from the end to an angle of 10º to 15º make cleaning the inside edges easier.

(b) Cleaning the Edges

1. After cutting the edge, break the beads off with the rounded end of the spatula using the motion given in Figure 152.

NOTE: Using the rounded end of the spatula will keep from dulling the polished end.

NOTE: The shearing motion is less likely to press the glass beads into the crevice of the template when compared to using a rolling or scraping motion.

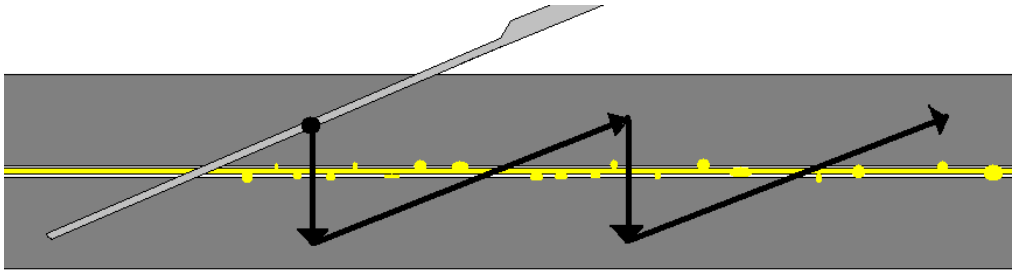

Figure 152: Spatula Motion Illustration

2. Using a small brush as shown in Figure 153 clean off the powdered debris with a motion that is perpendicular to the plane of the material between the templates. This motion minimizes penetrating the crevice of the template and keeps the bristles from prematurely disturbing the weave.

Figure 153: Brush for Removing Shards

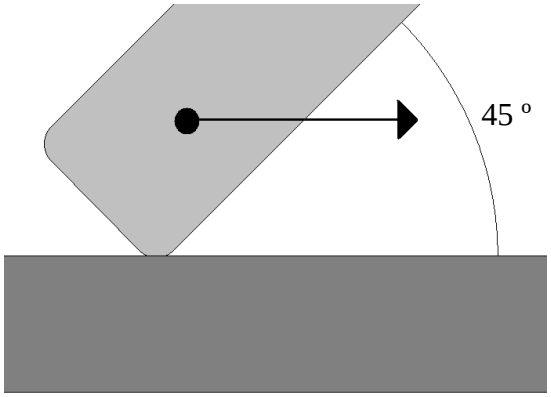

Figure 154: Spatula Angle and Motion Illustration

3. With the square end of the spatula clean out the crevice of the template.
    a. The spatula should remain in the same plane as the material.
    b. The edge should point directly into the surface of the template creating a 45º angle. See Figure 154.
    c. Press into the template with 4 or 5 pounds of force and pull rather than push the spatula.
    d. Depth of penetration should not be more than 15 thousandths or less than 6 or 7 thousandths. More depth would remove too much material and cause fraying and less depth wouldn't adequately clean out the minute glass shards.

NOTE: This motion of the spatula does two things. It scrapes out and breaks up the glass beads to a size smaller than a few mils so that they can't deeply penetrate the conductor. Secondly, as the two sides of the spatula are in contact with the top and bottom halves of the template they shear or cut the frayed strands of S-Glass from the scraping and brushing motions.

Figure 155: Dentist Tool for Removing Beads in Holes

4. For the sharp corners that the spatula can't get to use the pointed end of the dentist tool (see Figure 155) and follow the parameters of step 3.
5. Repeat step 2 to remove the powdered and sheared strands of S-Glass.
6. Repeat the cutting procedure as written in the Cutting Instructions section.
    a. Retorching the material singes and sears the edges so that the removed S-Glass piece has very little fraying.
    b. It also conglomerates the fragmented pieces of glass in the crevice for easy removal.
7. Repeat steps 3 and 4.
    a. This step is necessary to remove the newly formed glass beads in the crevice.
    b. Use the same parameters as step 3.

NOTE: If there is excessive fraying or bead build at this point you may need to repeat steps 5 and 6.

8. Repeat step 2.
9. After repeating step 2, use the small brush and gently, without over bending the bristles, clean the surface with a motion that is parallel to the crevice of the templates.

NOTE: If you are overly fraying the edges just sweep perpendicular to the crevice and ignore this step.

(c) Cleaning the Holes

NOTE: You will find that holes are more forgiving than straight sections because the weave of the fabric of S-Glass minimizes fraying.

1. After cutting the hole shear off all of the visible glass beads using the blunt end of your brush.
2. Use the pointed edge of the dentist tool and scrape the crevice of the template.
3. Thoroughly clean out the debris with the small brush.
4. If there are visibly frayed strands of S-Glass, retorch the holes and repeat steps 1, 2 and 3.

2. Mica

NOTE: Mica is much easier to clean than S-Glass. Use the same tools as for S-Glass unless noted otherwise

(a) Cleaning the Edges

1. After cutting the edge break the beads off with the rounded end of the spatula using the motion given in Figure 152.

NOTE: Using the rounded end of the spatula will keep from dulling the polished end.
NOTE: The shearing motion is less likely to press the mica into the crevice of the template when compared to using a rolling or scraping motion.

2. Using a small brush clean off the powdered debris with a motion that is perpendicular to the plane of the material between the templates. This motion minimizes penetration of the crevice and keeps the bristles from chipping flakes off of the mica.
3. It is unnecessary to scrape the edges like for S-Glass. The edge is finished.

(b) Cleaning the Holes

1. After cutting the hole shear off all of the visible mica beads using the blunt end of your brush.
2. Thoroughly clean out the debris with the small brush.

F. Inverting the Screw Clamps

1. First thoroughly clean all around the top and bottom of the screw clamps with the small brush. This minimizes the possibility of contaminating the piece and creating powdered S-Glass.
2. Remove one clamp from the outside of the template.
3. Replace the clamp under the following guidelines.
    a. Place the clamp on the inside of the template directly across from the place it was removed unless:
        i. There is insufficient space between clamps. In which case find a new spot for the clamp.
        ii. The clamp would interfere with cutting and cleaning a hole. Keeping the clamps at least a quarter of an inch from the holes should be sufficient.
    b. Keep the same orientation so that all of the red screw knobs point the same direction.
    c. Hand-tighten the clamps.
4. Repeat steps 2 and 3 until all clamps are on the inside of the template.
5. Use a pair of pliers to tighten the clamps an eighth to a quarter of a turn.

NOTE: It is necessary to tighten slightly with pliers on this step because the outside is prone to having more gaps between the templates compared to the inside.

6. If the clamps are tight, the templates are aligned, and the layout looks something like Figure 156, you are ready to begin cutting the holes and the outside of the template.

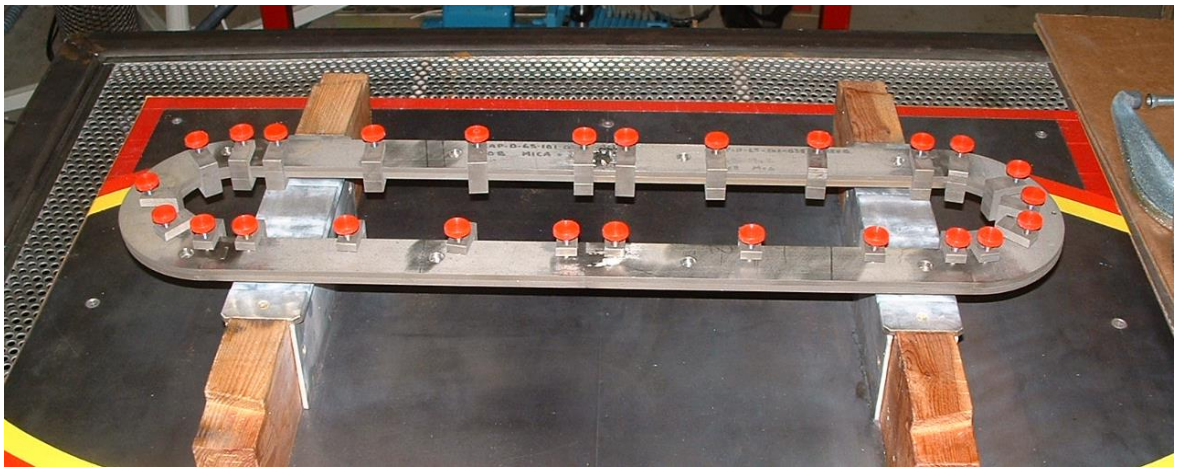

Figure 156: Inverting the Screw Clamps

G. Removing and Storing Finished Pieces

NOTE: The procedure will be the same for a Mica piece and for an S-Glass piece.

1. Thoroughly clean all surfaces of the template with the brush.
    a. Clean top and bottom of templates
    b. Clean inside and outside rings of the template
    c. Clean around each screw clamp and the holes
2. Thoroughly clean all surfaces that will come in contact with the piece to be removed.
    a. The cut Garolite phenolic that stores the pieces
    b. The ground steel flat plate
    c. The tabletop you are working on
    d. The spatula to help separate the piece from the template
3. While working on the clean tabletop and without shifting the templates remove all of the screw clamps.
4. Slowly and gently remove the top half of the template.

NOTE: The cut piece is prone to mechanically adhere to the surface of the template. If necessary use the cleaned spatula to separate the piece from the template.

5. With the cut piece exposed on top of the bottom half of the template and the template on the clean table top cover the cut piece with the phenolic or with the ground steel flat plate.
    a. Use the phenolic if you will be quickly storing the piece.
    b. Use the flat plate if you will be inspecting or immediately using the piece.
6. Gently flip the three pieces together in tandem so that the flat plate is on bottom, the cut piece is in the middle and the last half of the template is on top
7. Slowly and gently remove the last half of the template.

NOTE: The cut piece is prone to mechanically adhere to the surface of the template. If necessary use the cleaned spatula to separate the piece from the template.

8. For storage, find the correctly labeled Garolite phenolic sheets in the storage box on top of the wooden cabinet in the winding room. They should be wrapped in plastic wrap and stored in the box in Figure 157.

Figure 157: Cut Mica and S-Glass Storage Container

9. Cut out a piece of brown paper that is ¼" smaller on all sides than the phenolic to be used as a spacer between previous cut outs.
10. Place the new piece along with the piece of brown paper on top of the stack and rewrap with plastic wrap.
11. Find the spreadsheet with all of the data for what is contained in the storage box and fill out all pertinent data.

H. Master Procedure

WARNING: If not using the downdraft table, wear a breathing mask and covering clothes to minimize contact with S-Glass strands.

1. S-Glass

WARNING: Always cut and handle magnet material with cotton gloves to prevent contamination.

1. Clean and prepare working area, equipment, and raw materials.
2. Prepare the S-Glass material according to the procedure on page 173.
3. Prepare the templates according to the procedure on page 175.
4. Align the S-Glass and templates according to the procedure on page 175.
5. Fasten the templates and material with according to the procedure on page 178.
6. Initialize the torch according to the procedure on page 179.
7. Cut the inside of the template according to the procedure on page 181.
8. Clean the inside cut edge according to the procedure on page 183.
9. Invert the screw clamps according to the procedure on page 188.
10. Cut the outside and the holes according to the procedures on page 181.
11. Clean the outside and the holes according to the procedures on pages 183.
12. Clean the template and the work area for removing the S-Glass.
13. Remove and store the finished piece according to the procedure on page 189.
14. Fill out the spreadsheet that is with the storage box and make sure it is up to date.
15. Clean up and tidy up the working area, equipment, and supplies.
16. Update and refine the procedure if necessary.

2. Mica

WARNING: Always cut and handle magnet material with cotton gloves to prevent contamination.

1. Clean and prepare working area, equipment, and raw materials.
2. Prepare the mica material according to the procedure on page 173.

3. Prepare the templates according to the procedure on page 175.
4. Align the mica and templates according to the procedure on page 175.
5. Fasten the templates and material according to the procedure on page 178.
6. Initialize the torch according to the procedure on page 179.
7. Cut the inside of the template according to the procedure on page 181.
8. Clean the inside cut edge according to the procedure on page 183.
9. Invert the screw clamps according to the procedure on page 188.
10. Cut the outside and the holes according to the procedures on page 181.
11. Clean the outside and the holes according to the procedures on pages 183.
12. Clean the template and the work area for removing the mica.
13. Remove and store the finished piece according to the procedure on page 189.
14. Fill out the spreadsheet that is with the storage box and make sure it is up to date.
15. Clean up and tidy up the working area, equipment, and supplies.
16. Update and refine the procedure if necessary.

3. Cutting Mica and S-Glass Together

NOTE: It would be wise to cut complete magnet packages out together. This minimizes handling and fraying.

1. For cutting S-Glass and mica simultaneously follow the procedure for S-Glass with the following guidelines:
    a. Make the polished square end of the spatula broader by the thickness of the mica layers (0.002” or 0.004”).
    b. Slow down the cutting speed from 3 seconds per inch to 4 seconds per inch.
    c. You may add mica up to 0.006” thick to the single layer of S-Glass. Any more mica would cause too large of a gap between the halves of the template for cleaning.
    d. Trying to cut two layers of S-Glass with mica is ill advised.
2. Trying to make two layers of S-Glass at one time is not advised.
    a. The fraying is too excessive.

b. It is overly difficult to remove lodged glass beads between layers of S-Glass.

3. Trying to make several layers of mica simultaneously is acceptable.
    a. A stack of 0.012” thickness is probably the limit.
    b. It is suggested that the 0.004” thick mica be used.
        i. Separating the layers is tedious and the 0.002” mica is prone to tearing.
        ii. It is easier to differentiate the thicker mica.
    c. After removing the mica, separate the layers if desired.
        i. The key to separating layers is getting them started correctly.
        ii. Use a fresh razor and the spatula along one of the rounded edges.
        iii. Be gentle and patient. You’ve come too far to tear a piece now.